



MEASUREMENT OF THE CROSS SECTION RATIO  $\sigma(\chi_{C2})/\sigma(\chi_{C1})$  FOR PROMPT  $\chi_C$   
PRODUCTION WITH CMS EXPERIMENT

A THESIS SUBMITTED TO  
THE GRADUATE SCHOOL OF NATURAL AND APPLIED SCIENCES  
OF  
MIDDLE EAST TECHNICAL UNIVERSITY

BY

ILINA V. AKIN

IN PARTIAL FULFILLMENT OF THE REQUIREMENTS  
FOR  
THE DEGREE OF DOCTOR OF PHILOSOPHY  
IN  
PHYSICS

SEPTEMBER 2012

Approval of the thesis:

**MEASUREMENT OF THE CROSS SECTION RATIO  $\sigma(\chi_{C2})/\sigma(\chi_{C1})$  FOR PROMPT  $\chi_C$   
PRODUCTION WITH CMS EXPERIMENT**

submitted by **ILINA V. AKIN** in partial fulfillment of the requirements for the degree of  
**Doctor of Philosophy in Physics Department, Middle East Technical University** by,

Prof. Dr. Canan Özgen  
Dean, Graduate School of **Natural and Applied Sciences**

\_\_\_\_\_

Prof. Dr. Mehmet Zeyrek  
Head of Department, **Physics**

\_\_\_\_\_

Prof. Dr. Mehmet Zeyrek  
Supervisor, **Physics Department, METU**

\_\_\_\_\_

**Examining Committee Members:**

Prof. Dr. Müge Boz  
Physics Department, Hacettepe University

\_\_\_\_\_

Prof. Dr. Mehmet Zeyrek  
Physics Department, METU

\_\_\_\_\_

Prof. Dr. Altuğ Özpıneci  
Physics Department, METU

\_\_\_\_\_

Assoc. Prof. Dr. Muhammed Deniz  
Physics Department, Dokuz Eylül University

\_\_\_\_\_

Assoc. Prof. Dr. Ismail Turan  
Physics Department, METU

\_\_\_\_\_

**Date:**

\_\_\_\_\_

**I hereby declare that all information in this document has been obtained and presented in accordance with academic rules and ethical conduct. I also declare that, as required by these rules and conduct, I have fully cited and referenced all material and results that are not original to this work.**

Name, Last Name: ILINA V. AKIN

Signature :

# ABSTRACT

MEASUREMENT OF THE CROSS SECTION RATIO  $\sigma(\chi_{c2})/\sigma(\chi_{c1})$  FOR PROMPT  $\chi_c$   
PRODUCTION WITH CMS EXPERIMENT

Akin, Ilina Vasileva

Ph.D., Department of Physics

Supervisor : Prof. Dr. Mehmet Zeyrek

September 2012, 121 pages

The prompt production of  $\chi_c$  quarkonia is studied in proton-proton collisions at 7 TeV, using data collected by CMS in 2011 corresponding to an integrated luminosity of  $4.6 \text{ fb}^{-1}$ . The  $\chi_c$  mesons are reconstructed through their radiative decays to  $J/\psi$  and photon with  $J/\psi \rightarrow \mu^+\mu^-$ . The photons are reconstructed through their conversion in electron-positron pairs in the tracking detector which gives a mass resolution sufficient for resolving these states. The ratio of the prompt production cross sections for the  $\chi_{c1}$  and  $\chi_{c2}$  states,  $\sigma(\chi_{c2})/\sigma(\chi_{c1})$ , has been determined as a function of the  $J/\psi$  transverse momentum between 7 and 25 GeV/c.

Keywords: CMS, physics, QCD, quarkonium

# ÖZ

## CMS DENEYİNDE ANLIK CHİC ÜRETİMİNDE $\sigma(\chi_{c2})/\sigma(\chi_{c1})$ TESİR KESİT ORANI ÖLÇÜMÜ

Akin, Ilina Vasileva

Doktora, Fizik Bölümü

Tez Yöneticisi : Prof. Dr. Mehmet Zeyrek

Eylül 2012, 121 sayfa

Chic quarkonia'ların 7 TeV'lik proton-proton çarpışmalarındaki anlık üretimi CMS deneyi tarafından 2011 yılında toplanmış  $4.6 \text{ fb}^{-1}$ 'lık veri kullanılarak çalışılmıştır. Chic mezonları  $J/\psi$  ve fotona olan ışınımsal bozunmalarından ( $J/\psi \rightarrow \mu^+\mu^-$ ) geri oluşturulmuştur. Fotonlar bu halleri ayırtmak için yeterli kütle çözünürlüğünü sağlayacak şekilde, iz algıcında gerçekleşen elektron-pozitron çiftlerine dönüşümü aracılığıyla geri-oluşturulmuştur. Chic1 and chic2 ( $\chi_{c1}$  and  $\chi_{c2}$ ) hallerinin anlık üretim tesir kesitlerinin oranı,  $\sigma(\chi_{c2})/\sigma(\chi_{c1})$ ,  $J/\psi$ 'nin 7 - 25 GeV/c arası transvers momentumunun fonksiyonu olarak belirlenmiştir.

Anahtar Kelimeler: CMS, fizik, QCD, quarkonium

*To my parents*

## ACKNOWLEDGMENTS

This work was carried out during the years 2011-2012 at the European laboratory for particle physics (CERN) near Geneva.

I am grateful to my supervisor, Prof. Mehmet Zeyrek, who suggested the topic for my research project, for his support during my entire MS and PhD programs and for giving me the unique opportunity to work at the world's largest particle physics laboratory, CERN.

I am grateful to my supervisor at CERN, Stefano Argiro'. Without his enthusiasm, dedication and hard work, this study would never have succeeded. I would like to thank him for inviting me to stay for two months at the University of Torino, for providing a financial support for that and for his help during the entire analysis.

I would like to thank Domenico Giordano for introducing me to the  $\chi_c$  analysis and for his guidance during my first steps in this measurement. I greatly appreciate his expert knowledge in photon conversions essential for this measurement.

I am grateful to Torsten Dahms for his support at the beginning of my work. I would like to thank Nadia Pastrone for being very helpful and kind to me when I was in Torino.

I am grateful to the B-Physics conveners, Hermine Wöehri and Carlos Lourenco, for their help and support during the entire analysis. My special thanks are for Hermine Wöehri who made it possible for me to present the results of the measurement to a conference and for helping me with an application for a scholarship.

This analysis would never has succeeded without the expert knowledge of the committee members assigned to review this analysis. I am grateful to Pietro Faccioli, Maxim Gouzevitch and Andrea Venturi. I learnt a lot from them about different aspects of high-energy physics measurements.

I would like to thank Sergey Baranov, Kuang-Ta Chao and Yan-Qing Ma for providing theory predictions to be compared with the measurement.



I thank my friends at CERN, Giuseppe Codispoti, Carlo Battilana, Letizia Lusito and Muhammad Ahmad for their support and help. I also thank my dear friend Sholeh Alaei, for her friendship during all these years and Buğra Bilin and Selçuk Bilmiş for their friendship and their help with various translations into Turkish language.

My special thanks are for Andreas Korn for his support, valuable discussions and understanding during these years.

In conclusion, this research would not have been possible without the financial support of the Turkish Atomic Energy Agency (TAEK).

# TABLE OF CONTENTS

ABSTRACT . . . . .	iv
ÖZ . . . . .	v
ACKNOWLEDGMENTS . . . . .	vii
TABLE OF CONTENTS . . . . .	ix
LIST OF TABLES . . . . .	xii
LIST OF FIGURES . . . . .	xiv
CHAPTERS	
1 Introduction . . . . .	1
2 Theory . . . . .	3
2.1 Standard Model . . . . .	3
2.2 Quantum Chromodynamics . . . . .	3
2.3 Quarkonium bound states . . . . .	5
2.4 Perturbative QCD . . . . .	7
2.5 Non-perturbative QCD . . . . .	9
2.6 Quarkonium production models . . . . .	10
2.6.1 Early production models . . . . .	10
2.6.2 NRQCD factorization . . . . .	12
2.6.3 Fragmentation function approach . . . . .	13
2.7 $\chi_c$ production in hadron colliders . . . . .	14
3 The LHC and CMS experiment . . . . .	16
3.1 LHC . . . . .	16
3.2 Luminosity . . . . .	17
3.3 The Compact Muon Solenoid . . . . .	17
3.3.1 Coordinate system . . . . .	18

3.3.2	Tracker . . . . .	18
3.3.3	Calorimetry . . . . .	22
3.3.4	Magnet . . . . .	25
3.3.5	Muon System . . . . .	25
3.4	CMS Trigger . . . . .	27
3.5	CMS data flow . . . . .	29
4	Measurement . . . . .	31
4.1	Production and decay of $\chi_c$ states . . . . .	31
4.2	Data sample . . . . .	32
4.3	Triggers . . . . .	34
4.4	Candidate reconstruction and selection . . . . .	35
4.4.1	Muons . . . . .	35
4.4.2	$J/\psi$ candidates . . . . .	37
4.4.3	Converted photons . . . . .	37
4.4.4	$\chi_c$ candidates . . . . .	44
4.5	Production ratio - definition . . . . .	45
4.6	Data analysis . . . . .	48
4.6.1	Unbinned maximum likelihood fit . . . . .	48
4.6.2	Kinematic distributions from data . . . . .	52
4.7	Acceptance and efficiency studies with Monte Carlo . . . . .	58
4.7.1	Measurement of the ratio of efficiencies $\epsilon_1/\epsilon_2$ . . . . .	58
4.7.2	Kinematic distributions from Monte Carlo . . . . .	65
4.7.3	Absolute $\chi_c$ photon reconstruction efficiency . . . . .	67
4.7.4	Reconstruction efficiency for $J/\psi$ . . . . .	71
4.8	Consistency checks . . . . .	73
4.9	Systematic studies . . . . .	74
4.9.1	Uncertainty from mass fit . . . . .	74
4.9.2	Uncertainty on the ratio of efficiencies $\epsilon_1/\epsilon_2$ . . . . .	76
4.9.3	Pileup . . . . .	78
4.9.4	$\chi_c$ polarization . . . . .	81

4.9.5	Systematics summary . . . . .	84
4.10	Results . . . . .	85
4.11	Comparison with theory . . . . .	88
5	Conclusions . . . . .	91
REFERENCES . . . . .		93
APPENDICES		
A	Kinematic variables . . . . .	96
B	Fitting methods . . . . .	98
C	Fits to Pythia Monte Carlo particle gun . . . . .	101
D	Uncertainties from the signal model . . . . .	107
E	$p_T(J/\psi)$ spectrum measured with the CMS experiment . . . . .	109
F	Expressions for the $\chi_{c1}$ and $\chi_{c2}$ decay angular distributions . . . . .	110
G	Polarization of $\chi_c$ in Collins-Soper frame . . . . .	113

# LIST OF TABLES

## TABLES

Table 2.1 Quarks and leptons properties. Every particle in the table has a corresponding antiparticle with opposite charge. According to the Standard Model, the neutrino masses are equal to zero. Observed neutrino oscillation suggests that the neutrinos have mass and their experimental values are reported in the table. . . . .	4
Table 2.2 Boson properties. . . . .	5
Table 2.3 Scales in charmonium system [14]. The velocity $v$ is given with respect to the speed of light. . . . .	9
Table 4.1 Charmonium bound states. . . . .	31
Table 4.2 Data samples used in the analysis. . . . .	33
Table 4.3 Trigger paths used in the analysis. . . . .	34
Table 4.4 Summary of the cuts used to select $\chi_c$ candidates. . . . .	47
Table 4.5 Parameters of the Double Crystal Ball function from Monte Carlo simulation for $\chi_{c1}$ and $\chi_{c2}$ . . . . .	51
Table 4.6 Results of the maximum likelihood fit with the Monte Carlo driven signal parametrization and exponential multiplied by power law background parametrization. The uncertainties are statistical only. The uncertainty on the ratio includes the correlation between $N_{\chi_{c1}}$ and $N_{\chi_{c2}}$ . . . . .	52
Table 4.7 The values of $\epsilon_1/\epsilon_2$ obtained from Pythia Monte Carlo particle gun. The uncertainties on $\epsilon_1$ and $\epsilon_2$ are statistical and they are assumed to be binomial. . . . .	65
Table 4.8 Values of $N_{\chi_{c2}}/N_{\chi_{c1}}$ without $\pi^0$ cut. . . . .	74
Table 4.9 Values of $\epsilon_1/\epsilon_2$ without $\pi^0$ cut. . . . .	74
Table 4.10 Values of $\epsilon_1/\epsilon_2$ for different choices of input $p_T(\chi_c)$ spectrum. . . . .	77

Table 4.11 Number of vertices in bins up to a given number (Case 1) and in individual bins (Case 2) for Run 2011A and Run 2011B. . . . .	79
Table 4.12 The values of $\epsilon_1/\epsilon_2$ for different polarization scenarios in the helicity frame relative to the unpolarized case. . . . .	85
Table 4.13 Relative systematic uncertainties on $\frac{\sigma(\chi_{c2})\mathcal{B}(\chi_{c2})}{\sigma(\chi_{c1})\mathcal{B}(\chi_{c1})}$ for various $p_T(J/\psi)$ from different sources and the sum of individual uncertainties in quadrature. . . . .	85
Table 4.14 Measurements of $\frac{\sigma(\chi_{c2})\mathcal{B}(\chi_{c2})}{\sigma(\chi_{c1})\mathcal{B}(\chi_{c1})}$ for various values of $p_T(J/\psi)$ . The first uncertainty is statistical, the second is systematic. The last two columns report the uncertainty deriving from the extreme polarization scenarios in the helicity and Collins-Soper frames. . . . .	86
Table 4.15 Measurements of $\sigma(\chi_{c2})/\sigma(\chi_{c1})$ for various values of $p_T(J/\psi)$ . The first uncertainty is statistical, the second is systematic, the third is the branching fractions uncertainty. Two separate columns report the uncertainty deriving from the extreme polarization scenarios in the helicity and Collins-Soper frames. . . . .	86
Table D.1 Ratio of $N_{\chi_{c2}}/N_{\chi_{c1}}$ for different signal parameters varied within their uncertainties. . . . .	108
Table G.1 The values of $\epsilon_1/\epsilon_2$ for different polarization scenarios in the Collins-Soper frame relative to the unpolarized case. . . . .	114

# LIST OF FIGURES

## FIGURES

Figure 2.1	Charmonium spectrum. . . . .	6
Figure 2.2	QCD coupling constant [8]. . . . .	8
Figure 3.1	CERN Accelerator Complex. . . . .	16
Figure 3.2	Schematic view of the CMS detector [1]. . . . .	18
Figure 3.3	Tracker overview [1]. . . . .	19
Figure 3.4	Pixel overview [1]. . . . .	20
Figure 3.5	The material budget in units of radiation length as a function of $\eta$ for different subdetectors (left) and functional contributions (right) [1]. . . . .	22
Figure 3.6	ECAL layout [1]. . . . .	23
Figure 3.7	CMS view with locations for hadron barrel (HB), endcap (HE), outer (HO) and forward (HF) calorimeters (left) and HCAL tower segmentation of HB, HO and HE (right) [1]. . . . .	24
Figure 3.8	CMS iron yoke and field lines of the magnet [1]. . . . .	26
Figure 3.9	CMS muon DT chambers in one of the five wheels [1]. . . . .	27
Figure 3.10	CMS CSC at the endcaps [1]. . . . .	28
Figure 3.11	Level-1 Trigger structure [1]. . . . .	29
Figure 4.1	Prompt and non-prompt $\chi_c$ production. . . . .	32
Figure 4.2	Dimuon mass distribution obtained from overlapping several trigger paths in narrow mass windows. . . . .	33
Figure 4.3	Invariant mass distribution of $J/\psi$ candidates with muon and vertex probability cuts. The steps in the plot correspond to different dimuon trigger paths. . . . .	38

Figure 4.4 Example of a positive (left) and a negative (right) distance of minimum approach between two ideal track circles [42]. . . . .	41
Figure 4.5 Conversion vertices distributions in radial plane in silicon pixel and strip (TIB) trackers. Most conversions occur in the three pixel layers placed at 4.4, 7.3 and 10.2 cm. . . . .	42
Figure 4.6 $x$ - $y$ distribution in the pixel detector region of the position of the reconstructed conversion vertex. The beam pipe at radius of $\sim 3$ cm is clearly visible, off-centered with respect to the pixel detector, as well as the three pixel layers with radii of 4.4, 7.3 and 10.2 cm. . . . .	43
Figure 4.7 Pseudo-proper decay length distribution of $J/\psi$ from the selected $\chi_c$ candidates. The prompt component is shown in green, the non-prompt component is in lilac and the prompt + non-prompt component is in blue. A cut of $30 \mu\text{m}$ to the pseudo-proper decay length shown in red selects the prompt component of $J/\psi$ . . . . .	46
Figure 4.8 Fits to mass difference spectrum for $\chi_c$ candidates for $p_T(J/\psi)$ in $[7.0 - 9.0]$ GeV/c with $\chi^2/ndf = 0.77$ (top) and $[9.0 - 11.0]$ GeV/c with $\chi^2/ndf = 1.03$ (bottom). . . . .	53
Figure 4.9 Mass difference spectrum for $\chi_c$ candidates for $p_T(J/\psi)$ in $[11.0 - 13.0]$ GeV/c with $\chi^2/ndf = 0.9$ (top) and $[13.0 - 16.0]$ GeV/c with $\chi^2/ndf = 0.9$ (bottom). . . . .	54
Figure 4.10 Mass difference spectrum for $\chi_c$ candidates for $p_T(J/\psi)$ in $[16.0 - 20.0]$ GeV/c with $\chi^2/ndf = 0.86$ (top) and $[20.0 - 25.0]$ GeV/c with $\chi^2/ndf = 0.81$ (bottom). . . . .	55
Figure 4.11 Transverse momentum (left) and pseudorapidity (right) distributions of converted photons from $\chi_{c1}$ (black) and $\chi_{c2}$ (blue) in data with cuts from Table 4.4. The pseudo-rapidity of the photon is in the range $[-1.1, 1.1]$ therefore the photon does not fly very far from the $J/\psi$ , see Figure 4.12. . . . .	56
Figure 4.12 Transverse momentum (left) and rapidity (right) distributions of $J/\psi$ from $\chi_{c1}$ (black) and $\chi_{c2}$ (blue) in data with cuts from Table 4.4. The cut on the rapidity of the $J/\psi$ in $[-1, 1]$ is clearly visible. . . . .	57
Figure 4.13 Transverse momentum (left) and rapidity (right) distributions of $\chi_{c1}$ (black) and $\chi_{c2}$ (blue) in data data with cuts from Table 4.4. . . . .	57



Figure 4.14 The $p_T$ spectrum measured in [45] is shown with data points. The green line is the fitted spectrum with Equation 4.13 used as input distribution for the Pythia Monte Carlo particle gun. . . . .	59
Figure 4.15 Production of $\chi_c$ in proton-proton collisions and its decay to $J/\psi + \gamma$ . The polar and azimuthal angles, $\theta'$ and $\phi'$ , are between the positive muon as measured in the $J/\psi$ rest frame and the direction of the $J/\psi$ as seen in the $\chi_c$ rest frame. Polar angle $\theta$ is between $J/\psi$ in the $\chi_c$ rest frame and $\chi_c$ direction in the laboratory.	60
Figure 4.16 Polar angle of the muon in the $J/\psi$ rest frame with respect to the $J/\psi$ direction as seen from the $\chi_{c1}$ rest frame. Left: before reweighting, right: after reweighting. . . . .	62
Figure 4.17 Polar angle of the muon in the $J/\psi$ rest frame with respect to the $J/\psi$ direction as seen from the $\chi_{c2}$ rest frame. Left: before reweighting, right: after reweighting. . . . .	62
Figure 4.18 $p_T$ distributions for the converted photons coming from $\chi_{c1}$ and $\chi_{c2}$ as generated with Pythia Monte Carlo particle gun with $p_T(\psi')$ input spectrum for $\chi_c$ (left) and reconstructed with CMS detector with applied cuts in Table 4.4 (right). . . . .	66
Figure 4.19 $p_T$ distributions for the $J/\psi$ coming from $\chi_{c1}$ and $\chi_{c2}$ as generated with Pythia Monte Carlo particle gun with $p_T(\psi')$ input spectrum for $\chi_c$ (left) and reconstructed with CMS detector with applied cuts in Table 4.4 (right). . . . .	66
Figure 4.20 $p_T$ distributions for $\chi_{c1}$ and $\chi_{c2}$ as generated with Pythia Monte Carlo particle gun with $p_T(\psi')$ input spectrum for $\chi_c$ (left) and reconstructed with CMS detector with applied cuts in Table 4.4 (right). . . . .	67
Figure 4.21 $p_T(J/\psi)$ vs $p_T(\chi_c)$ with mean distributions superimposed for $\chi_{c1}$ (top) and $\chi_{c2}$ (bottom) generated with Pythia Monte Carlo particle gun with flat $p_T$ input spectrum for $\chi_c$ . The slopes of the mean distributions are 0.875 and 0.879 respectively. . . . .	68
Figure 4.22 $p_T(\gamma)$ vs $p_T(J/\psi)$ with mean distributions superimposed for $\chi_{c1}$ (top) and $\chi_{c2}$ (bottom) generated with Pythia MC particle gun with flat $p_T$ input spectrum for $\chi_c$ . The slopes of the mean distributions are 0.128 and 0.142 respectively. . . . .	69

Figure 4.23 Conversion probability and reconstruction efficiency of $\chi_c$ photons as a function of photon transverse momentum measured with Pythia Monte Carlo particle gun in $ \eta(\gamma)  < 1$ . . . . .	71
Figure 4.24 Ratio of the $J/\psi$ detection efficiencies for $J/\psi$ produced by decay of the simulated $\chi_{c1}$ and $\chi_{c2}$ . The values of the ratio of the $J/\psi$ detection efficiencies for all $p_T(J/\psi)$ ranges are consistent with one within statistical uncertainties. . . . .	72
Figure 4.25 Values of $\epsilon_1/\epsilon_2$ for the $\psi'$ and flat input spectrum and their fit to a straight line. Uncertainties are statistical and are due to limited size of the simulation sample. . . . .	78
Figure 4.26 Top: Distribution of the number of primary vertices in Run2011A (left) and Run2011B (right). Middle: stability of the ratio $N_{\chi_{c2}}/N_{\chi_{c1}}$ in bins up to a given number of vertices (Case 1) for Run2011A (left) and Run2011B (right). Bottom: stability of the ratio $N_{\chi_{c2}}/N_{\chi_{c1}}$ for individual bins of the number of vertices (Case 2) for Run2011A (left) and Run2011B (right). . . . .	80
Figure 4.27 Angle between the direction of the $J/\psi$ and $\chi_c$ as seen in $\chi_c$ rest frame for unpolarized, helicities 0, $\pm 1$ and $\pm 2$ $\chi_c$ states in the helicity frame. Left: $\chi_{c1}$ , right: $\chi_{c2}$ . . . . .	83
Figure 4.28 $p_T$ distributions of the photon from $\chi_{c1}$ (left) and $\chi_{c2}$ (right) for unpolarized, helicities 0, $\pm 1$ and $\pm 2$ $\chi_c$ states in the helicity frame. . . . .	84
Figure 4.29 Ratio of the $\chi_{c2}$ to $\chi_{c1}$ production cross sections (circles) and the ratio of the cross sections times the branching fractions to $J/\psi + \gamma$ (squares) as a function of the $J/\psi$ transverse momentum. The green band corresponds to the systematic uncertainties and the error bars to the statistical uncertainties. For the cross section ratios the 6% uncertainty from the branching fractions is not included [64]. . . . .	87

Figure 4.30 Top: Comparison of the production ratio  $\frac{\sigma(\chi_{c2})\mathcal{B}(\chi_{c2})}{\sigma(\chi_{c1})\mathcal{B}(\chi_{c1})}$  with  $k_T$  factorization approach [61]. The measurement is corrected with an acceptance factor assuming zero helicity for the  $\chi_c$  states. The  $k_T$  factorization prediction is represented by a line because theoretical uncertainties cancel out in the ratio. Bottom: Comparison of the production ratio  $\frac{\sigma(\chi_{c2})\mathcal{B}(\chi_{c2})}{\sigma(\chi_{c1})\mathcal{B}(\chi_{c1})}$  with NLO NRQCD [28] calculations. The measurement is corrected to match the kinematic range used in NLO NRQCD calculations which assume the  $\chi_c$  are produced unpolarized. The two extreme polarization scenarios in helicity frame are shown by blue and green dashed lines. The NLO NRQCD prediction is a band (red color), reflecting the uncertainties in the fitted values of the color octet matrix elements [64]. . . . . 90

Figure C.1 Double-sided Crystal Ball fits to particle gun Monte Carlo for  $\chi_{c1}$  candidates for  $p_T(J/\psi)$  in [7.0 – 9.0] GeV/c (top) and [9.0 – 11.0] GeV/c (bottom). . . . 101

Figure C.2 Double-sided Crystal Ball fits to particle gun Monte Carlo for  $\chi_{c1}$  candidates for  $p_T(J/\psi)$  in [11.0 – 13.0] GeV/c (top) and [13.0 – 16.0] GeV/c (bottom). . . 102

Figure C.3 Double-sided Crystal Ball fits to particle gun Monte Carlo for  $\chi_{c1}$  candidates for  $p_T(J/\psi)$  in [16.0 – 20.0] GeV/c (top) and [20.0 – 25.0] GeV/c (bottom). . . 103

Figure C.4 Double-sided Crystal Ball fits to particle gun MC for  $\chi_{c2}$  candidates for  $p_T(J/\psi)$  in [7.0 – 9.0] GeV/c (top) and [9.0 – 11.0] GeV/c (bottom). . . . . 104

Figure C.5 Double-sided Crystal Ball fits to particle gun MC for  $\chi_{c2}$  candidates for  $p_T(J/\psi)$  in [11.0 – 13.0] GeV/c (top) and [13.0 – 16.0] GeV/c (bottom). . . . . 105

Figure C.6 Double-sided Crystal Ball fits to particle gun MC for  $\chi_{c2}$  candidates for  $p_T(J/\psi)$  in [16.0 – 20.0] GeV/c (top) and [20.0 – 25.0] GeV/c (bottom). . . . . 106

Figure E.1 The  $p_T$  spectrum measured in [45] is shown with data points. The green line is the fit to data using Equation 4.13. The fitted spectrum is used as input distribution for the Pythia Monte Carlo particle gun. . . . . 109

Figure G.1 Angle between the direction of  $J/\psi$  and  $\chi_c$  as seen in  $\chi_c$  rest frame for unpolarized, helicities 0,  $\pm 1$  and  $\pm 2$   $\chi_c$  states in the Collins-Soper frame. Left:  $\chi_{c1}$ , right:  $\chi_{c2}$ . . . . . 113

Figure G.2  $p_T$  distributions of the photon from  $\chi_{c1}$  (left) and  $\chi_{c2}$  (right) for unpolarized, helicities 0,  $\pm 1$  and  $\pm 2$   $\chi_c$  states in the Collins-Soper frame. . . . . 114

# CHAPTER 1

## Introduction

In this thesis, we measure the ratio of production cross sections of two excited charmonia states,  $\chi_{c1}$  and  $\chi_{c2}$ , as a function of transverse momentum  $p_T$  of  $J/\psi$ . For this measurement, we use the CMS experiment [1] at the Large Hadron Collider (LHC) [2] where two proton beams collide at a center of mass energy of 7 TeV.

The measurement of the production ratio of  $\sigma(\chi_{c2})/\sigma(\chi_{c1})$  can bring new knowledge to our understanding of the theory of strong interaction, Quantum Chromodynamics [3]. Several theoretical models describe the production mechanism of quarkonium but there exists a discrepancy between their predictions and experimental results. Hence, the mechanism underlying the production of quarkonium remains a mystery.

Recent measurements of the production ratio of  $\sigma(\chi_{c2})/\sigma(\chi_{c1})$  for different  $p_T(J/\psi)$  ranges have been performed by LHCb [4] and CDF [5]. The CDF Collaboration reported a value of  $\sigma(\chi_{c2})/\sigma(\chi_{c1}) = 0.75 \pm 0.03(stat) \pm 0.03(syst)$  for  $p_T(J/\psi)$  in [4.0 – 20.0] GeV/c and pseudorapidity range  $|\eta(J/\psi)| < 1$ . The LHCb collaboration measured  $\sigma(\chi_{c2})/\sigma(\chi_{c1})$  for  $p_T(J/\psi)$  in [2.0 – 15.0] GeV/c and rapidity range  $2.0 < y(J/\psi) < 4.5$ . For  $p_T(J/\psi) > 8$  GeV/c both measurements tend to favor Non-Relativistic QCD (NRQCD) [12] factorization which is a theoretical model largely accepted to best describe quarkonium production and decay. At low  $p_T(J/\psi)$  both CDF and LHCb observe a discrepancy with NRQCD.

With the current measurement, we improve the sensitivity to theoretical models by extending the  $J/\psi$   $p_T$  spectrum beyond the spectra measured by CDF and LHCb. The measurement of the ratio of cross sections,  $\sigma(\chi_{c2})/\sigma(\chi_{c1})$ , is very effective in testing theoretical models because many experimental uncertainties cancel out.

In the CMS detector,  $\chi_c$  mesons are reconstructed through their decays into a  $J/\psi$  and a photon. The  $J/\psi$  are reconstructed with two oppositely charged muons,  $J/\psi \rightarrow \mu^+\mu^-$ , and photons are reconstructed through conversions,  $\gamma \rightarrow e^+e^-$ .

The thesis is organized as follows. In Chapter 2 we discuss the nature of the binding of the quarks inside hadrons by reviewing the theory of strong interaction, Quantum Chromodynamics in its perturbative and non-perturbative regimes. Then we discuss several quarkonium production models. Chapter 3 gives an overview of the CMS detector and its main components. In our focus are the tracker and the muon chambers where the detection and identification of converted photons and muons occur. We briefly describe the data flow, from the detection with the CMS detector to the final usage for different CMS analyses. Chapter 4 describes the measurement of the ratio of production cross sections of  $\chi_{c1}$  and  $\chi_{c2}$  and compares the results with existing theoretical calculations. The drawn conclusions are discussed in Chapter 5.

## CHAPTER 2

### Theory

#### 2.1 Standard Model

The known matter in our universe consists of quarks and leptons and their properties are summarized in Table 2.1. The quarks and leptons are grouped in three generations. The first generation contains the most stable particles which make most of the observed matter in the universe, while the second and the third generations contain particles which decay to the lower generation of particles.

The interactions among quarks and leptons occur via exchange of another type of particles named bosons, see Table 2.2. The quarks and leptons have spin-1/2 while bosons are spin-1 particles. There are four fundamental interactions: strong, weak, electromagnetic and gravitational. Each of the interactions has different strength and range of influence. Leptons participate in gravitational, electromagnetic and weak interactions. Quarks on the other hand can participate in all four interactions.

The theory which describes the strong interaction between quarks and gluons is Quantum Chromodynamics (QCD) and it will be described in the following sections.

#### 2.2 Quantum Chromodynamics

The interaction between quarks and gluons is explained by QCD. Both quarks and gluons have color charge which can have three degrees of freedom: red, blue and green. The quarks can have one of the three color degrees of freedom. In nature, however, there exist only color neutral states of quark configurations:  $q\bar{q}$  (mesons) and  $qqq$  (baryons) and they are both

Table 2.1: Quarks and leptons properties. Every particle in the table has a corresponding antiparticle with opposite charge. According to the Standard Model, the neutrino masses are equal to zero. Observed neutrino oscillation suggests that the neutrinos have mass and their experimental values are reported in the table.

<b>Leptons</b>				
Generation	Name	Symbol	Electric charge	Mass [ $MeV/c^2$ ]
First generation	Electron	$e^-$	-1	0.511
	Electron neutrino	$\nu_e$	0	< 0.000225
Second generation	Muon	$\mu^-$	-1	105.658
	Muon neutrino	$\nu_\mu$	0	< 0.19
Third generation	Tau	$\tau^-$	-1	1776.82
	Tau neutrino	$\nu_\tau$	0	< 18.2

<b>Quarks</b>				
Generation	Name	Symbol	Electric charge	Mass [ $MeV/c^2$ ]
First generation	Up	$u$	+2/3	1.8 – 3.0
	Down	$d$	-1/3	4.5 – 5.5
Second generation	Charm	$c$	+2/3	1250 – 1300
	Strange	$s$	-1/3	90 – 100
Third generation	Top	$t$	+2/3	172100 – 174900
	Bottom	$b$	-1/3	4150 – 4210

referred to as hadrons. The gluons are colorful objects and they are mixtures of two colors such as red and antiblue. There are eight types of them. Gluons in color neutral state do not exist.

Due to the exchange of gluons, quarks are confined inside hadrons. By increasing the distance between the quarks in the hadrons, the coupling between them increases and the quark interaction becomes stronger. At small distances between quarks the coupling is small, the interaction is weak and quarks are loosely bound inside the hadrons. They behave as free particles which is a feature known as asymptotic freedom.

Today QCD can not calculate simultaneously the interactions at small and large interquark distances. The two regimes of interactions are separately treated by two different methods: perturbative and non-perturbative QCD.

Table 2.2: Boson properties.

Name Symbol	Force Range (m)	Electric charge Color charge	Mass [ $GeV/c^2$ ] Strength
Photon $\gamma$	Electromagnetic $\infty$	0 0	0 $\alpha = 1/137$
Gluon $g$	Strong $10^{-15}$	0 8 colored gluons	0 $\alpha_s \sim 1$ , at high energies $\alpha_s \rightarrow 0$
Z boson $Z^0$	Weak $10^{-18}$	0 0	91.187 $\alpha_Z = 10^{-6}$
W boson $W^\pm$	Weak $10^{-18}$	$\pm 1$ 0	80.399 $\alpha_W = 10^{-6}$

### 2.3 Quarkonium bound states

Quarkonium is a meson which consists of a heavy quark ( $c$  or  $b$  quark) and its antiquark which are bound by exchange of gluons. Depending on quantum numbers  $J$  (total angular momentum),  $P$  (parity) and  $C$  (charge conjugation), there exist different quarkonium states, which are characterized by specific momentum and binding energy of the quark pair. The total spin,  $S$ , of quarkonium is a sum of the spins of the quark and the antiquark,  $S = S_1 + S_2$ . The total angular momentum of quarkonium is a sum of its total spin and its orbital angular momentum,  $L$ ,  $J = S + L$ .

Quarkonium states are usually denoted by  $n^{2S+1}L_J$ , where  $n$  is the radial quantum number,  $L = 0$  is labeled by the letter  $S$ ,  $L = 1$  by  $P$  and  $L = 2$  by  $D$ . They can be also classified by  $J^{PC}$ , where  $P = (-1)^{L+1}$  is parity and  $C = (-1)^{L+S}$  is charge conjugation.

If a quarkonium is a combination of a charm quark and its antiquark,  $c\bar{c}$ , it is called charmonium. The charmonium spectrum is given in Figure 2.1 and shows  $c\bar{c}$  states with different quantum numbers below the threshold to produce two charmed mesons.

In quarkonium systems, the kinetic energy  $mv^2$  and momentum  $mv$  of the heavy quarks are smaller than their masses  $m$ . This implies that the velocities  $v$  of the quarks in the  $q\bar{q}$  system are non-relativistic,  $v/c \ll 1$ , where  $c$  is the speed of light. As a result the time scale associated with the momentum of the binding gluons is smaller than the time scale of the heavy quark motion,  $1/mv < 1/mv^2$ . This leads to the conclusion that interaction between heavy quarks is instantaneous and can be modeled with a potential.



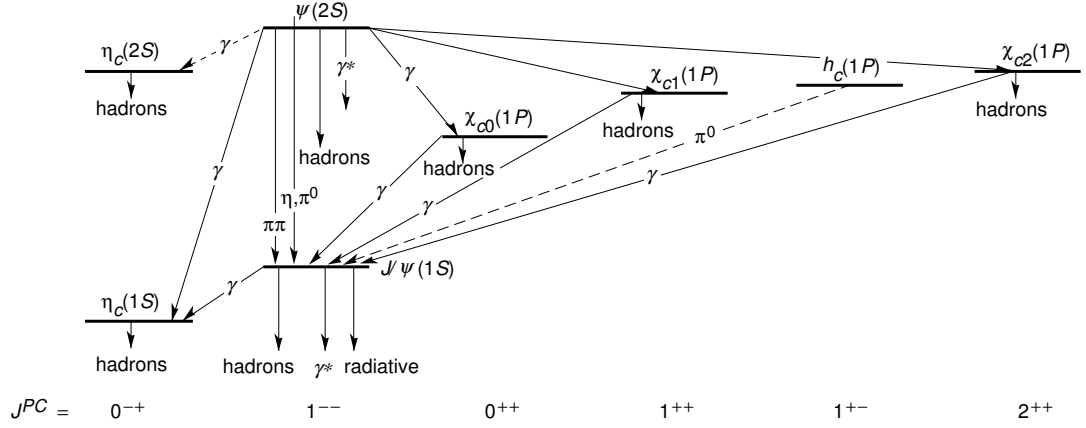


Figure 2.1: Charmonium spectrum.

A lot of studies have been done to find appropriate form of the binding potential. Coulomb like potential at short distance  $r \simeq 0.1$  fm plus linearly increasing potential at long distance  $r \sim 1$  fm

$$V(r) = -\frac{4}{3} \frac{\alpha_s}{r} + \sigma \cdot r \quad (2.1)$$

give good prediction for quarkonium spectrum in Figure 2.1. The expression in Equation 2.1 is also known as Cornell potential. The string tension,  $\sigma \simeq 2 \text{ GeV}^2$ , reflects the strength of quark-antiquark confinement,  $\alpha_s$  is the coupling constant between quarks and gluons and  $r$  is the distance between the quarks.

A typical distance between heavy quarks in quarkonium is of order  $0.1 \div 1.0$  fm. At intermediate and large interquark distances there are uncertainties in the potential in Equation 2.1. It is known that at these distances the basic characteristics of quarkonium are formed. In order to correct for these uncertainties relativistic corrections to the potential need to be included. It has been estimated that these corrections may have contribution of order  $20 \div 30\%$  [6, 7].

The potential as defined in Equation 2.1 is used to determine the quarkonium energy spectrum by solving Schrodinger equation. This approach proved to be very successful in describing different quarkonium states and their properties but has the disadvantage that it can not be derived from the theory of strong interaction, QCD.

To overcome this problem effective theories for heavy quarkonium systems based on QCD

have been developed. In Sections 2.4 and 2.5 we describe perturbative and non-perturbative QCD theory methods which are applicable respectively at short and long interquark distances in mesons and baryons. We will also describe early and more recent quarkonium production models which have been developed last years.

## 2.4 Perturbative QCD

Perturbative QCD considers quarks as free particles at short distances. The tools used for perturbative calculations also known as Feynman rules are derived from the QCD Lagrangian density

$$L_{QCD} = -\frac{1}{4}F_{\mu\nu}^a F_a^{\mu\nu} + i \sum_{q=1}^{n_f} \bar{\psi}_q^i \gamma^\mu (D_\mu)^{ij} \psi_q^j - \sum_{q=1}^{n_f} m_q \bar{\psi}_q^i \psi_q^i. \quad (2.2)$$

Equation 2.2 describes the interaction of quark fields  $\psi_q^j$  of mass  $m_q$  with massless gluons. The sums in Equation 2.2 run over different flavor of quarks  $n_f = u, d, s, c, b, t$ . The field strength tensor  $F_{\mu\nu}^a$  is derived from the gluon field  $A_\mu$

$$F_{\mu\nu} = \partial_\mu A_\nu - \partial_\nu A_\mu + ig[A_\mu, A_\nu]. \quad (2.3)$$

Equation 2.3 runs over eight color degrees of freedom of the gluon field  $A_\mu$  where  $g$  is the coupling constant. The covariant derivative  $D_\mu$  in Equation 2.2 acts on triplet quark and octet gluon fields and it is given by

$$D_\mu^{ij} = \delta_{ij} \partial_\mu + ig \frac{\lambda_{ij}^a}{2} A_\mu^a \quad (2.4)$$

where  $\lambda^a$  are fundamental representations of  $SU(3)$  color group. More information on QCD can be found at [3].

The QCD coupling constant,  $g$ , can be redefined as  $\alpha_s = \frac{g^2}{4\pi}$  and Figure 2.2 shows the change of  $\alpha_s$  with energy  $\mu$ . The energy dependence of  $\alpha_s$  is given to first order by

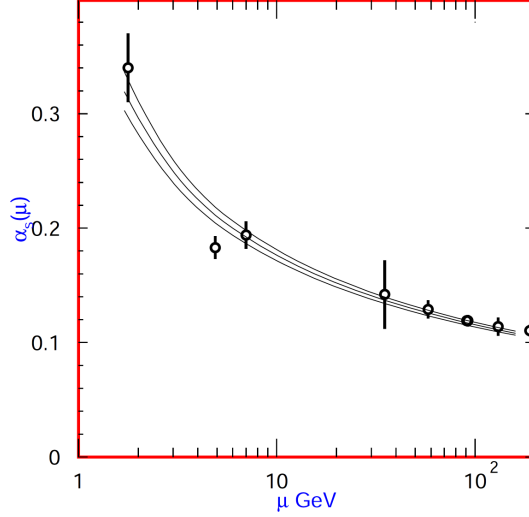


Figure 2.2: QCD coupling constant [8].

$$\alpha_s(\mu^2) = \frac{1}{b} \ln(\mu^2 / \Lambda_{QCD}^2) \quad (2.5)$$

where  $b = \frac{(33-2n_f)}{12\pi}$  and  $n_f$  is the number of different flavor of quarks.

If we calculate the quarkonium spectrum with Equation 2.2 using a perturbative expansion in  $\alpha_s$  [9], we do not have a match with experimental measurements. At  $\Lambda_{QCD} \sim 200$  MeV, which is the scale of binding of quarks and antiquarks, the coupling constant  $\alpha_s$  becomes large and perturbation theory can not be used for accurate calculations. Therefore non-perturbative formulation of the QCD Lagrangian have to be used to determine the interactions among quarks and gluons at low energies.

There exist different non-perturbative methods which explain these interactions as well as the process of hadron formation. Some of these methods are QCD sum rules [10, 11], lattice QCD [3] and effective QCD theories such as Non-Relativistic QCD (NRQCD) [12] and potential Non-Relativistic QCD (pNRQCD) [13]. Nowadays, NRQCD and pNRQCD are considered as standard tools to describe quarkonium production and decay and we will introduce them in the next sections.

## 2.5 Non-perturbative QCD

In quarkonium systems, there are several momentum scales which are important for analyzing the dynamics of interaction between quarks and antiquarks. These scales are the mass  $m$  of the heavy quark, its momentum  $mv$  and its kinetic energy  $mv^2$ . Another important scale is  $\Lambda_{QCD} \sim 200$  MeV. At this scale non-perturbative effects between quarks start to play role. The hierarchy of scales for the charmonium ground state is  $m > mv > mv^2 > \Lambda_{QCD}$  and their approximate values are given in Table 2.3 where the average charm quark velocity  $v^2$  in charmonium is about 0.25.

Table 2.3: Scales in charmonium system [14]. The velocity  $v$  is given with respect to the speed of light.

Scale	$m$	$mv$	$mv^2$	$v^2$
Values	1.5 GeV	750 MeV	400 MeV	0.25

Processes that happen at scale  $m$  play a small role in the binding of quarkonia. The coupling constant at this scale is  $\alpha_s(m) \approx 0.25$  and therefore it is allowed to describe the interaction processes in perturbative QCD. The scales of order  $mv$  and  $mv^2$  are not accessible to perturbation theory. In general, at these scales non-perturbative effects start to play role and binding of quarks and antiquarks occurs.

The effective field theories appropriate for a system with two heavy quarks are NRQCD and pNRQCD. The main idea behind these theories is introducing a cut off scale  $\Lambda$  below which the effective field theory fully describes observed physical phenomena. NRQCD is obtained from QCD by integrating out the momentum scale  $m$ , while pNRQCD is obtained from QCD by integrating out the momentum scales  $m$  and  $mv$ . The advantage of using effective field theories is that the perturbative and non-perturbative contributions are separated which is easier for computational studies. Perturbative contributions are calculated independently for each process. Non-perturbative contributions can be used in one process after being determined from another process.

### NRQCD

Non-Relativistic QCD was proposed by Caswell and Lepage [12] in 1986 and developed by Bodwin, Braaten and Lepage [15] and Luke and Manohar [16]. It is the first attempt to

systematically study heavy quark bound states in the formalism of QCD. The NRQCD is an effective field theory which describes heavy quarks and gluons with energy and momentum less than a certain cut off scale  $\Lambda$ , where  $m > \Lambda > mv$ .

The NRQCD formalism has been applied to study spectroscopy, decay and production of quarkonium [3]. The NRQCD predictions for quarkonium spectroscopy and decay are well understood but the same predictions for production do not agree very well with experimental results.

### **Potential NRQCD**

The effective theory, NRQCD, is not yet a satisfactory theory because no separation of non-relativistic fluctuations below scale  $m$  is carried out. The effective theory, pNRQCD, is more complicated than NRQCD because it is based on separation of non-relativistic fluctuations in every momentum region,  $m > mv > mv^2 > \Lambda_{QCD}$ .

The effective theory, pNRQCD, was proposed by Pineda and Soto in 1998 [13]. In pNRQCD quarks and gluons with momenta more than  $m$  and  $mv$  are integrated out and the cut off scale  $\Lambda$  is such that  $mv > \Lambda > mv^2 > \Lambda_{QCD}$ .

The pNRQCD formalism has been successfully applied to study quarkonium spectra and decays [3]. The same formalism for quarkonium production does not exist.

## **2.6 Quarkonium production models**

### **2.6.1 Early production models**

#### **Color-Singlet Model**

Color-Singlet Model (CSM) was the first model proposed to describe the production mechanism of quarkonium. It assumes that the  $q\bar{q}$  pair is produced as a color singlet object with a small relative momentum and immune to long range strong interactions with other final state particles. During the binding, the color and spin of  $q\bar{q}$  pair do not change. The model also assumes that  $q\bar{q}$  state produced in color octet state (state that do not have the color and angular momentum of the final quarkonium) never form quarkonium.

In models which will be described later, the  $q\bar{q}$  pair can be produced in a color octet state. Later gluons can be emitted from the quark  $q$  or antiquark  $\bar{q}$ , changing the color and angular momentum of the color octet  $q\bar{q}$  pair into color singlet quarkonium.

Many papers based on calculations using CSM [17, 18, 19, 20] exist. The approach is based on factorization of the two processes of quarkonium formation: production and binding of the  $q\bar{q}$  pair. This assumption is reasonable because the time scale of production of the pair is  $\sim 1/m$ , while the formation of the bound state occurs at time scale  $\sim 1/\Lambda_{QCD}$ .

The probability of binding  $q\bar{q}$  pair into quarkonium is given by the  $l$ 'th derivative of the radial wave function at zero separation between the quark and antiquark multiplied by the amplitude of producing a  $q\bar{q}$  pair at rest. Parameter  $l$  is the orbital angular momentum of the  $q\bar{q}$  pair.

The CSM assumes that only one parameter, based on the wave function at origin, describes the long distance interactions between quarks and antiquarks. This assumption might not be completely correct. Indeed, it was realized in 1993, by measuring the prompt  $J/\psi$  cross section, that the CSM does not accurately describe data especially at high transverse momentum. To solve this problem, new theory models have been developed. A new factorization scheme based on NRQCD formalism (to be discussed in Section 2.6.2) and a new production mechanism related to the fragmentation of partons (to be discussed in Section 2.6.3), have been proposed.

### Color-Evaporation Model

Color-Evaporation Model (CEM) was introduced in 1977 by Fritzsche and Halzen [21, 22]. The model assumes that at short distances  $\sim 1/m$  the  $q\bar{q}$  pair can be created in any color and spin state. This is in contradiction to the CSM where the pair is initially created in a color singlet state. The authors of the CEM question the possibility that a color singlet state formed at distances  $\sim 1/m$  can survive to form quarkonium. According to them there is an infinite time for soft gluons emitted later in the process to readjust the color of the  $q\bar{q}$  pair in color octet state before it appears as a color singlet quarkonium. The cross section to produce a quarkonium in CEM is

$$\sigma_{onium} = \frac{1}{9} \int_{2m_q}^{2m_{D,B}} dm \frac{d\sigma_{q\bar{q}}}{dm} \quad (2.6)$$

where  $\sigma_{q\bar{q}}$  is computed perturbatively and  $2m_{D,B}$  is the threshold to produce two charm or two beauty mesons. The coefficient  $\frac{1}{9}$  represents the probability of a  $q\bar{q}$  pair to be in a singlet state. The cross section for a specific quarkonium state  $H$  is given by the formula  $\sigma_H = \rho_H \sigma_{onium}$  where  $\rho_H$  is a constant and is related to the decay width of the quarkonium state  $H$ . Again, there is a separation of production and binding processes which is very similar to the factorization approach used in the CSM.

One of the predictions of CEM is the ratio of cross sections for any two quarkonium states is constant and independent of the production process. This, however, does not match experimental observations.

### 2.6.2 NRQCD factorization

The NRQCD factorization method is based on Non-Relativistic QCD [12, 15, 16] which reproduces full QCD at momentum scales of order  $mv$  and smaller. The method assumes that the long and short distance physics in quarkonium production can be separated, provided that the formation of the bound state is insensitive to the creation of the  $q\bar{q}$  pair,  $1/\Lambda_{QCD} \gg 1/m$ . The production of quarkonium  $H$  in NRQCD is represented by the factorization formula

$$\sigma(H) = \sum_n \sigma_n(\Lambda) \langle \mathcal{O}_n^H(\Lambda) \rangle. \quad (2.7)$$

Here,  $\Lambda$  is the cut off scale of the effective theory. The coefficients  $\sigma_n(\Lambda)$  represent the partonic cross sections to create a  $q\bar{q}$  pair and they are calculated in perturbative QCD. They are process dependent, calculated as an expansion in  $\alpha_s$ . The matrix elements  $\langle \mathcal{O}_n^H(\Lambda) \rangle$  represent the probability of a  $q\bar{q}$  pair to evolve into quarkonium  $H$ . The matrix elements can be color singlet and color octet operators representing the  $q\bar{q}$  pair created or annihilated in a color singlet and a color octet state. The sum in Equation 2.7 is an expansion in  $\alpha_s$  and velocity  $v$ . Through a given order in  $v$ , only a finite set of matrix elements contributes.

The color singlet matrix elements are related to wave functions of quarkonium at the origin. The color octet matrix elements can be calculated on the lattice [23], using weak coupling techniques [24] or can be related to wave functions at origin and some number of universal non-perturbative parameters [25]. The color octet matrix elements can also be extracted from data [26]. An important property of color octet matrix elements is their universality: they can

be determined independently of the production process and used in calculations for another process.

The CSM can be obtained from the NRQCD factorization formula in Equation 2.7 by excluding the color octet terms. Adding color octet terms in Equation 2.7, improved significantly the predictions of quarkonium production cross sections at high transverse momenta however these predictions suffer from many uncertainties. For example the matrix elements,  $\langle O_n^H(\Lambda) \rangle$ , can be combined in a different way for the different processes and this can be a source of uncertainty. The truncation of the sum in Equation 2.7 to a given order of  $\alpha_s$  and  $v$  can be another source of uncertainty. For example standard truncation in  $v$  includes one color singlet and three color octet matrix elements for  $S$ -wave quarkonium and one color singlet and one color octet matrix elements for  $P$ -wave quarkonium. Most of the theoretical uncertainties however cancel in ratios of cross sections.

The production mechanism of quarkonium using the NRQCD approach has been extensively studied in the last years. To describe previous experimental data, it was found that next-to-leading order (NLO) corrections in  $\alpha_s$  have to be included in calculations of hadroproduction cross sections of  $S$  [27] and  $P$  [28] wave charmonium.

### 2.6.3 Fragmentation function approach

It is believed that at large  $p_T$  the dominant mechanism of quarkonium production is fragmentation. Fragmentation is a formation of a hadron within a jet produced by a parton with large transverse momentum. The fragmentation of a parton into quarkonium is described by a universal fragmentation function. The fragmentation functions represent the probability for a parton to fragment into a particular hadron carrying a certain fraction of the parton's energy. Fragmentation functions describe the long distance, non-perturbative physics of the hadronization process in which the observed hadrons are formed and they can be expanded in terms of NRQCD matrix elements [29].

In 1993, Braaten and Yuan [30] pointed out that the dominant production mechanism for charmonium at high transverse momentum might be fragmentation. They calculated the fragmentation probability for a gluon to produce  $S$ -wave quarkonium states. In another paper [31] in 1994 they calculated the fragmentation probability for a  $g \rightarrow \chi_c$  from the parton process



$g \rightarrow c\bar{c} + g$ . They estimated that this can be the reason for the significant fraction of  $\chi_c$  observed at a large transverse momentum. Fragmentation into  $\chi_c$  followed by its radiative decay may also account for the significant fraction of  $J/\psi$  produced at these large transverse momenta.

## 2.7 $\chi_c$ production in hadron colliders

Two production models in hadron collisions will be introduced:  $k_T$  factorization and NRQCD factorization. Comparison of existing calculations for both models with the current measurement will be done in Chapter 4.

### $k_T$ factorization

The  $k_T$  factorization method [34, 35] starts from Color-Singlet quarkonium production model and it incorporates the initial state radiation through parton distribution functions which include the transverse momenta,  $k_T$ , additionally to the longitudinal momentum fraction,  $x$ , of the incident partons. A nice comparison between conventional approach which assumes that all particles involved in the calculation of parton level cross sections have only longitudinal components of their momenta and the  $k_T$  factorization approach can be found at [36].

The production cross section of  $\chi_{cJ}$  in proton-proton collisions using  $k_T$  factorization formalism is given by the formula

$$\sigma[pp \rightarrow \chi_{cJ} + X] = \sum_{i,j} \int dx_1 dx_2 dk_{1T} dk_{2T} f(x_1, k_{1T}, \mu^2) f(x_2, k_{2T}, \mu^2) \times \hat{\sigma}[i + j \rightarrow \chi_{cJ} + X]. \quad (2.8)$$

The parton cross sections  $\hat{\sigma}[i + j \rightarrow \chi_{cJ} + X]$  are evaluated in perturbative QCD. The parton distribution functions  $f(x_1, k_{1T}, \mu)$  and  $f(x_2, k_{2T}, \mu)$  depend the parton's transverse momentum  $k_T$ , as well as on the parton's longitudinal momentum fraction  $x$  [37].

### NRQCD factorization

The factorization formula in Equation 2.7 applied to  $\chi_{cJ}$  production in proton-proton collisions is

$$\begin{aligned}
\sigma[pp \rightarrow \chi_{cJ} + X] &= \sum_n \sigma(c\bar{c})_n \langle \mathcal{O}_n^{\chi_{cJ}} \rangle \\
&= \sum_{i,j,n} \int dx_1 dx_2 f_{i/p}(x_1, \mu^2) f_{j/p}(x_2, \mu^2) \\
&\quad \times \hat{\sigma}[i + j \rightarrow (c\bar{c})_n + X] \langle \mathcal{O}_n^{\chi_{cJ}} \rangle
\end{aligned} \tag{2.9}$$

where  $f_{i/p}$  and  $f_{j/p}$  denote the parton distribution functions [32, 33] which give the probability density for finding a parton with a certain longitudinal momentum fraction  $x_1$  and  $x_2$  at momentum transfer  $\mu^2$ . The indices  $i, j$  indicate  $gg, gq, g\bar{q}, q\bar{q}$  interactions and  $\hat{\sigma}$  is the parton level cross section calculated in perturbative QCD. The terms  $\langle \mathcal{O}_n^{\chi_{cJ}} \rangle$  are color singlet,  $c\bar{c}[^3P_J^{(1)}]$ , and color octet,  $c\bar{c}[^3S_1^{(8)}]$  matrix elements. They are related to the transition probability of a  $c\bar{c}$  pair into charmonium  $\chi_{cJ}$ . After radiating a gluon, from either the  $c$  or the  $\bar{c}$  quark in the color octet state  $^3S_1$ , the  $c\bar{c}$  pair is in color singlet  $^3P_J$  bound state.

## CHAPTER 3

### The LHC and CMS experiment

#### 3.1 LHC

The Large Hadron Collider (LHC) [2] is the world largest and most powerful particle accelerator. It is designed to collide proton beams at center of mass energy of 14 TeV. It has circumference of 27 kms and is placed in a tunnel, 175 meters under the ground near Geneva. The LHC is the final stage of a system of accelerators shown in Figure 3.1.

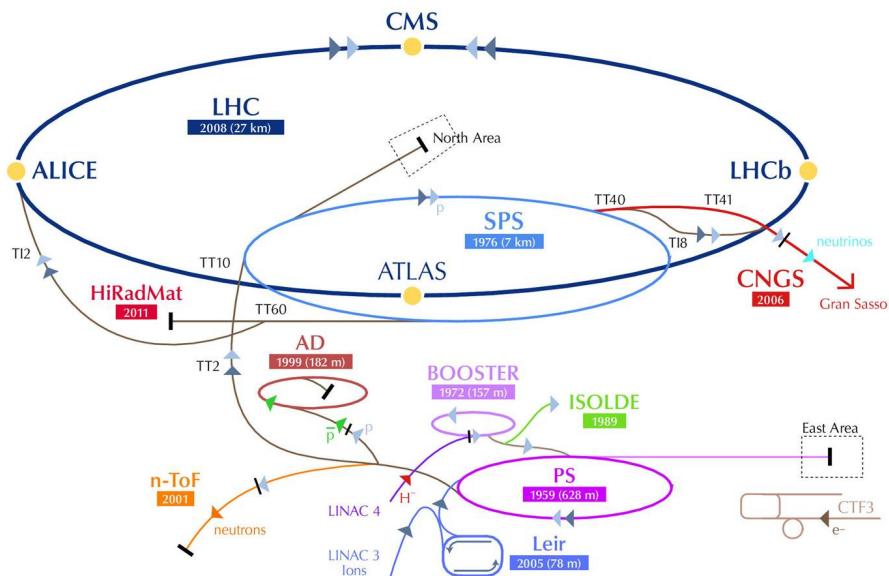


Figure 3.1: CERN Accelerator Complex.

Protons in the beams are taken from a bottle of hydrogen gas and first accelerated in linac and Proton Synchrotron to 26 GeV. Then the particles are injected into Super Proton Synchrotron

and accelerated to 450 GeV. The final acceleration to 7 TeV per proton beam is done in the two rings of the LHC. There are dipole magnets along the rings which bend the beams. Then the two beams are focused and brought into collision at four interaction points along the rings. The proton beams are accelerated with a radio frequency of 400 MHz. This gives rise to synchrotron oscillations which group the protons in the beams into packets. The LHC is designed for 2808 packets in a single beam.

### 3.2 Luminosity

The design instantaneous luminosity,  $\mathcal{L}$ , of the LHC is of order  $10^{34} \text{ cm}^{-2}\text{s}^{-1}$  and it is given by the number of collisions per second per interaction region, divided by the total cross section of the proton beam

$$\mathcal{L} = \frac{n \cdot f_{rev} \cdot N_1 \cdot N_2}{A_T^{eff}} \quad (3.1)$$

where  $A_T^{eff}$  is the effective transverse area of the proton beam,  $n$  is the number of packets the beam is splitted to and  $f_{rev}$  is the frequency of revolution around the ring.  $N_1$  and  $N_2$  are the number of protons in each packet. With respect to other high energy colliders, the design luminosity of LHC is several magnitudes larger. This is needed because LHC is designed to discover new particles at TeV scale. At these scales the interaction rates with momentum transfers more than 1 TeV are very low. Therefore more data needs to be collected which can only be achieved by having large luminosity.

### 3.3 The Compact Muon Solenoid

The Compact Muon Solenoid Experiment (CMS) [1] is one of the two general purpose detectors at LHC designed to study proton-proton interactions. It contains different subsystems which can measure energy and momentum of electrons, muons, taus, photons and hadrons. A schematic view of the CMS detector in Figure 3.2 shows all of these subdetectors.

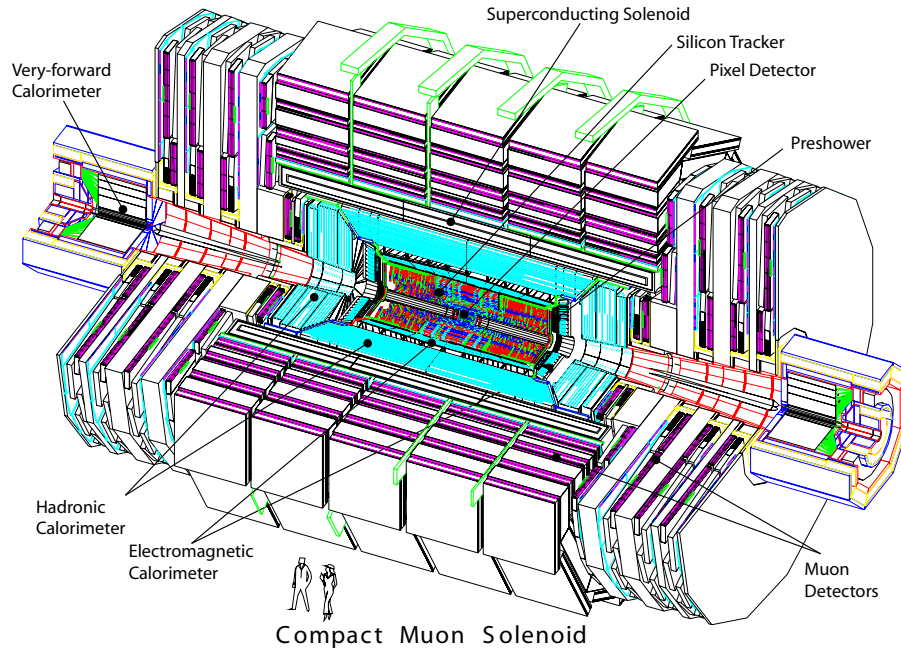


Figure 3.2: Schematic view of the CMS detector [1].

### 3.3.1 Coordinate system

The CMS coordinate system is defined with respect to the LHC ring. The  $x$  axis points towards the center of the ring, the  $y$  axis points up and the  $z$  axis is defined assuming a right handed coordinate system. The azimuthal angle  $\phi$  is measured from the  $x$  axis in  $x$ - $y$  plane and the radial coordinate is denoted by  $r$ . The polar angle  $\theta$  is defined in the  $r$ - $z$  plane. In Appendix A several kinematic variables are defined which will be used in this measurement.

### 3.3.2 Tracker

The tracker is the closest subdetector to the beam axis where the collisions occur. It has a length of 5.8 m and a diameter of 2.5 m. For each bunch crossing which happens every 25 ns there will be about 1000 particles created at the LHC luminosity of  $10^{34} \text{ cm}^{-2}\text{s}^{-1}$ . Due to the large number of particles created at each collision, the tracking system is exposed to severe radiation.

To achieve radiation hardness and at the same time good spacial resolution, the tracking sys-

tem is designed entirely of silicon sensors. The main purpose of the tracker is to record particle paths. The tracker has two main components: silicon pixel and silicon strip trackers. A schematic view is shown in Figure 3.3.

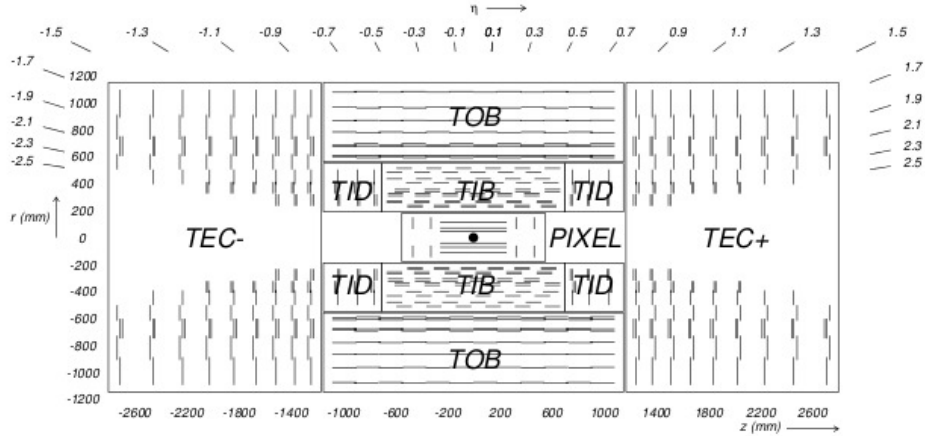


Figure 3.3: Tracker overview [1].

### Pixel detector

The part of the tracker closest to the beampipe is called pixel detector. It is placed between radii of 4 cm and 10 cm. The pixel detector is very important for the reconstruction of secondary vertices from  $b$  and  $c$  quarks and  $\tau$  leptons decays and for forming seeds for tracks which will be further reconstructed using other tracker layers and subdetectors. The lifetimes of the  $b$  and  $c$  quarks and the  $\tau$  leptons set the size of the pixel. Almost a quadratic shape of  $100 \mu\text{m}$  ( $r\phi$ )  $\times$   $150 \mu\text{m}$  ( $z$ ) is chosen which gives a comparable resolution in both directions. This gives the possibility to reconstruct the track in three dimensions and determine the collision vertex with very high precision.

There are three cylindrical layers and four discs of pixel detector modules respectively in the barrel and in the forward region. They can be seen in Figure 3.4. The pixel tracker, both in the barrel and endcaps, covers a pseudorapidity range of  $|\eta| < 2.5$ .

The inner layer is placed at 4.4 cm just surrounding the beam pipe. The other two layers are at radii of 7.3 and 10.2 cm. All three layers have length of 53 cm. In the forward region, there are four discs of pixel detector modules at  $z = \pm 34.5$  cm and  $z = \pm 46.5$  cm. The disc's inner radius is 6 cm and the outer radius is 15 cm.

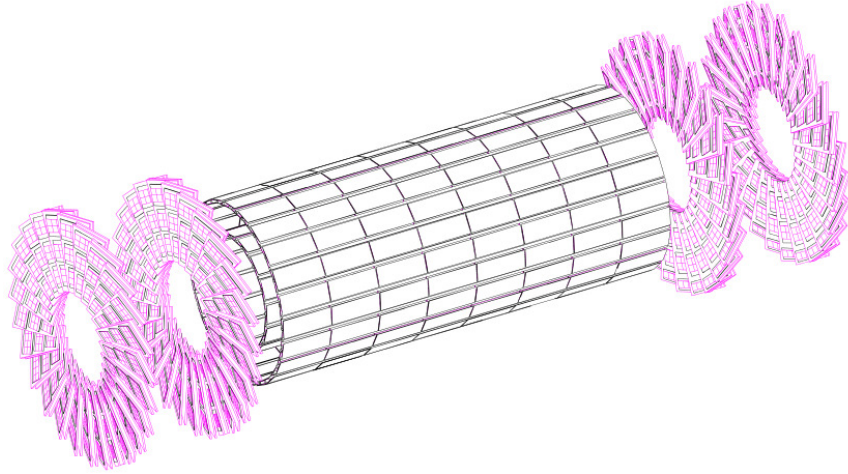


Figure 3.4: Pixel overview [1].

The barrel layers are made of 18, 30 and 42 ladders respectively for the first, second and third layer of the pixel detector. Each ladder is made up of 8 silicon modules. The 4 forward disks consist of 24 double sided blades arranged in a fan like structure. Each blade in the disk has 4 silicon modules on the side facing the interaction point and 3 silicon modules facing away. Each of the silicon modules consists of readout chips and sensors. In total, there are 1440 silicon modules in the pixel detector.

When a particle passes through a silicon module, electrons are ejected from the silicon atoms, creating electron-hole pairs. Each pixel collects these charges on the surface as a small electric signal. The readout chip amplifies the signal and as a result it indicates a hit in the pixel. To start building the trajectory of a charged particle, at least 3 hits in the three pixel layers are needed.

### **Silicon strip tracker**

At intermediate radii, between 20 and 130 cm, the particle flux is reduced significantly and silicon micro strip detectors are used with a size of 10 cm x 80  $\mu\text{m}$ .

The central barrel is divided in tracker inner barrel (TIB) with two inner endcaps (TID) covering the region between 20 cm and 60 cm, and a tracker outer barrel (TOB) covering the region above 60 cm radius. TIB consists of four layers assembled in shells, TID has three discs and TOB has six concentric layers. There are also two endcaps (TEC) with nine discs

on each side of the tracker. Each of the silicon strip tracker subdetector layers is made up of silicon modules designed specifically for its place. In total, there are 15148 silicon modules in the strip silicon tracker. Similarly to the pixel modules, silicon modules consists of sensors, support structure and readout electronics.

When a charged particle crosses a silicon module, electrons are ejected from the atoms. This small amount of current is amplified by readout chips producing hits in the module which allows to reconstruct the particle track. Track reconstruction of muons and converted photons using hits in the pixel and silicon strip tracker will be explained in Chapter 4.

The combined momentum resolution of the pixel and strip tracker is

$$\frac{\sigma(p_T)}{p_T} \propto 0.015\% p_T + 0.5\% \quad (3.2)$$

where  $p_T$  is transverse momentum of the charged particle and  $\sigma(p_T)$  is the uncertainty on  $p_T$ . The momentum resolution of 100 GeV/c track at  $\eta \propto 0$  is 1.5% and at  $\eta \propto 2.5$  is 7%.

### **Material budget in CMS Tracker**

A high track reconstruction efficiency is of great importance for the reconstruction of charged particle tracks. In general, the reconstruction efficiency is not limited by the resolution of the tracker. The inefficiency comes from hadronic interactions of the particles produced in the collisions with the material of the service installations inside the tracker. The service installations include on-detector electronics and cooling systems. Figure 3.5 shows the material budget in units of radiation length,  $X_0$ , as a function of pseudorapidity for different tracker layers and service installations. At  $\eta \approx 1.4$  there is an increase of the material budget because of cables and cooling pipes between the TIB and TOB, and the TID and TEC.

High material density increases the probability of bremsstrahlung, photon conversion and multiple scattering and is in conflict with the design requirements for the tracker. However, for this work it is important because the  $\chi_c$  are reconstructed with conversions in the tracker layers. To achieve high track reconstruction efficiency in high material density regions as well as in the whole tracker a special approach of "iterative" track reconstruction is used. This approach will be explained in Chapter 4.



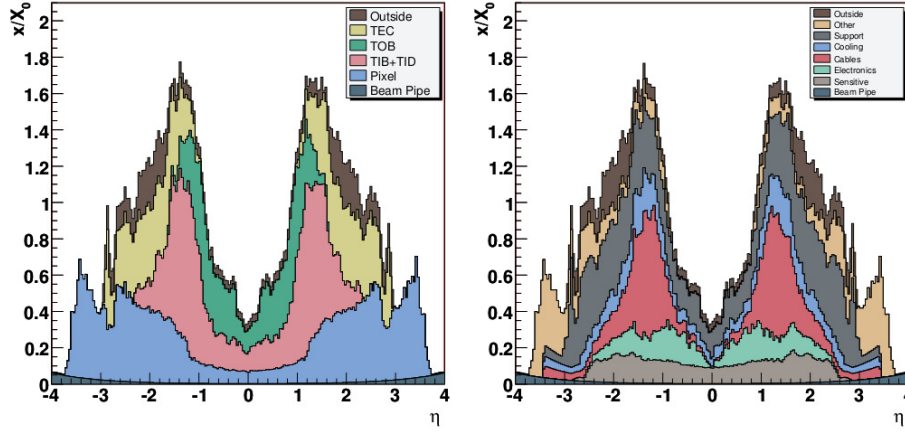


Figure 3.5: The material budget in units of radiation length as a function of  $\eta$  for different subdetectors (left) and functional contributions (right) [1].

### 3.3.3 Calorimetry

#### Electromagnetic Calorimeter

The electromagnetic calorimeter (ECAL) measures the energy and position of photons and electrons created in the collisions. The energy is measured by initiating interactions of these particles with the material of the ECAL and absorbing the resulting energy. It is in contrast to the tracker which absorbs only the deposited ionization energy.

The ECAL is made of lead tungstate ( $PbWO_4$ ) crystals chosen because of their excellent energy resolution. The layout of ECAL barrel and endcaps is shown in Figure 3.6.

The ECAL barrel covers the pseudorapidity range  $|\eta| < 1.479$  and contains 61200 crystals. The crystals have tapered shape with a front cross section of  $22 \times 22 \text{ mm}^2$ , rear cross section  $26 \times 26 \text{ mm}^2$  and length of 230 mm ( $25.8X_0$ ). The crystals are grouped into  $5 \times 2$  matrices. Then, 40 or 50 matrices are grouped into modules each containing 400 or 500 crystals. Four modules according to their position in  $\eta$  are assembled into supermodules, which thus contain 1700 crystals. Eighteen supermodules, each covering  $20^\circ$  in  $\phi$ , form a half barrel.

The ECAL endcaps cover pseudorapidity range  $1.479 < |\eta| < 3.0$  and contain 3662 crystals. Each endcap consists of identically shaped crystals with a rear cross section of  $30 \times 30 \text{ mm}^2$ , a front cross section of  $28.62 \times 28.62 \text{ mm}^2$  and 220 mm length ( $24.7X_0$ ). They are grouped in  $5 \times 5$  matrices to form supercrystals. The supercrystals are arranged in a rectangular grid.

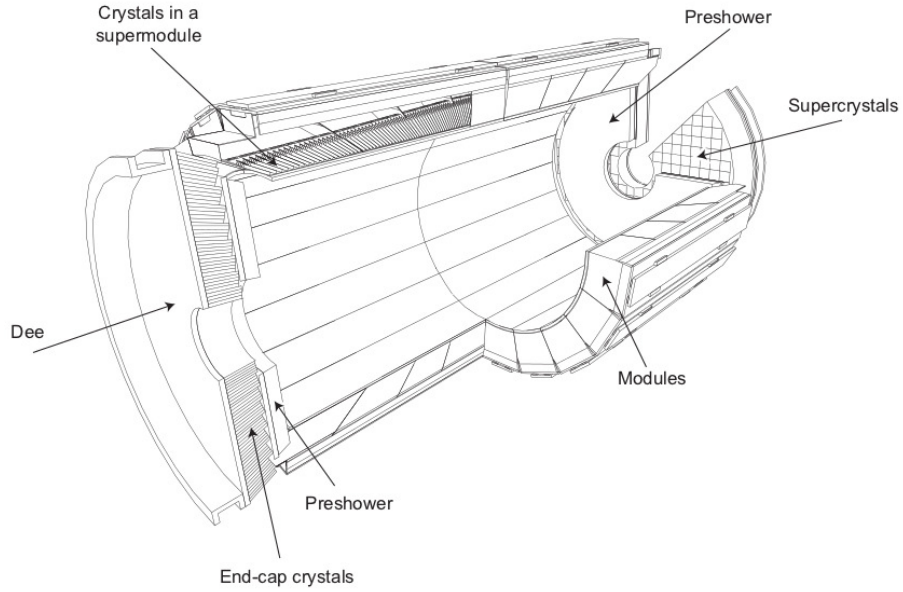


Figure 3.6: ECAL layout [1].

The energy resolution of  $PbWO_4$  crystals is

$$\frac{\sigma(E)}{E} \propto \frac{3\%}{\sqrt{E}} + 0.03\% \quad (3.3)$$

where  $\sigma(E)$  is the uncertainty on the measured energy and  $E$  is in GeV. For example energy resolution of 120 GeV electron is 0.5%.

When electrons and photons pass through the crystal it produces light in proportion to the particle's energy. The light is detected with photodetectors, avalanche photodiodes (APDs) in the barrel and vacuum phototriodes (VPTs) in the endcaps, which convert it into electrical signals.

A preshower detector is placed in front of the endcaps, in the region  $1.653 < |\eta| < 2.6$ , to improve  $\pi^0/\gamma$  discrimination. The preshower has a finer granularity than the ECAL and it can separate each of the two closely spaced photons from  $\pi^0$  decays.

### Hadron Calorimeter

The hadron calorimeter (HCAL) measures the energy of quarks and gluons by absorbing jets of particles the quarks and gluons hadronize into. The CMS hadron calorimeter is a sampling

calorimeter with brass absorber plates ( $\approx 5.5$  cm thick) and tiles of plastic scintillator (3.8 mm thin) as active medium. HCAL consists of four regions: barrel, endcap, forward and outer HCAL calorimeters, see Figure 3.7.

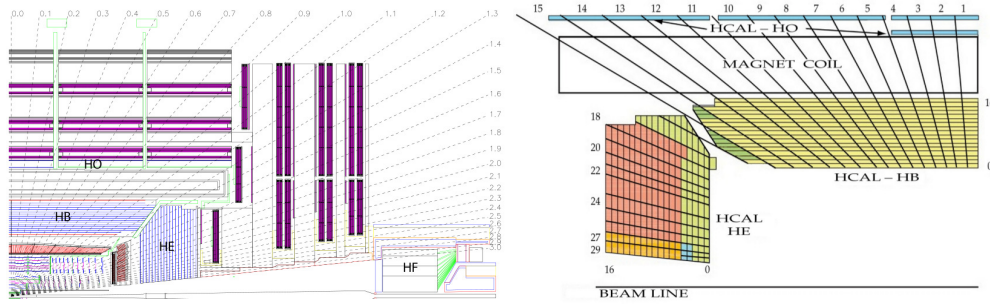


Figure 3.7: CMS view with locations for hadron barrel (HB), endcap (HE), outer (HO) and forward (HF) calorimeters (left) and HCAL tower segmentation of HB, HO and HE (right) [1].

The HCAL barrel (HB) is placed between the ECAL and the magnetic coil and covers pseudorapidity range  $|\eta| < 1.3$ . The HCAL endcap (HE) covers pseudorapidity range  $1.3 < |\eta| < 3$  and is attached to the muon endcap yoke. Both HB and HE use scintillator as active medium. The forward calorimeter (HF) has pseudorapidity coverage down to  $|\eta| = 5.2$  and is placed outside the magnetic field. The HF must be very resistant to radiation and due to this reason Cherenkov radiating quartz fibers are used as active medium.

The stopping power of HB and HE is not sufficient for hadron shower development, therefore the outer calorimeter (HO) is placed outside the magnetic coil. Similarly to HB and HE, it uses scintillator as active medium. The HO is used to identify late starting showers and to measure their deposited energy. The energy resolution of the HCAL is

$$\frac{\sigma(E)}{E} \propto \frac{100\%}{\sqrt{E}} + 5\% \quad (3.4)$$

where  $\sigma(E)$  is the uncertainty on the measured energy and  $E$  is in GeV.

When a hadronic particle passes through a plate of absorber it produces numerous secondary particles which can flow through successive absorber layers and create shower of particles. The particles pass also through active scintillation material causing them to emit light. A megatile is a layer of scintillator tiles chosen in a way to receive the same number of particles. Optic fibers collect the light from megatiles and feed the readout boxes where photodetectors

amplify the signal. The signals from successive tiles are added to form towers. The tower is the measure of particle's energy.

Figure 3.7 shows the HCAL tower segmentation in  $r$ - $z$  plane for HB, HO and HE detectors. The shading represents the grouping of scintillator layers into different readouts.

### **3.3.4 Magnet**

Magnetic field in the detector is needed in order to bend particle's trajectories and measure their momenta. The CMS magnet consists of two components: superconducting solenoid and yoke.

#### **Superconducting solenoid**

The superconducting solenoid has a magnetic field of 4 T and weights 220 t. It has dimensions of 6 m diameter and 12.5 m length. The solenoid is built in five modules which have 4 winding layers made from stabilized reinforced NbTi conductor. The thickness of the coil is  $3.9X_0$ . The inner coil radius accommodates the tracker, ECAL and HCAL.

#### **Iron yoke**

The magnetic flux is returned via 1.5 m thick and 10000 t weight iron yoke. It is segmented in 5 wheels along the beam pipe and has 2 endcaps. The iron yoke has 3 layers along its radius in the barrel and 3 discs perpendicular to the beam line in the endcaps, see Figure 3.8. Muon detectors are embedded in the iron structure of the yoke allowing 4 muon stations. The outer layer diameter of the yoke is 14 m.

### **3.3.5 Muon System**

The Muon system is designed to identify muons and measure their momenta. Muons are heavy and long-lived particles and they can cross large amount of matter without being stopped. The muons deposit only ionization energy in ECAL and HCAL while the other known final state particles except neutrinos are completely absorbed. There are 3 types of gaseous detectors especially designed for muon identification at CMS: drift tubes (DT), cathode strip chambers (CSC) and resistive plate chambers (RPC).

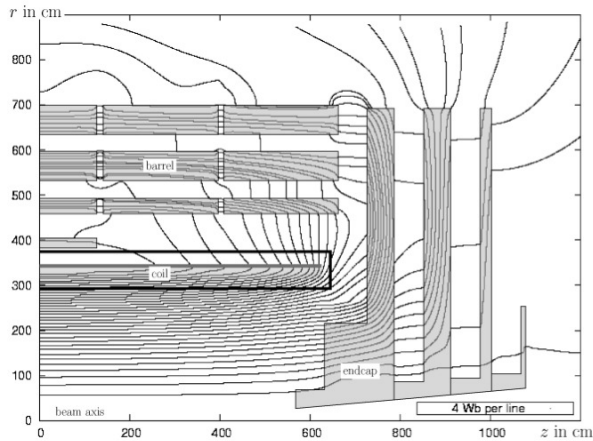


Figure 3.8: CMS iron yoke and field lines of the magnet [1].

### Drift tubes

In the barrel region, for  $|\eta| < 1.2$ , the neutron-induced background is small, the muon rate is low and the magnetic field is almost uniform and parallel to the beam line, see Figure 3.8, which implies the usage of DT chambers. They are sensitive to the magnetic field and have limited muon rate capability due to the long drift time. The DT chambers are organized in 4 stations among the layers of the return yoke. The first 3 stations contain 12 chambers per wheel, which measure the  $r$ - $\phi$  and  $z$  coordinates of the muons. The chambers in the fourth station are 14 per wheel and they measure only the  $r$ - $\phi$  coordinate of the muons. In each of the 12 sectors of the yoke there are 4 muon chambers per wheel, labeled MB1, MB2, MB3 and MB4, see Figure 3.9. In total, there are 250 DT chambers in the barrel.

The iron yoke supports between the chambers create dead zones for muon reconstruction. This has been solved by placing the DT chambers in a way the gaps not to align in  $\phi$ , see Figure 3.9.

### Cathode strip chambers

In the endcap region, the neutron-induced background is high and the magnetic field is large, non-uniform and radial, see Figure 3.8. This implies the usage of CSC chambers due to their short drift path, less sensitivity to the magnetic field and very good muon rate capability. There are 4 CSC stations in each endcap, placed among the plates of the return yoke which measure the muon position in  $r$ - $\phi$  plane. The CSC chambers have trapezoidal form (cover  $10^\circ$

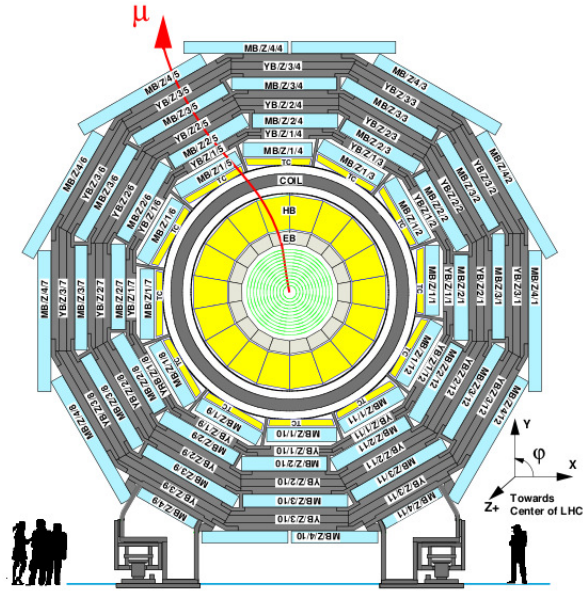


Figure 3.9: CMS muon DT chambers in one of the five wheels [1].

or  $20^\circ$  in  $\phi$ ) and they are arranged in groups: 72 ME1/1, 72 ME1/2, 72 ME1/3, 36 ME2/1, 72 ME2/2, 36 ME3/1, 72 ME3/2 and 36 ME4/1, see Figure 3.10. There are 540 CSC chambers in each endcap.

### Resistive plate chambers

In the back of each muon station there is one or more layers of RPC. Two RPC layers sandwich the first two barrel stations and one layer is placed in the outer two stations. There are four layers of RPC in each endcap.

The DTs and CSCs are designed to measure precisely muon's position while the RPCs are dedicated fast trigger detectors. They have excellent timing resolution of about 1 ns and can unambiguously identify the bunch crossing. There are 610 RPCs in CMS.

## 3.4 CMS Trigger

Due to the high rate of proton-proton interactions it will be impossible to store the large amount of data associated with these collisions. Production rate is reduced by selecting only interesting data in two steps: Level-1 Trigger (L1) and High-Level Trigger (HLT).

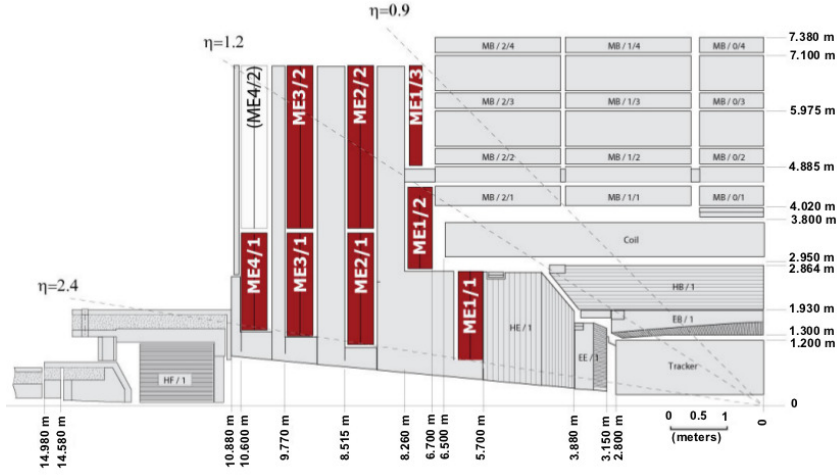


Figure 3.10: CMS CSC at the endcaps [1].

## Level-1 Trigger

The Level-1 Trigger consists of custom designed electronics with designed output rate of 50 kHz which means data rate reduction of the order of  $10^6$ . Since the designed bunch spacing of 25 ns is a very short time for Level-1 Trigger to read the data and provide a decision, the data is stored in front end buffers. The L1 Trigger takes a decision to keep data by combining information from the muon systems and the calorimeters. The trigger latency between given bunch crossing and the trigger decision is  $3.2 \mu\text{s}$  which is equivalent to 128 beam crossings of 25 ns.

The structure of the Level-1 Trigger is shown in Figure 3.11. It consists of three subsystems: calorimeter trigger, muon trigger and global trigger.

The muon trigger delivers the 4 highest  $p_T$  muons in each event. The calorimeter trigger sends the 4 most energetic objects from isolated and non-isolated  $e/\gamma$ , central jets, forward jets and tau-like jets. It also counts the number of jets, missing transverse energy,  $E_T^{miss}$ , and total transverse energy,  $E_T$ . Then, the Global Trigger takes the decision to accept or reject event based on up to 128 different algorithms with programmable thresholds applied in parallel to the objects delivered by the muon and calorimeter triggers.

At the end OR function combines the results from the algorithms and event is accepted or rejected. A positive decision causes the front end electronics to read the data from the de-

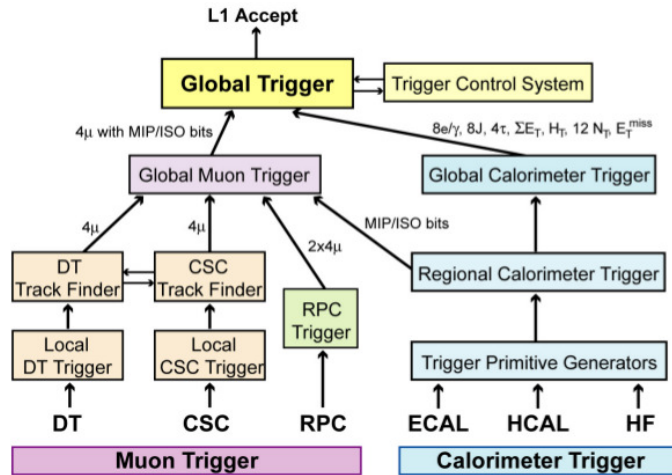


Figure 3.11: Level-1 Trigger structure [1].

tector and send it to a computer farm that performs more rigorous reconstruction of physics objects and further kinematic selections in order to accept or reject event (High-Level Trigger processing).

### High-Level Trigger

The High-Level Trigger is a software system implemented in a filter farm of about a thousand processors. It reduces the rate of stored events to 150 Hz. The HLT has access to complete read out data therefore it reconstructs physics objects like jets, electrons etc. as close as possible to the standard offline reconstruction code. The HLT is seeded by Level-1 and additionally uses information from the tracker and full granularity of the calorimeter and muon systems. The HLT contains many trigger paths each of them corresponding to a different selection like dimuons, diphotons etc. If an event is accepted by a given path, the HLT might not run the rest of the triggers. Later, the triggers not run online could be run offline allowing to study trigger efficiencies or producing specific data samples which can be easily analyzed by physicist. The HLT decision can be longer than  $3 \mu s$  but overall it is consistent with the Level-1 accept rate.

### 3.5 CMS data flow

Raw data that passed HLT and CMS Online Data Acquisition system (system which collects data from different detectors and builds events) is stored at a storage facility at CERN, known



as Tier-0. The raw data contains information for every single proton-proton collision which passed HLT and it is called an event. There are about  $10^9$  events per year stored at Tier-0. Standard CMS algorithms perform calibration and alignment of the detector using raw data and do prompt (first) reconstruction of physics objects like muons, electrons, jets etc. Later, their momenta, energies and trajectories are measured and this is done by using all detectors of CMS experiment.

The output data from prompt reconstruction is saved in different primary datasets based on trigger information.

The data from Tier-0 is transferred to Tier-1 storage facilities worldwide where further calibration and re-reconstruction is performed centrally to be used by all CMS analyzes. The Tier-2 centers are more numerous and they are based at different universities in the world. They have limited disk space and are used for running individual analysis and Monte Carlo simulations.

Data is stored in three types of root files which contain information about raw, reconstructed and analysis object data, respectively RAW, RECO and AOD root files. The RAW root files contain information about the recorded event in raw format as hits, energy deposits in the detector etc. The RECO root files contain detailed information of reconstructed physics objects and the AOD root files are simplified version of the RECO files which are mostly used in the analyses.

Tier-0, Tier-1 and Tier-2 centers form a GRID [39] based computer infrastructure in 35 countries.

# CHAPTER 4

## Measurement

### 4.1 Production and decay of $\chi_c$ states

The excited charmonium states  $\chi_c$  can be produced directly in proton-proton collisions or can be a product of  $b$ -hadron decays. The first is referred to as prompt, while the second is known as non-prompt  $\chi_c$  production. There is a distance between the production vertex of the  $b$ -hadron (secondary vertex) and the primary vertex where proton collisions occur. This distance depends on the life time of the  $b$ -hadron and is used to discriminate the two components of the  $\chi_c$  production process.

In this analysis, we are interested in prompt  $\chi_c$  production where the  $\chi_c$  further decays into  $J/\psi$  and photon,  $\chi_c \rightarrow J/\psi + \gamma$ . A schematic view of the two production processes is shown in Figure 4.1.

Table 4.1 summarizes some of the properties of the  $J/\psi$  and  $\chi_c$  charmonium states.

Table 4.1: Charmonium bound states.

Particle	Mass [ $MeV/c^2$ ]	Width [ $MeV/c^2$ ]	$\mathcal{B}(J/\psi \rightarrow \mu + \mu)$ [%]
$J/\psi$	$3096.92 \pm 0.01$	$0.093 \pm 0.002$	$5.93 \pm 0.06$
Particle	Mass [ $MeV/c^2$ ]	Width [ $MeV/c^2$ ]	$\mathcal{B}(\chi_{cJ} \rightarrow J/\psi + \gamma)$ [%]
$\chi_{c0}$	$3414.75 \pm 0.31$	$10.5 \pm 0.8$	$1.16 \pm 0.08$
$\chi_{c1}$	$3510.66 \pm 0.07$	$0.88 \pm 0.05$	$34.4 \pm 1.5$
$\chi_{c2}$	$3556.20 \pm 0.09$	$1.95 \pm 0.13$	$19.5 \pm 0.8$

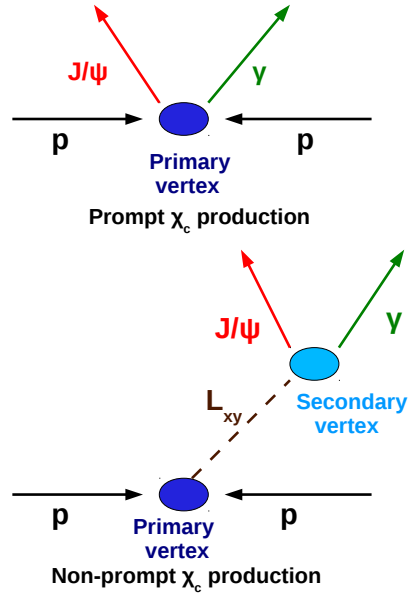


Figure 4.1: Prompt and non-prompt  $\chi_c$  production.

## 4.2 Data sample

The CMS experiment collected about  $5.56 \text{ fb}^{-1}$  of data in 2011 by colliding bunches of protons with different intensities at a center of mass energy of 7 TeV. For this measurement we use MuOnia data samples, produced centrally and based on data recorded with the CMS detector by using the  $B$ -Physics HLT dimuon resonant ( $J/\psi$ ,  $\Upsilon$ ,  $B_s$ ) and non-resonant (the two muons may not form a  $J/\psi$  or  $\Upsilon$  resonance) triggers. Table 4.2 contains a complete list of the MuOnia data samples and their corresponding run ranges. The run range indicates a specific period of collecting data with CMS with the same instantaneous luminosity of proton-proton collisions. The MuOnia data samples contain information of reconstructed physics objects like electrons, muons, jets etc for every event. The reconstruction of physics objects has been centrally performed and it was explained in Section 3.5.

A full description of  $B$ -Physics HLT triggers used for 2011 data can be found at [38]. In general, all  $B$ -Physics triggers are based on a selection of opposite sign muon pairs. Additionally for each trigger there is a cut on the transverse momentum  $p_T$ , rapidity  $|y_{\mu^+\mu^-}|$ , invariant mass

Table 4.2: Data samples used in the analysis.

Run range	Data sample
<b>Run 2011A</b>	
160404 – 163869	/MuOnia/Run2011A-May10ReReco-v1/AOD
165071 – 168437	/MuOnia/Run2011A-PromptReco-v4/AOD
170053 – 172619	/MuOnia/Run2011A-PromptReco-v5/AOD
172620 – 175770	/MuOnia/Run2011A-PromptReco-v6/AOD
<b>Run 2011B</b>	
175832 – 180252	/MuOnia/Run2011B-PromptReco-v1/AOD

$m_{\mu^+\mu^-}$ , displacement of the muon pair from the primary vertex etc. Figure 4.2 shows the contributions of several  $B$ -Physics triggers to the dimuon mass distribution obtained from MuOnia data sample. The steps in Figure 4.2 indicate usage of different triggers.

The 2011 data is divided into two periods: 2011A and 2011B. The 2011A period includes instantaneous luminosities  $5 \times 10^{32}$ ,  $1 \times 10^{33}$ ,  $1.4 \times 10^{33}$ ,  $2 \times 10^{33}$ ,  $3 \times 10^{33} \text{ cm}^{-2}\text{s}^{-1}$ . The second period is characterized by higher instantaneous luminosity of  $5 \times 10^{33} \text{ cm}^{-2}\text{s}^{-1}$  which leads to larger number of interactions per bunch crossing.

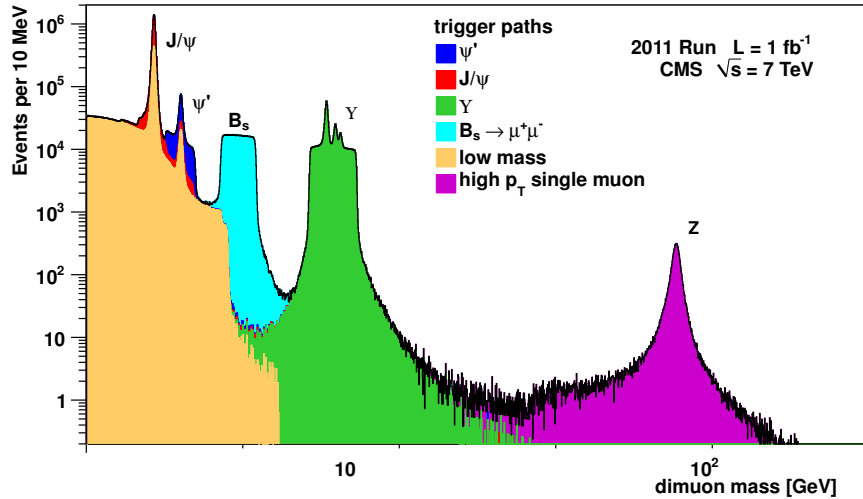


Figure 4.2: Dimuon mass distribution obtained from overlapping several trigger paths in narrow mass windows.

### 4.3 Triggers

To select events which contain a  $J/\psi$  candidate with specific selection criteria we apply the triggers in Table 4.3. These triggers are subset of the list of triggers in [38] used to produce MuOnia data samples. The triggers in Table 4.3 are applied additionally because the events in MuOnia data samples might not have been selected by those triggers (event is accepted if it fires at least one of the trigger paths in a list for a given run range).

The HLT trigger paths in Table 4.3 are characterized by two opposite charge muons, dimuon rapidity  $|y| < 1.25$ , momentum threshold for the pair that increases from 6.5 to 10 GeV, vertex  $\chi^2$  probability more than 0.005 (how likely is to observe as high or higher  $\chi^2$ ) and dimuon mass from 2.95 to 3.25 GeV/ $c^2$ . In Table 4.3 we report the instantaneous luminosities,  $\mathcal{L}$ , for each trigger path as well as their time-integrated luminosity given by

$$\mathcal{L}_{int} = \int \mathcal{L} dt. \quad (4.1)$$

Total integrated luminosity,  $\mathcal{L}_{int}$ , obtained from all trigger paths which corresponds to the total amount of data used in this analysis is 4.6 fb $^{-1}$ .

Table 4.3: Trigger paths used in the analysis.

Run range	Trigger path	$\mathcal{L}$ [cm $^{-2}$ s $^{-1}$ ]	$\mathcal{L}_{int}$ [pb $^{-1}$ ]
<b>Run 2011A</b>			
163269 – 163869	HLTDimuon6p5BarrelJpsiv1	$1 \times 10^{33}$	165.11
165088 – 166043	HLTDimuon7JpsiXBarrelv1	$1 \times 10^{33}$	722.94
166346 – 166346	HLTDimuon7JpsiXBarrelv2	$1 \times 10^{33}$	4.42
167078 – 167913	HLTDimuon7JpsiXBarrelv3	$1.4 \times 10^{33}$	244.54
170722 – 173198	HLTDimuon7JpsiXBarrelv5	$2 \times 10^{33}$	872.94
<b>Run 2011A and Run 2011B</b>			
173236 – 178380	HLTDimuon10JpsiBarrelv6	$3 \times 10^{33}$	1918.00
<b>Run 2011B</b>			
178421 – 179889	HLTDimuon10JpsiBarrelv9	$5 \times 10^{33}$	600.28
179959 – 180252	HLTDimuon10JpsiBarrelv10	$5 \times 10^{33}$	94.34
			<b>4.6 fb<math>^{-1}</math></b>

## 4.4 Candidate reconstruction and selection

The  $\chi_c$  is reconstructed through its decay to  $J/\psi$  and photon by using MuOnia data samples and triggers in Table 4.3. The  $J/\psi$ s are reconstructed using two opposite charge muons which have common vertex. The muons are detected in the muon chambers and tracker. The photons are reconstructed through conversions in the silicon pixel and strip tracker,  $\gamma \rightarrow e^+ + e^-$ .

### 4.4.1 Muons

Muons are produced with standard CMS reconstruction algorithms and they are stored in a dedicated collection for every event in the MuOnia data samples. There are three types of muons depending on the way of their reconstruction in the CMS detector:

- Stand-alone muons
- Tracker muons
- Global muons

**Stand-alone muons** are built using only the information from the muon system. The reconstruction starts by finding hit positions in DT, CSC and RPC. Then, hits within each of the DT and CSC chambers are matched to form seeds. The seeds are the starting point for trajectory building of muons. The track finding and fitting procedure based on a combinatorial Kalman filter [40] explores the next DT, CSC and RPC layers, adjacent to the layers where the seeds are formed, to build the muon trajectory.

Reconstruction of the **Tracker muons** starts from the tracker by considering all tracks above a certain minimum  $p_T$  which are later matched with at least one muon segment in the muon chambers. Muons are identified by their deposited energy in the electromagnetic calorimeter. The requirement is that the energy deposited in ECAL is compatible with a minimum ionizing particle. This approach of muon reconstruction works well for muons with  $p_T$  below 6 GeV/c when they can not reach the outer muon chambers. Tracker muons have a minimum momentum of 2.5 GeV/c.

**Global muons** are a combination of stand-alone muons and tracks in the silicon pixel and strip tracker. The muon track reconstructed in the muon chambers is matched with a track

reconstructed in the tracker. Global muons have a minimum momentum of 3 GeV/c.

The tracker and the muon systems play different roles in the muon reconstruction depending on its momentum scale. The tracker has high momentum resolution, about  $1 \div 2\%$  for 100 GeV/c particles and it is not much affected by multiple scattering and energy loss. The magnetic field in the tracker is homogeneous and almost constant. Therefore the tracker has very high efficiency in low  $p_T$  muon reconstruction. Moreover, the low  $p_T$  muons can not reach the muon stations because they lose energy in the material and bend in the magnetic field before reaching the muon system. On the other hand, the muon systems can reconstruct higher momentum muons because they can measure curvatures with a lever arm of  $4 \div 7$  m from the beamline as opposed to 1 m in the tracker (the higher the momentum of the muons is the less curved is its trajectory).

Knowing the trajectory's curvature of the muon, the tangent to the trajectory as well as the magnetic field one can find a relation between the momentum of the muon and its motion in magnetic field using Lorentz force. Low  $p_T$  muon's trajectory is a helix, while high  $p_T$  muon's trajectory is nearly a straight line. High  $p_T$  muons can emit photons leading to electromagnetic showers in the muon systems. This can cause a loss of efficiency in the reconstruction of high  $p_T$  muons.

In this analysis, we use two types of muons: reconstructed inside-out (Tracker muons) and reconstructed outside-in (Global muons). We apply additional selection cuts on the muon candidates as reconstructed with CMS standard algorithms to reject tracks that are not coming from muons. These cuts reject muon candidates, which may come from decays in flight from kaons and pions,  $K \rightarrow \mu$  and  $\pi \rightarrow \mu$ , or cosmic muons. Below is a list of selection requirements applied both to Global and Tracker muons:

- At least 11 hits in the tracker (pixel and strips layers) and no less than 2 hits in the pixel layers. This selection removes decays in flight from kaons and pions.
- The impact parameters  $d_0$  and  $z_0$  must have values of  $|d_0| < 4$  cm and  $|z_0| < 35$  cm with respect to the primary vertex to reject decays in flight and cosmic muons. The meanings of  $d_0$  and  $z_0$  are explained in Appendix A.
- Individual muon tracks are required to have  $p_T > 3.3$  GeV/c and  $|\eta| < 1.3$ .

- Two types of muons are used: "TrackerMuonOneStationTight" and "TrackerMuonArbitrated". For the first type, the silicon track is matched to two segments in the muon chambers. For the second type, an arbitration process is used to assign segments in the muon chambers uniquely to the muon tracks.
- Fit to the trajectory of Tracker muon in the Tracker is required to have  $\chi^2/ndf < 4.0$  to suppress muons from decays in flight.
- Fit to the trajectory of Global muon is required to have  $\chi^2/ndf < 1.8$  in the tracker and  $\chi^2/ndf < 20.0$  in the muon systems to suppress muons from decays in flight.

#### 4.4.2 $J/\psi$ candidates

We reconstruct the  $J/\psi$  using opposite sign Global and Tracker muons by building different muon pair combinations: Global-Global, Global-Tracker and Tracker-Tracker.

After pairing the two opposite charge muons, their trajectories are fitted with a common vertex constraint. The vertex fit  $\chi^2$  probability is required to be larger than 1%. If more than one muon pairs is found in the event, only the pair with largest vertex  $\chi^2$  probability is retained. In addition, it is required that the dimuon mass is in the  $J/\psi$  mass range 3.0 and 3.2 GeV/c<sup>2</sup> and the rapidity of the muon pair is in the interval  $[-1, 1]$ . We chose  $J/\psi$  to be in the barrel region of the detector because photons, which do not fly very far from  $J/\psi$ , can be poorly reconstructed in the forward region of the tracker.

Figure 4.3 shows the invariant mass spectrum of the muon pair with muon cuts from Section 4.4.1 and vertex probability cuts. The  $J/\psi$  and  $\psi'$  peaks are clearly visible. The steps in the plot correspond to the usage of different dimuon triggers.

#### 4.4.3 Converted photons

##### Electron and positron tracks

The  $\chi_c$  photons are characterized with very low momenta,  $p_T < 5$  GeV/c. They can not reach the ECAL and due to the substantial material budget in the silicon pixel and strip trackers they often convert into electron-positron pairs. Electron-positron pairs from converted photons



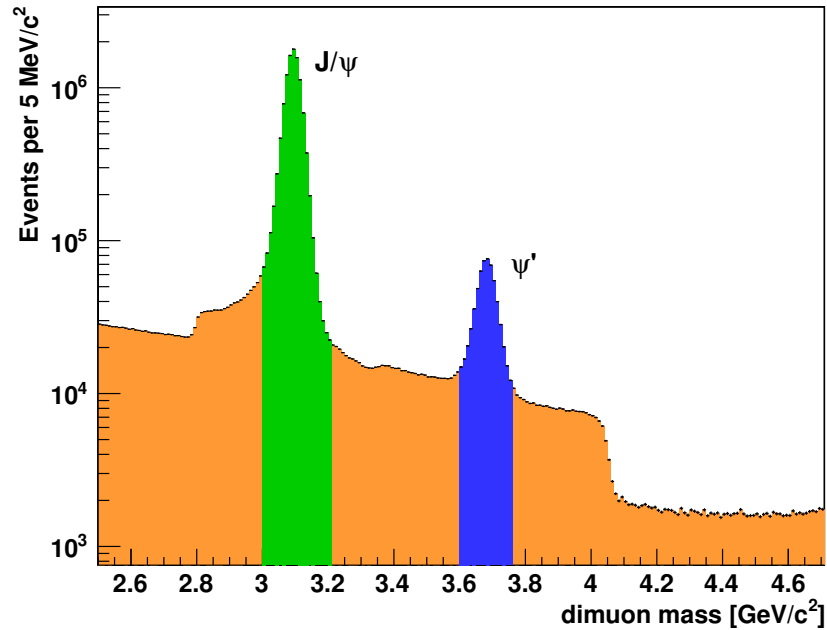


Figure 4.3: Invariant mass distribution of  $J/\psi$  candidates with muon and vertex probability cuts. The steps in the plot correspond to different dimuon trigger paths.

originate from a conversion vertex which is a displaced vertex from the interaction point (collision point). The two tracks from the electron-positron pair are parallel at the conversion vertex, both in the transverse and longitudinal frame of the detector. The tracks later open in the transverse plane because of the bending in the solenoidal magnetic field. The invariant mass of the converted photon is zero.

Similarly to the muon candidates, the conversion candidates (electron and positron tracks) are reconstructed with standard CMS reconstruction algorithms and stored in a dedicated collection for each event in MuOnia data sample.

There are two algorithms of track reconstruction from conversions in CMS:

- Tracker only seeded tracks
- ECAL seeded tracks

The **Tracker only seeded reconstruction algorithm** starts building a track trajectory from seed hits in the pixel and silicon strip tracker. **ECAL seeded tracks algorithm** also starts

trajectory building from hits in the pixel tracker but the seed hits are found using the electron energy deposited in ECAL superclusters. The second method is not applicable for the reconstruction of photons coming from  $\chi_c$ . The  $\chi_c$  photons have very low  $p_T$  and both electrons have difficulties reaching the calorimeter.

Both algorithms, the **Tracker only seeded** and **ECAL seeded** reconstructions, are based on the default track reconstruction in CMS which uses Kalman Filter method [40]. When electrons traverse tracker material they lose energy by emitting photons through bremsstrahlung. In general, the amount of emitted bremsstrahlung depends on the amount of the tracker material which varies significantly with  $\eta$  (Section 3.3.2). Within the Kalman Filter method, the radiation energy loss is taken into account by correcting the track momentum. It is assumed, that all fluctuations of track parameters due to material budget has Gaussian form. In reality, the energy fluctuations increase with increasing material budget in the tracker. Therefore a nonlinear approach is needed for electron and positron track reconstruction. This is achieved by Gaussian Sum Filter algorithm [41] which is a generalization of the Kalman Filter method.

For the electron-positron tracks from  $\chi_c$  converted photons, we use Tracker only seeded tracks, reconstructed with Kalman Filter method. Below we explain how electron and positron trajectories are built using the CMS track reconstruction algorithms.

### **Building electron and positron trajectories**

Track reconstruction starts with hits in the pixel and silicon strip trackers. These hits are the initial estimate of the track trajectory and are also called seeds. The seeds are propagated out-ward to search for compatible hits in the neighboring tracker layers. When new hits are found they are added to the track trajectory and the track parameters and uncertainties are recalculated by using Kalman Filter or Gaussian Sum Filter methods. The search continues until the end of the tracker is reached or no new compatible hits are found. Several track candidates are produced from each seed.

Several iterations of trajectory finding are performed. In the first iteration, all reconstructed hits are used and the requirement on the trajectory parameters are most stringent. Hits that are assigned to a track in one iteration are removed from the collection of hits used in the subsequent iterations and the requirements are less restrictive. At the end of each iteration, tracks are filtered to remove the ones which are fake. Fake tracks do not have good fit  $\chi^2$

probability and are often not compatible with the primary vertices.

Below is a list of track parameters. Depending on the values of these parameters, the tracks are grouped in different quality categories and used for different purposes.

- track normalized fit  $\chi^2$
- number of hits used for building track trajectory
- number of tracker layers with a hit on the track trajectory
- number of layers with missing hits between the first and the last hit on the track trajectory
- transverse momentum  $p_T$  of the track
- transverse impact parameter  $d_0$  with respect to the mean proton-proton collision (Appendix A)
- significance of the transverse impact parameter  $d_0/\sigma$ ,  $\sigma$  is the uncertainty on  $d_0$
- longitudinal impact parameter  $z_0$  with respect to the primary vertex (Appendix A)
- significance of the longitudinal impact parameter  $z_0/\sigma$ ,  $\sigma$  is the uncertainty on  $z_0$

We require that at least 4 hits are used for building electron and positron tracks with  $\chi^2/ndf$  less than 10. There are no further requirements on the remaining parameters from the list above. Tighter requirements on those parameters will decrease the efficiency of our converted photons.

### **Converted photon selection cuts**

In addition to the selection cuts on electron and positron trajectories applied above, there are further selection requirements which include both tracks:

- The two tracks must have opposite charge.
- The charge-signed impact parameter  $q \cdot d_0$  must be positive,  $q \cdot d_0 > 0$ , where  $q$  is the track's charge and  $d_0$  is transverse impact parameter. This means conversion vertex lies outside electron and positron helices.

- Helices transform into circles when projected onto the transverse plane. The distance of minimum approach in the transverse plane,  $d_m$ , between two points of tangent approach of the two tracks helices must be between  $-0.25$  and  $1$  cm. Figure 4.4 shows the meaning of the parameter  $d_m$ , defined as  $d_{O_1-O_2} - (R_1 - R_2)$ , where  $d_{O_1-O_2}$  is the distance between the centers of the two tracks circles and  $R_1$  and  $R_2$  are the two circles radii. The parameter  $d_m$  is negative when the two tracks circles are intersecting. The upper cut on  $d_m$  is used to reject tracks that bend around in the magnetic field and travel backward also known as "loopers". The "loopers" have a spiral trajectory and they lose energy with every turn.

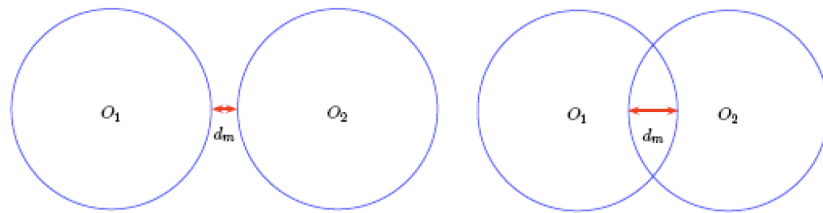


Figure 4.4: Example of a positive (left) and a negative (right) distance of minimum approach between two ideal track circles [42].

- The difference in  $z$ ,  $\Delta_z$ , of the innermost hits in a track pair must be less than  $5$  cm.
- The two tracks must have one of the two innermost hits in the same tracker layer. This is to reduce fake tracks coming from loopers.
- Transverse momentum,  $p_T$ , of the converted photon should be more than  $0.5$  GeV/c. This cut reduces the number of fake converted photons significantly.

Electron and positron track are fitted with a common 3D-constrained kinematic vertex fitter which imposes the tracks to be parallel in both the transverse and longitudinal planes. The pair is retained if the fit converges and its  $\chi^2$  probability is greater than  $5 \times 10^{-4}$ .

The selection cuts above are standard requirements which are applied on conversions in CMS tracker.

Additionally to the standard requirements, we require the conversion vertex to be at a transverse distance larger than  $1.5$  cm from the center of the beam pipe (radius of the beam pipe is

$\sim 3$  cm). This cut reduces the number of fake track pairs originating from the primary vertex as in the case of the Dalitz decay of the  $\pi^0$ ,  $\pi^0 \rightarrow \gamma e^+ e^-$ .

Figure 4.5 shows the distribution of the reconstructed vertices with respect to the center of the CMS detector in the silicon pixel and strip trackers and Figure 4.6 shows their distribution in  $x$ - $y$  plane in the pixel tracker. Figure 4.5 shows that most of the conversions occur in the first three layers of the pixel tracker.

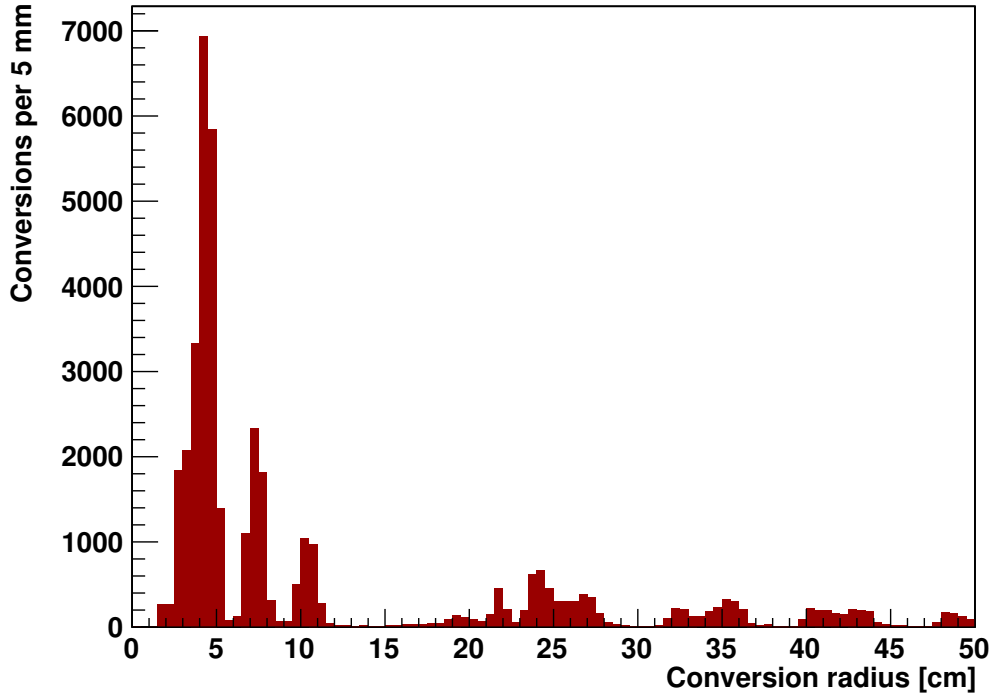


Figure 4.5: Conversion vertices distributions in radial plane in silicon pixel and strip (TIB) trackers. Most conversions occur in the three pixel layers placed at 4.4, 7.3 and 10.2 cm.

Each conversion track candidate must be compatible in  $z$  with at least one reconstructed primary vertex. This is ensured by requiring that the longitudinal impact parameter  $z_0$  of the conversion track with respect to the primary vertex satisfies  $|z_0/\sigma| < 5$ , where  $\sigma$  is the uncertainty on  $z_0$ . The primary vertices in proton-proton collisions are centrally reconstructed with special CMS algorithms from selected tracks for each event. Additionally, we require that the number of the tracks from the primary vertices is at least 4, corresponding to the muons and electrons tracks. Among the two primary vertices closest in  $z$  to each of the  $e^+$  and  $e^-$  tracks, at least one must be common to the two tracks.

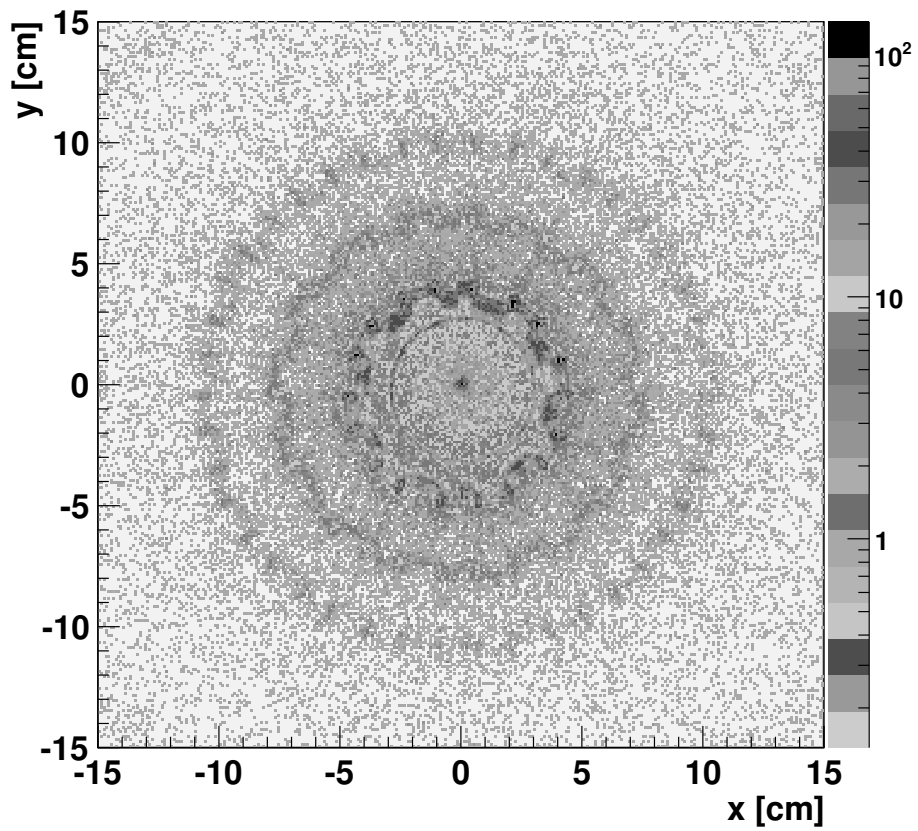


Figure 4.6:  $x$ - $y$  distribution in the pixel detector region of the position of the reconstructed conversion vertex. The beam pipe at radius of  $\sim 3$  cm is clearly visible, off-centered with respect to the pixel detector, as well as the three pixel layers with radii of 4.4, 7.3 and 10.2 cm.

A reconstructed primary vertex from proton-proton collision is assigned to the reconstructed conversion by projecting the photon momentum along the beamline and by choosing the closest vertex along the  $z$  direction. If the distance along the  $z$  between the vertex and the projected photon momentum,  $\Delta z$ , is larger than five times its uncertainty ( $|\Delta z/\sigma| < 5$ ,  $\sigma$  is the uncertainty on  $\Delta z$ ) the candidate is rejected.

#### 4.4.4 $\chi_c$ candidates

Each conversion candidate with selection cuts in Section 4.4.3 is associated to every other conversion candidate in the event and to every photon reconstructed with electromagnetic calorimeter. Any conversion building up a pair which invariant mass falls in the range between 0.11 and 0.15 GeV/ $c^2$  is rejected, since it is assumed to originate from a  $\pi^0$  decay,  $\pi^0 \rightarrow \gamma\gamma$ .

The primary vertex associated to the conversion is required to be compatible with the reconstructed  $J/\psi$  vertex. This requirement is fulfilled when the three-dimensional distance between the two vertices,  $D$ , satisfies  $|D/\sigma| < 5$  where  $\sigma$  is the uncertainty on  $D$ .

We are interested in a prompt  $\chi_c$  production and this implies its decay product, the  $J/\psi$ , to be also promptly produced in the proton-proton collisions. The  $J/\psi$  from the decay of  $b$ -hadrons is displaced from the primary vertex where the  $b$ -hadrons are produced. The 3D decay length of  $b$ -hadrons or the distance between the primary vertex and the  $b$ -hadron decay vertex is

$$L = \beta\gamma ct \tag{4.2}$$

where  $c$  is the speed of light,  $t$  is the proper lifetime of the  $b$ -hadron,  $\beta = v/c$  where  $v$  is the speed of the  $b$ -hadron and  $\gamma$  is the Lorentz boost defined as  $1/\sqrt{1-\beta^2}$ . The transverse decay length of  $b$ -hadrons in  $x$ - $y$  plane of the detector is

$$L_{xy} = \beta_T \gamma ct \tag{4.3}$$

and it can be used to separate the  $J/\psi$  produced in  $b$  decays from prompt  $J/\psi$ . For events with  $J/\psi$   $p_T$  greater than 1.25 GeV/ $c$ , the  $J/\psi$  flight direction aligns well with that of the  $b$ -hadron [43]. Therefore  $L_{xy}$  can be written as

$$L_{xy} = \vec{L} \cdot \frac{\vec{p}_T(J/\psi)}{|p_T(J/\psi)|} \quad (4.4)$$

where  $\vec{L}$  is the vector from the primary vertex to the  $J/\psi$  decay vertex in the  $r$ - $\phi$  plane and  $\vec{p}_T(J/\psi)$  is the transverse momentum vector in  $x$ - $y$  plane. A variable called pseudo-proper decay length,  $\ell_{J/\psi}$ , is used to discriminate between the  $J/\psi$  prompt and non-prompt components and it is derived from Equations 4.3 and 4.4 by using  $\beta_T \gamma = p_T(J/\psi)/m_{J/\psi}$

$$\ell_{J/\psi} \equiv ct = \frac{L_{xy}}{\beta_T \gamma} = L_{xy} \cdot \frac{m_{J/\psi}}{p_T(J/\psi)} \quad (4.5)$$

where  $m_{J/\psi}$  is the mass of the  $J/\psi$  and  $L_{xy}$  is measured by using Equation 4.4. Prompt  $J/\psi$  has a zero pseudo-proper decay length whereas non-prompt  $J/\psi$  has an exponentially decaying pseudo-proper length distribution due to the lifetime of the  $b$ -hadrons. The distribution of the pseudo-proper decay length,  $\ell_{J/\psi}$ , of the  $J/\psi$  from  $\chi_c$  candidates is illustrated in Figure 4.7.

We apply a cut of  $30 \mu\text{m}$  to the pseudo-proper decay length of the  $J/\psi$  to select its prompt component. To evaluate the contamination from non-prompt  $J/\psi$  in the region  $\ell_{J/\psi} < 30 \mu\text{m}$ , we perform an unbinned maximum likelihood fit to the pseudo-proper decay length of the  $J/\psi$ . In an ideal detector, the  $\ell_{J/\psi}$  should be zero for the prompt events. Therefore for the prompt component we use a resolution function which is taken to be a double Gaussian Probability Distribution Function (PDF). The  $J/\psi$  shape of the non-prompt component is given by convolving the same resolution function with an exponential decay function of a  $b$ -hadron. Figure 4.7 illustrates the fit to the pseudo-proper decay length of the  $J/\psi$ . We calculated the fraction of the non-prompt component of the  $J/\psi$  in the region  $\ell_{J/\psi} < 30 \mu\text{m}$  to be around 8%. This has been done by counting the number of non-prompt  $J/\psi$  events with respect to the number of prompt  $J/\psi$  events in the region  $\ell_{J/\psi} < 30 \mu\text{m}$ . A contamination from background was not taken into account.

All the selection cuts used to define the  $\chi_c$  candidates are summarized in Table 4.4.

## 4.5 Production ratio - definition

Cross section in high energy physics characterizes the probability that a particular reaction between interacting particles will take place. It can be found by counting the number of



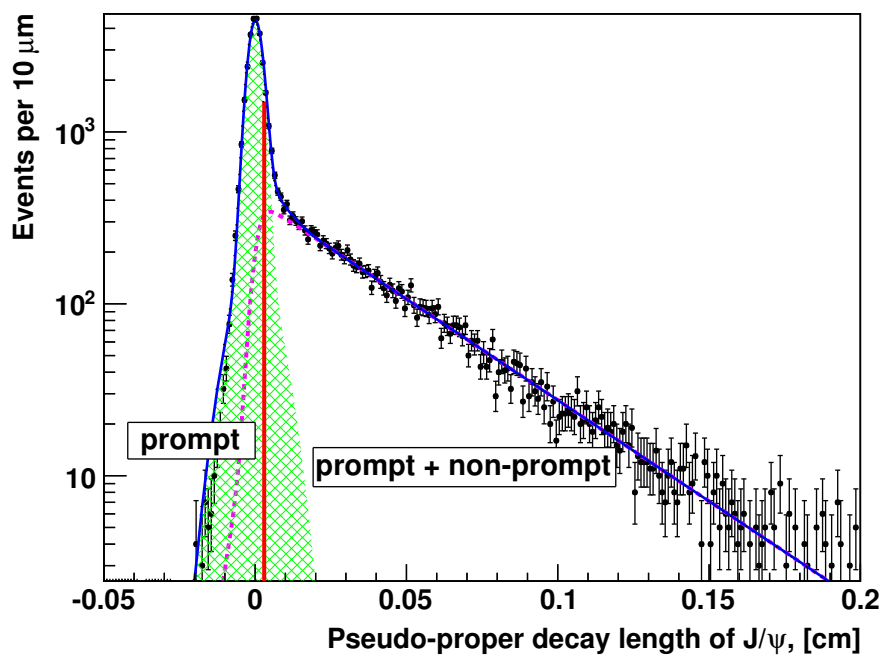


Figure 4.7: Pseudo-proper decay length distribution of  $J/\psi$  from the selected  $\chi_c$  candidates. The prompt component is shown in green, the non-prompt component is in lilac and the prompt + non-prompt component is in blue. A cut of  $30 \mu\text{m}$  to the pseudo-proper decay length shown in red selects the prompt component of  $J/\psi$ .

Table 4.4: Summary of the cuts used to select  $\chi_c$  candidates.

<b>Muon selection</b>	
track fit $\chi^2/ndf$	< 4.0 (Tracker muons in the tracker)
track fit $\chi^2/ndf$	< 1.8 (Global muons in the tracker)
track fit $\chi^2/ndf$	< 20.0 (Global muons in the muon system)
hits in pixel	$\geq 2$
hits in tracker	$\geq 11$
Fiducial cylinder	4 cm(r) $\times$ 35 cm(z)
$p_T(\mu),  \eta  < 1.3$	3.3 GeV/c
Muon ID	TrackerMuonArbitrated and TrackerMuonOneStationTight
<b>Photon conversion selection</b>	
Electron track hits	$\geq 4$
Electron track fit $\chi^2/ndf$	< 10
Distance of approach	$-0.25 \text{ cm} < d_m < 1 \text{ cm}$
Electron track-primary vertex comp.	$ z_0/\sigma  < 5$
Signed impact parameter	$q \cdot d_0 > 0$
$e^+e^-$ vertex fit probability	$> 5 \times 10^{-4}$
$e^+e^-$ vertex-primary vertex comp.	$ \Delta z/\sigma  < 5$
Radius of conversion	$R_{conv} > 1.5 \text{ cm}$
$p_T(\gamma)$	$> 0.5 \text{ GeV}/c$
<b>J/<math>\psi</math> selection</b>	
$\mu^+\mu^-$ vertex fit probability	$> 0.01$
$m_{\mu^+\mu^-}$	3.0 – 3.2 GeV/c <sup>2</sup>
$ y(\mu^+\mu^-) $	< 1
<b><math>\chi_c</math> selection</b>	
$\pi^0$ rejection	$m_{\gamma\gamma} < 0.11 \text{ GeV}/c^2$ and $m_{\gamma\gamma} > 0.15 \text{ GeV}/c^2$
Photon-J/ $\psi$ vertex compatibility	$ D/\sigma  < 5$
Prompt component selection	$\ell_{J/\psi} < 30 \mu\text{m}$

observed events in a particular decay process.

The cross section of a given decay process is measured as

$$\sigma = \frac{N_{obs} - N_{bkg}}{\mathcal{L}_{int} \cdot \epsilon \cdot A_{cc} \cdot \mathcal{B}} \quad (4.6)$$

where  $N_{obs}$  is the total number of observed events and  $N_{bkg}$  is the number of background events which mimic the signal decay topology. The difference of the two numbers gives the number of observed signal events. The coefficient  $A_{cc}$  is the geometrical acceptance and the coefficient  $\epsilon$  is the reconstruction efficiency of the decay products. The acceptance and efficiency are needed to correct the number of observed events to the number of expected

events given imperfect detector. Coefficient  $\mathcal{B}$  is the branching ratio and it is the fraction of particles which decay by an individual decay mode with respect to the total number of particles which can decay. Coefficient  $\mathcal{L}_{int}$  is the total amount of collected data also known as integrated luminosity defined in Chapter 3.

In this measurement, we are not interested in the absolute value of the cross section but rather in its shape. The ratio of cross sections can provide this information. In the ratio, large systematic uncertainties cancel. The ratio of the production cross sections of  $\chi_{c2}$  and  $\chi_{c1}$  is given by the formula

$$\frac{\sigma(pp \rightarrow \chi_{c2} + X)\mathcal{B}(\chi_{c2} \rightarrow J/\psi + \gamma)}{\sigma(pp \rightarrow \chi_{c1} + X)\mathcal{B}(\chi_{c1} \rightarrow J/\psi + \gamma)} = \frac{N_{\chi_{c2}}}{N_{\chi_{c1}}} \cdot \frac{\epsilon_1}{\epsilon_2} \quad (4.7)$$

where  $N_{\chi_{c1}}$  and  $N_{\chi_{c2}}$  are the number of reconstructed  $\chi_{c1}$  and  $\chi_{c2}$  candidates from data. The term  $\epsilon_1/\epsilon_2$  is the ratio of the geometric acceptances multiplied by the ratio of reconstruction efficiencies of the  $\chi_{c1}$  and  $\chi_{c2}$  candidates defined as  $(\epsilon \cdot A_{cc})_{\chi_{c1}}/(\epsilon \cdot A_{cc})_{\chi_{c2}}$  in Equation 4.6. Its value is derived from a full detector simulation and will be described Section 4.7. The values of the branching ratios,  $\mathcal{B}(\chi_{c2} \rightarrow J/\psi + \gamma)$  and  $\mathcal{B}(\chi_{c1} \rightarrow J/\psi + \gamma)$ , are taken from PDG [44] and they will be used to calculate the total production ratio

$$\frac{\sigma(pp \rightarrow \chi_{c2} + X)}{\sigma(pp \rightarrow \chi_{c1} + X)} = \frac{N_{\chi_{c2}}}{N_{\chi_{c1}}} \cdot \frac{\epsilon_1}{\epsilon_2} \cdot \frac{\mathcal{B}(\chi_{c1} \rightarrow J/\psi + \gamma)}{\mathcal{B}(\chi_{c2} \rightarrow J/\psi + \gamma)}. \quad (4.8)$$

## 4.6 Data analysis

### 4.6.1 Unbinned maximum likelihood fit

The identification of  $\chi_c$  is done using the invariant mass of  $\mu^+\mu^-$  in the  $J/\psi$  mass window  $3.0 \div 3.2 \text{ GeV}/c^2$  and  $\gamma$

$$m_{\chi_c}^2 = (p_{\mu^+\mu^-} + p_\gamma)^2 = (E_{\mu^+\mu^-} + E_\gamma)^2 - (\vec{p}_{\mu^+\mu^-} + \vec{p}_\gamma)^2 \quad (4.9)$$

where  $p_{\mu^+\mu^-}$  and  $p_\gamma$  are four momenta of  $\mu^+\mu^-$  and  $\gamma$ ,  $E$  and  $\vec{p}$  are their energies and momenta.

Then the energy and momentum of  $\chi_c$  are

$$\begin{aligned}
E_{\chi_c} &= E_{\mu^+\mu^-} + E_\gamma \\
\vec{p}_{\chi_c} &= \vec{p}_{\mu^+\mu^-} + \vec{p}_\gamma.
\end{aligned}
\tag{4.10}$$

Therefore we expect to see a narrow peak in the invariant mass distribution,  $dN/dm_{\chi_c}$ . The reconstructed width of  $\chi_c$  will be influenced by the resolution of the  $J/\psi$  and the photon. The natural width of  $J/\psi$  is  $0.093 \text{ MeV}/c^2$  therefore the reconstruction of  $\mu^+\mu^-$  pair is only limited by the accuracy of its measurement with CMS detector known as resolution. For  $|y_{J/\psi}| < 1.2$ , the width of  $J/\psi$  was measured to be  $\sigma = 28 \text{ MeV}/c^2$  [45].

In order to reduce the uncertainty due to the finite resolution of the  $\mu^+\mu^-$  pair with the CMS detector we build the mass difference spectrum,  $Q = m_{\gamma\mu\mu} - m_{\mu\mu} + m_{J/\psi}^{PDG}$  ( $m_{J/\psi}^{PDG}$  is the mass of  $J/\psi$  taken from PDG). Then we perform an unbinned extended maximum likelihood fit to the mass difference spectrum  $Q$  in various  $p_T$  ranges of  $J/\psi$  using RooFit [46] to find the number of reconstructed  $\chi_{c1}$  and  $\chi_{c2}$ ,  $N_{\chi_{c1}}$  and  $N_{\chi_{c2}}$ . For detailed information about the maximum likelihood fits see Appendix B. The Probability Distribution Function (PDF) used for the unbinned extended maximum likelihood fit is

$$P(Q) = \sum_{\chi_{cJ}} N_{\chi_{cJ}} \cdot S_{\chi_{cJ}}(Q) + N_B \cdot S_B(Q)
\tag{4.11}$$

where  $N_{\chi_{cJ}}$  is the number of signal events for each resonance,  $S_{\chi_{cJ}}(Q)$  is the signal PDF for each resonance,  $N_B$  is the number of background events and  $S_B(Q)$  is the background PDF.

### Signal probability distribution function

Since the  $\chi_c$  states have a finite lifetime, their invariant mass is not a fixed number. The uncertainty in their mass is inversely proportional to their lifetime also known as width. Usually experimental distributions (for example invariant mass distribution) are result of a theoretical distribution modified by a detector resolution function.

The  $\chi_c$  states have a small intrinsic width:  $0.88 \text{ MeV}/c^2$  for  $\chi_{c1}$  and  $1.95 \text{ MeV}/c^2$  for  $\chi_{c2}$  (see Table 4.1), therefore, their invariant mass distributions are dominated by the experimental resolution of the detector.

The shape of the resolution function was studied using Monte Carlo simulation. This was

motivated by the fact that  $\chi_{c1}$  and  $\chi_{c2}$  states have very close masses and the two peaks can not be separated to obtain a reliable parametrization of the resolution functions from data directly. For example, the tail of the  $\chi_{c2}$  mass distribution falls under the  $\chi_{c1}$  peak and the tail of  $\chi_{c1}$  ends up under the  $\chi_{c0}$  peak.

We generated separate samples of  $\chi_{c1}$  and  $\chi_{c2}$  with a Monte Carlo generator and processed the events through full CMS detector simulation. Details on this procedure will be given in Section 4.7. Then, we fit the invariant mass distribution  $m_{\gamma\mu\mu} - m_{\mu\mu} + m_{J/\psi}^{PDG}$  and extract the resolution function parameters for  $\chi_{c1}$  and  $\chi_{c2}$ . Since we build the mass difference  $m_{\gamma\mu\mu} - m_{\mu\mu}$ , this is indeed the resolution function of the converted photon.

From the simulation, we observe that the resolution function of the converted photon has three components: Gaussian core, left and right exponential tails. The Gaussian component describes the detector intrinsic energy resolution, while the exponential tails correspond to unrecovered energy losses of reconstructed electrons and other detector effects.

The mass distributions of  $\chi_{c1}$  and  $\chi_{c2}$  states from simulation are parametrized with Double Crystal Ball function [48] which is composed of a Gaussian and two exponential tails. The Gaussian is described by two parameters: mean mass  $m$  and width  $\sigma$ . The exponential tails are described by four parameters:  $\alpha_{l,r}$  account for the transition point between Gaussian and exponential and  $n_{l,r}$  are exponential coefficients. The Double Crystal Ball is defined as

$$S(Q; \alpha, n, \sigma, m) = \begin{cases} \left( \frac{n_l}{|\alpha_l|} \right)^{n_l} e^{-\frac{1}{2}\alpha_l^2} & \text{for } \frac{Q-m}{\sigma} \leq -\alpha_l, \\ \left( \frac{n_l}{|\alpha_l| - |\alpha_l| - \frac{Q-m}{\sigma}} \right)^{n_l} & \text{for } -\alpha_l < \frac{Q-m}{\sigma} < -\alpha_r, \\ \left( \frac{n_r}{|\alpha_r|} \right)^{n_r} e^{-\frac{1}{2}\alpha_r^2} & \text{for } \frac{Q-m}{\sigma} \geq -\alpha_r, \\ e^{-\frac{1}{2}\left(\frac{Q-m}{\sigma}\right)^2} & \text{else} \end{cases}$$

where  $n_{l,r}$  are the exponent indices for the low energy and high energy tails,  $\alpha_{l,r}$  are the turning points of the left and right tails. The left tail of the Double Crystal Ball functions takes into account final state radiation and interaction with matter while the right tail describes non Gaussian detector effects. The parameters  $\alpha$  and  $n$  are very strongly correlated. Therefore we chose to fix the values of the exponential indices to  $n_l = 3.5$  and  $n_r = 4.9$  for both  $\chi_{c1}$  and  $\chi_{c2}$ .

Results of the fits with Double Crystal Ball from Monte Carlo simulation for  $\chi_{c1}$  and  $\chi_{c2}$  are shown in Appendix C and the parameters extracted from the fit are summarized in Table 4.5.

The  $\chi_{c1}$  mass in Table 4.5 is about 6 MeV/c<sup>2</sup> lower than its PDG value given in Table 4.1. This is due to the incomplete recovery of bremsstrahlung radiation emitted by the two electrons.

Table 4.5: Parameters of the Double Crystal Ball function from Monte Carlo simulation for  $\chi_{c1}$  and  $\chi_{c2}$ .

$p_T(J/\psi)$	$m$ [GeV/c <sup>2</sup> ]	$\sigma$ [GeV]	$\alpha_l$	$\alpha_r$
$\chi_{c1}$				
7-9	3.50523 ± 0.00026	0.00635 ± 0.00020	0.588 ± 0.022	2.119 ± 0.093
9-11	3.50532 ± 0.00011	0.00648 ± 0.00009	0.579 ± 0.009	2.090 ± 0.069
11-13	3.50524 ± 0.00011	0.00647 ± 0.00009	0.557 ± 0.009	2.017 ± 0.054
13-16	3.50477 ± 0.00016	0.00706 ± 0.00013	0.584 ± 0.012	1.918 ± 0.045
16-20	3.50486 ± 0.00022	0.00670 ± 0.00024	0.524 ± 0.019	1.571 ± 0.060
20-25	3.50479 ± 0.00028	0.00694 ± 0.00037	0.516 ± 0.027	1.389 ± 0.078
$\chi_{c2}$				
7-9	3.55057 ± 0.00017	0.00677 ± 0.00014	0.542 ± 0.013	2.122 ± 0.088
9-11	3.55000 ± 0.00060	0.00749 ± 0.00027	0.580 ± 0.032	2.151 ± 0.055
11-13	3.55002 ± 0.00015	0.00766 ± 0.00015	0.566 ± 0.011	1.982 ± 0.060
13-16	3.54947 ± 0.00027	0.00829 ± 0.00021	0.600 ± 0.018	1.880 ± 0.042
16-20	3.5505 ± 0.0011	0.00766 ± 0.00001	0.518 ± 0.000	1.681 ± 0.002
20-25	3.5502 ± 0.0020	0.00696 ± 0.00016	0.479 ± 0.072	1.28 ± 0.14

For the  $\chi_{c0}$  state we do not use the Monte Carlo simulation to extract resolution parameters. Instead we parametrize the  $\chi_{c0}$  mass distribution with Crystal Ball function [47] with width  $\sigma$  and tail parameters  $\alpha$  and  $n$  equal to the  $\sigma$ ,  $\alpha_l$  and  $n_l$  of the  $\chi_{c1}$  Double Crystal Ball function.

The Crystal Ball function has four parameters:  $m$ ,  $\sigma$ ,  $\alpha$  and  $n$  and is defined as

$$S(Q; \alpha, n, \sigma, m) = \begin{cases} \left(\frac{n}{|\alpha|}\right)^n e^{-\frac{1}{2}\alpha^2} & \text{for } \frac{Q-m}{\sigma} \leq -\alpha, \\ \left(\frac{n}{|\alpha| - |\alpha| - \frac{Q-m}{\sigma}}\right)^n & \text{for } -\alpha < \frac{Q-m}{\sigma} < \alpha, \\ e^{-\frac{1}{2}\left(\frac{Q-m}{\sigma}\right)^2} & \text{for } \frac{Q-m}{\sigma} > \alpha. \end{cases}$$

### Probability distribution function for background

The majority of the background events which mimic  $\chi_c$  come from the combination of a  $J/\psi$  with a converted photon originating from  $\pi^0$ ,  $\pi^0 \rightarrow \gamma\gamma$ . The background distribution is modeled by a generic PDF defined as

$$S_B = (Q - q_0)^{\alpha_1} \cdot e^{(Q - q_0)\beta_1} \quad (4.12)$$

where  $\alpha_1$  and  $\beta_1$  are free parameters in the fit to data. The parameter  $q_0$  is fixed to 3.2 GeV/c

by assuming the combinatorial background starts to form at about this value.

### Results from fitting procedure to data

In Figures 4.8, 4.9 and 4.10 the fits to the measured mass difference spectrum for several  $p_T$  ranges of  $J/\psi$  are shown.

The  $\chi_{c1}$  and  $\chi_{c2}$  signals are parametrized by Double Crystal Ball function described above with parameters extracted from the Monte Carlo simulation. The  $\chi_{c0}$  distribution is parametrized with a Crystal Ball function with the same  $\sigma$ ,  $\alpha$  and  $n$  as the ones from the low-energy tail of the  $\chi_{c1}$ . The mass of the  $\chi_{c0}$  is fixed to the mass of the  $\chi_{c1}$  minus the mass difference between the two states obtained from the PDG. In the combined PDF in Equation 4.11 only the normalization factors  $N_{\chi_{c1}}$  and  $N_B$  and the background PDF parameters  $\alpha_1$  and  $\beta_1$  are free and they are determined from the fit to data.

Table 4.6 summarizes the number of reconstructed  $\chi_{c1}$  and  $\chi_{c2}$  and their ratio for different  $p_T$  ranges of  $J/\psi$  as extracted by performing an unbinned extended maximum likelihood fit to  $m_{\gamma\mu\mu} - m_{\mu\mu} + m_{J/\psi}^{PDG}$ .

Table 4.6: Results of the maximum likelihood fit with the Monte Carlo driven signal parametrization and exponential multiplied by power low background parametrization. The uncertainties are statistical only. The uncertainty on the ratio includes the correlation between  $N_{\chi_{c1}}$  and  $N_{\chi_{c2}}$ .

$p_T(J/\psi)[GeV/c]$	$N_{\chi_{c1}}$	$N_{\chi_{c2}}$	$N_{\chi_{c2}}/N_{\chi_{c1}}$
7.0-9.0	$618 \pm 31$	$315 \pm 25$	$0.510 \pm 0.049$
9.0-11.0	$1680 \pm 49$	$788 \pm 38$	$0.469 \pm 0.027$
11.0-13.0	$1820 \pm 51$	$820 \pm 38$	$0.451 \pm 0.025$
13.0-16.0	$1768 \pm 51$	$852 \pm 39$	$0.482 \pm 0.027$
16.0-20.0	$1270 \pm 43$	$487 \pm 31$	$0.383 \pm 0.028$
20.0-25.0	$643 \pm 31$	$237 \pm 22$	$0.369 \pm 0.040$

### 4.6.2 Kinematic distributions from data

To understand the nature of this measurement we plot several kinematic distributions of converted photons,  $J/\psi$  and  $\chi_c$  candidates. Figure 4.11 and Figure 4.12 show the transverse momentum  $p_T$  and pseudorapidity  $\eta$  (rapidity  $y$ ) distributions respectively for converted photons and  $J/\psi$ s coming separately from  $\chi_{c1}$  and  $\chi_{c2}$  with the selection cuts in Table 4.4. We

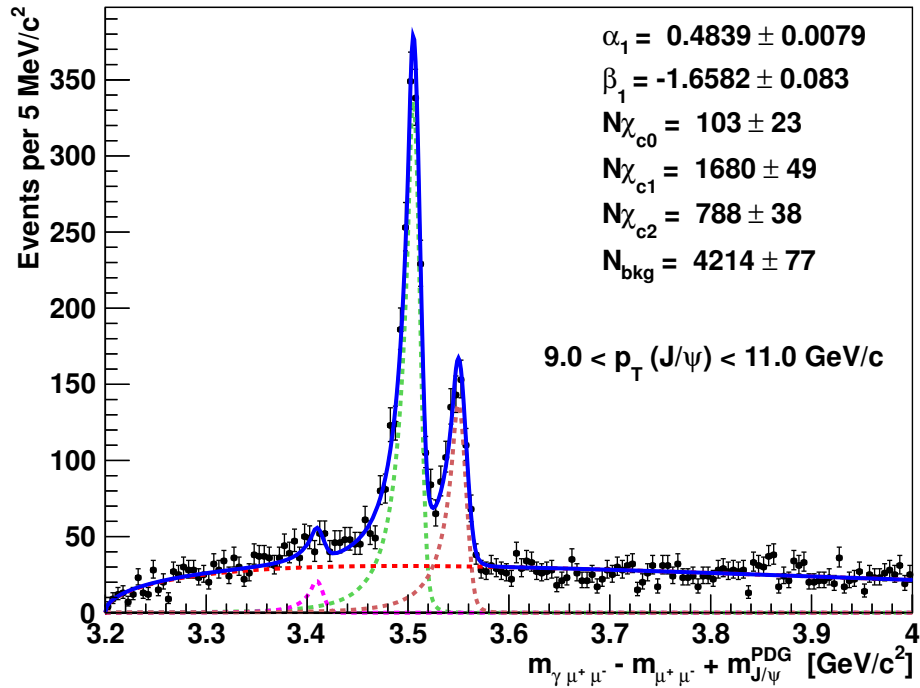
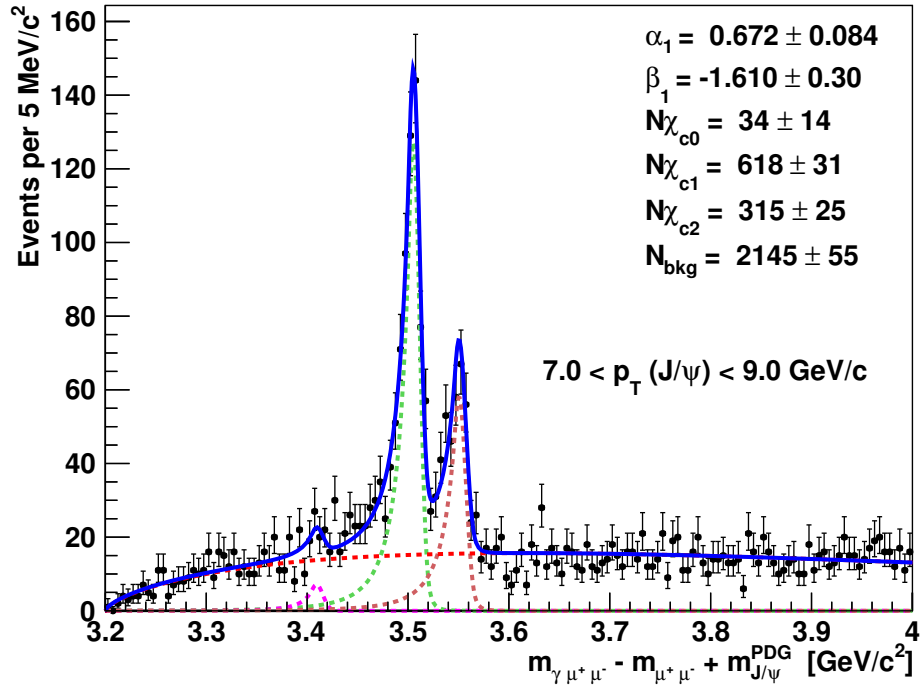


Figure 4.8: Fits to mass difference spectrum for  $\chi_c$  candidates for  $p_T(J/\psi)$  in  $[7.0-9.0]$  GeV/c with  $\chi^2/ndf = 0.77$  (top) and  $[9.0-11.0]$  GeV/c with  $\chi^2/ndf = 1.03$  (bottom).



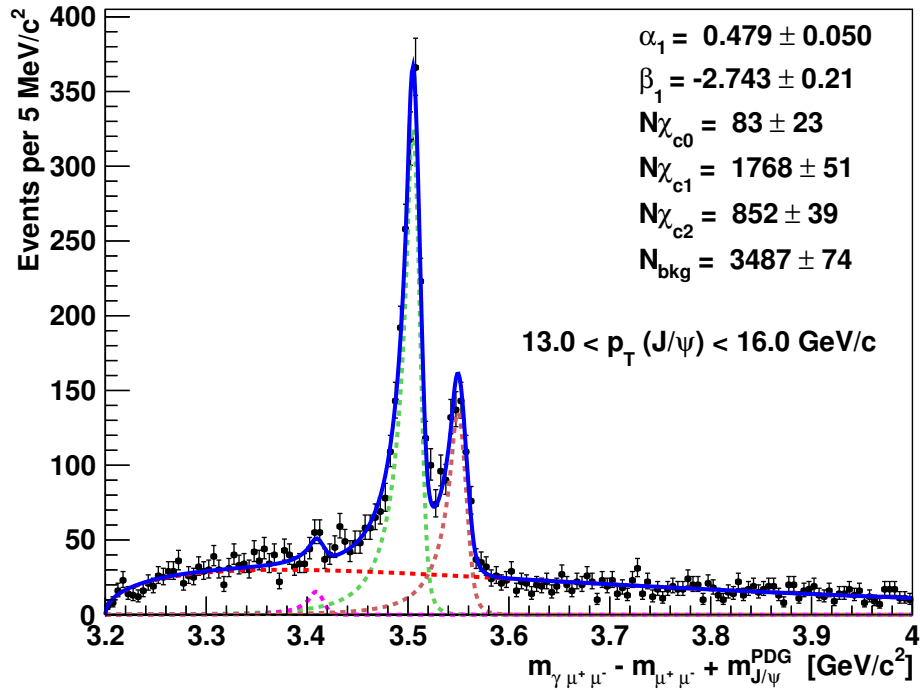
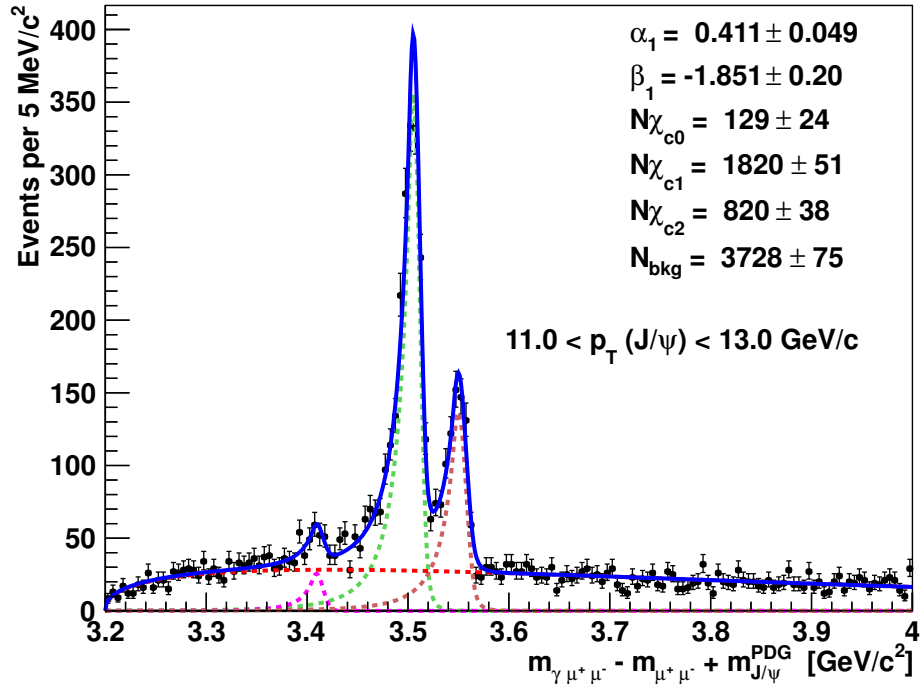


Figure 4.9: Mass difference spectrum for  $\chi_c$  candidates for  $p_T(J/\psi)$  in [11.0 – 13.0] GeV/c with  $\chi^2/ndf = 0.9$  (top) and [13.0 – 16.0] GeV/c with  $\chi^2/ndf = 0.9$  (bottom).

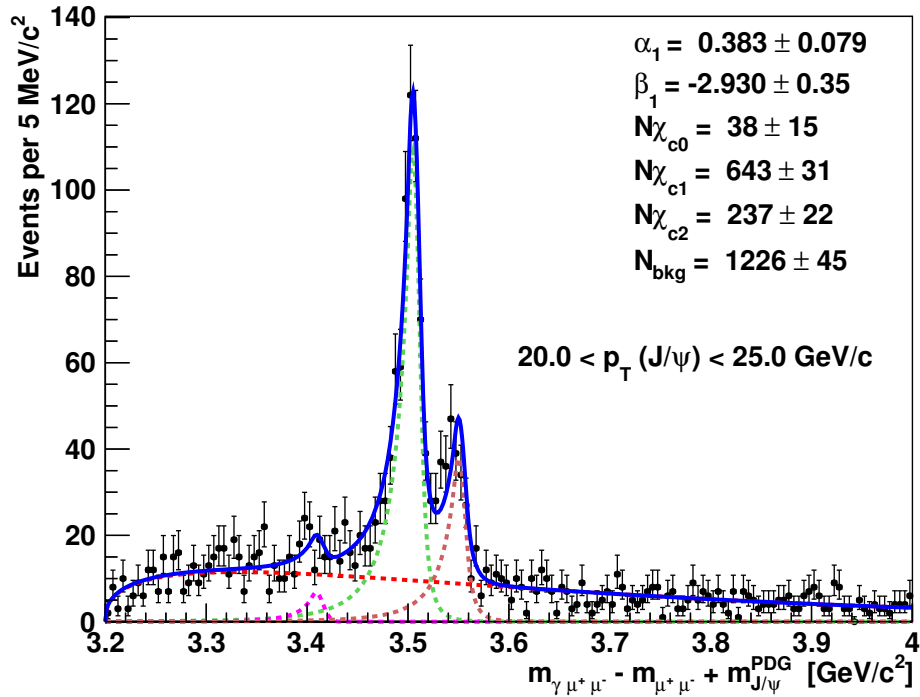
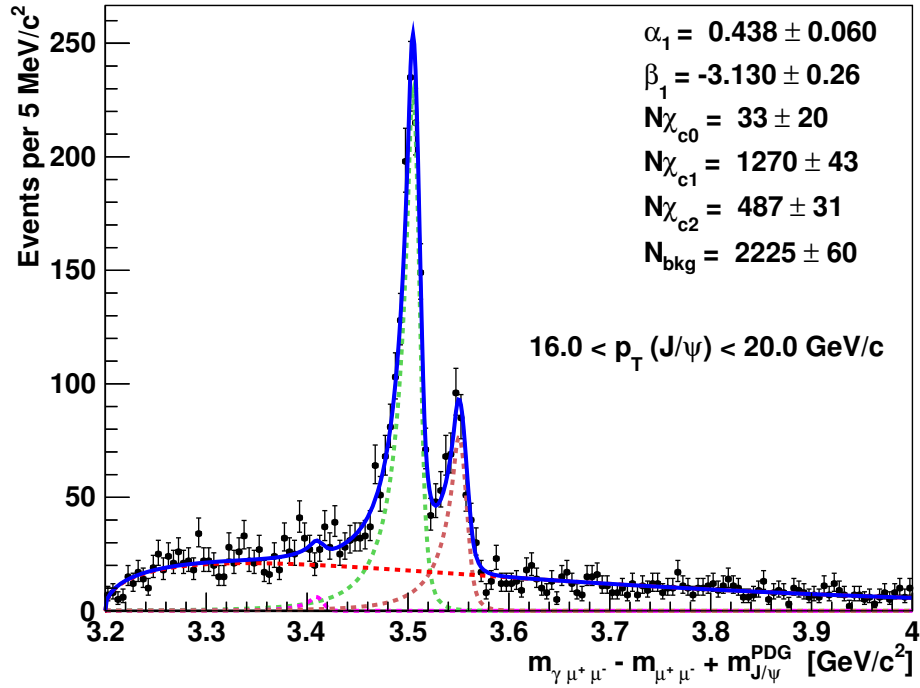


Figure 4.10: Mass difference spectrum for  $\chi_c$  candidates for  $p_T(J/\psi)$  in  $[16.0 - 20.0]$  GeV/c with  $\chi^2/ndf = 0.86$  (top) and  $[20.0 - 25.0]$  GeV/c with  $\chi^2/ndf = 0.81$  (bottom).

discriminate the  $\chi_{c1}$  from the  $\chi_{c2}$  by assuming that the  $\chi_{c1}$  candidates have an invariant mass in the region 3.45 and 3.52  $\text{GeV}/c^2$ , while the  $\chi_{c2}$  candidates have invariant mass in the region 3.52 and 3.57  $\text{GeV}/c^2$ . The presence of background events and cross contamination is not taken into account. The number of  $\chi_c$  candidates is also not corrected for the efficiency and acceptance of the two states.

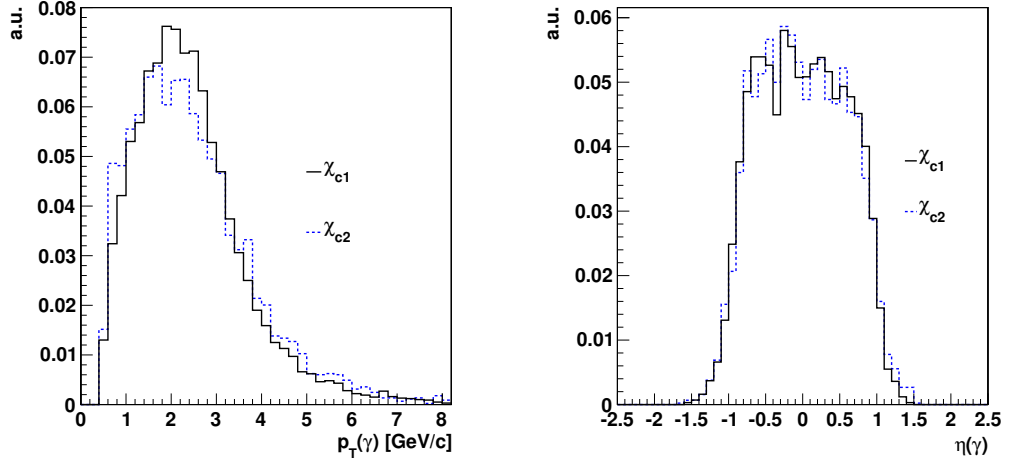


Figure 4.11: Transverse momentum (left) and pseudorapidity (right) distributions of converted photons from  $\chi_{c1}$  (black) and  $\chi_{c2}$  (blue) in data with cuts from Table 4.4. The pseudorapidity of the photon is in the range  $[-1.1, 1.1]$  therefore the photon does not fly very far from the  $J/\psi$ , see Figure 4.12.

With this crude assumption, we observe that the  $p_T$  spectrum of  $\gamma$  and  $J/\psi$  from  $\chi_{c1}$  and  $\chi_{c2}$  are very similar for both states. The corresponding rapidity distributions are also very similar and almost uniformly distributed in the range  $[-1, 1]$ .

Figure 4.13 shows the transverse momentum  $p_T$  and rapidity  $y$  distributions of  $\chi_{c1}$  and  $\chi_{c2}$ . The  $p_T$  distribution of  $\chi_{c2}$  is harder with respect to the  $p_T$  distribution of  $\chi_{c1}$ . Rapidity distributions for both  $\chi_{c1}$  and  $\chi_{c2}$  are almost flat.

The azimuthal distributions,  $\phi$ , for converted photons,  $J/\psi$  and  $\chi_c$  are not plotted because they are found to be symmetrical.

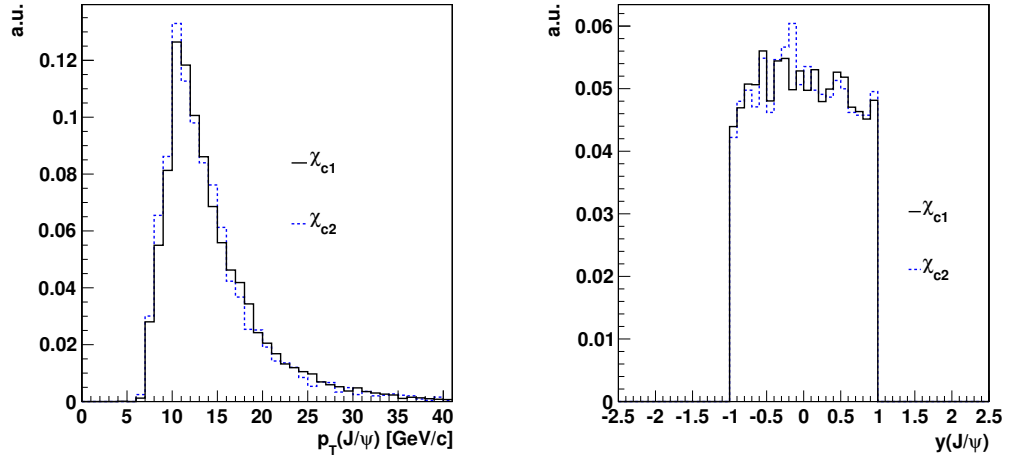


Figure 4.12: Transverse momentum (left) and rapidity (right) distributions of  $J/\psi$  from  $\chi_{c1}$  (black) and  $\chi_{c2}$  (blue) in data with cuts from Table 4.4. The cut on the rapidity of the  $J/\psi$  in  $[-1, 1]$  is clearly visible.

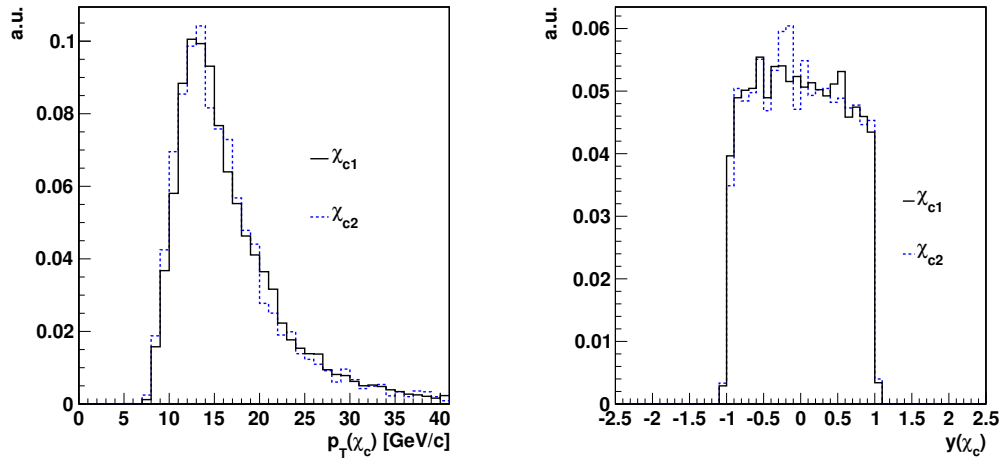


Figure 4.13: Transverse momentum (left) and rapidity (right) distributions of  $\chi_{c1}$  (black) and  $\chi_{c2}$  (blue) in data data with cuts from Table 4.4.

## 4.7 Acceptance and efficiency studies with Monte Carlo

### 4.7.1 Measurement of the ratio of efficiencies $\epsilon_1/\epsilon_2$

#### Pythia Monte Carlo particle gun

To determine the ratio  $\epsilon_1/\epsilon_2$  in Equations 4.7 and 4.8, a Monte Carlo simulation sample of equal numbers of  $\chi_{c1}$  and  $\chi_{c2}$  is used. The ratio  $\epsilon_1/\epsilon_2$  consists of the detector acceptance ratio multiplied with the reconstruction efficiency ratio for  $\chi_{c1}$  and  $\chi_{c2}$ . Detector acceptance is defined as the probability to find the decay products of  $\chi_{c1}$  and  $\chi_{c2}$  within the fiducial region of the CMS detector. This probability is less than one because certain events with generated  $\chi_c$  can be lost due to an imperfect detector. Reconstruction efficiency gives the probability to reconstruct  $\chi_c$  with respect to the total number of  $\chi_c$  in the given fiducial region of the detector.

The coefficient  $\epsilon_1/\epsilon_2$  is a correction factor to the ratio of observed events and it gives the correct ratio of expected events with  $\chi_{c1}$  and  $\chi_{c2}$ .

The Monte Carlo sample is produced using Pythia particle gun [49] which is a generator that generates only one type of particle. In our case this particle is  $\chi_{c1}$  or  $\chi_{c2}$ . Additionally, we configure the particle gun such that the  $\chi_{c1}$  and  $\chi_{c2}$  are generated in the rapidity range  $|y| < 1.25$  and in the  $p_T$  range between 0 GeV/c and 40 GeV/c with the same  $p_T$  spectrum as the one observed by the CMS experiment for the  $\psi'$  in the range between 5 GeV/c and 40 GeV/c. See below for more details on the generated input  $p_T(\chi_c)$  spectrum.

#### Input $p_T(\chi_c)$ spectrum

We do not know the momentum spectra of the  $\chi_{c1}$  and  $\chi_{c2}$  mesons. For the Monte Carlo generation of the  $\chi_c$ , a reasonable assumption is the choice of the  $p_T(\psi')$  spectrum. This choice is motivated by the proximity of the  $\psi'$  mass with the  $\chi_{c1}$  and  $\chi_{c2}$  masses ( $m_{\psi'} = 3.686$  GeV/c<sup>2</sup>). Additionally, there exist a measurement of the  $p_T(\psi')$  spectrum [45] with CMS detector in various rapidity ranges including the observed rapidity range of  $\chi_c$  states.

We use the data available in [45] for the  $\psi'$  momentum spectrum in the range  $|y(\psi')| < 1.2$  (observed  $|y_{\chi_{c1,c2}}| < 1.1$ , see Figure 4.13) and parametrize the data using the expression

$$\frac{dN}{dp_T} \propto p_T \left[ 1 + \frac{1}{(\beta-2)} \frac{p_T^2}{\langle p_T^2 \rangle} \right]^{-\beta} \quad (4.13)$$

where  $\beta$  and  $\langle p_T^2 \rangle$  are free parameters in the fit and their values are found to be  $\beta = 3.71 \pm 0.27$ ,  $\langle p_T^2 \rangle = 19.5 \pm 5.8$ .

The fitted  $p_T(\psi')$  spectrum used to model the  $p_T(\chi_c)$  spectrum is shown in Figure 4.14. Once generated with Pythia Monte Carlo particle gun generator, the  $\chi_c$  states are forced to decay to  $J/\psi + \gamma$ .

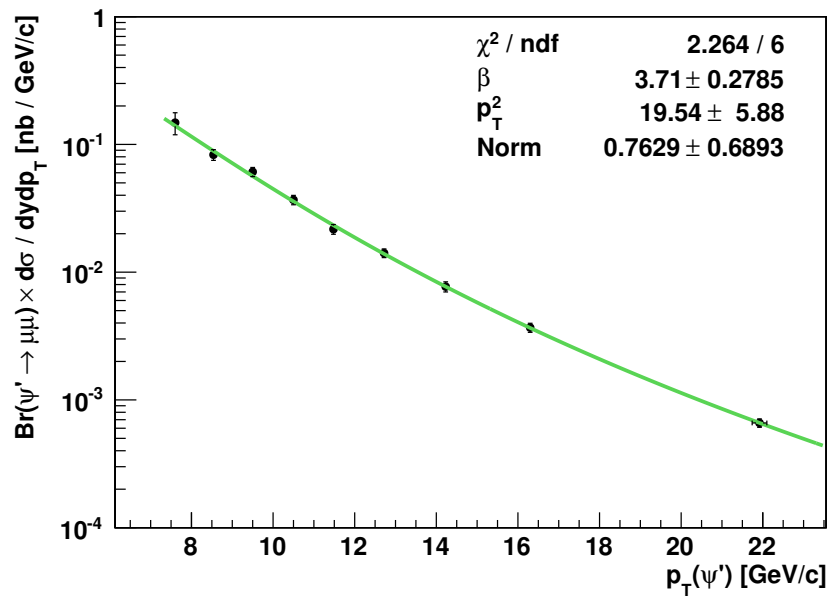


Figure 4.14: The  $p_T$  spectrum measured in [45] is shown with data points. The green line is the fitted spectrum with Equation 4.13 used as input distribution for the Pythia Monte Carlo particle gun.

### Decay angular distributions

Before proceeding with the next step towards the evaluation of the efficiency ratio  $\epsilon_1/\epsilon_2$  lets look at the angular distributions of the  $\chi_c$  decay products . The angles between various particles in the process  $\chi_c \rightarrow J/\psi + \gamma$  are indicated in Figure 4.15 where  $\theta'$  and  $\phi'$  are the polar and azimuthal angles between positive muon as measured in the  $J/\psi$  rest frame and the direction of the  $J/\psi$  as seen in the  $\chi_c$  rest frame. The polar angle  $\theta$  is between  $J/\psi$  in the  $\chi_c$  rest frame and  $\chi_c$  direction in the laboratory. The angles  $\theta'$  and  $\phi'$  contain information on the polariza-

tion of the  $J/\psi$ , while  $\theta$  contains information on the polarization of the  $\chi_c$ . The polarization measures the degree to which the total angular momentum of a given particle is aligned with respect to a chosen axis.

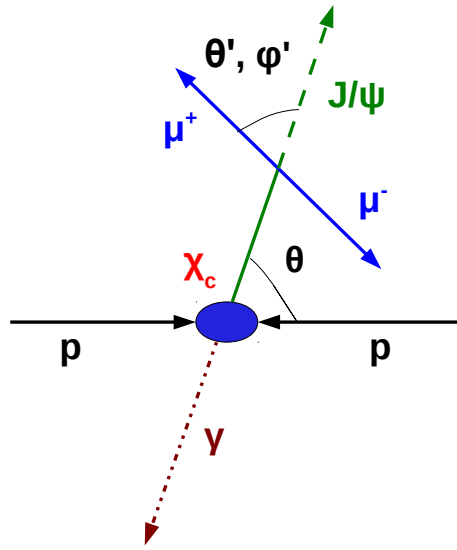


Figure 4.15: Production of  $\chi_c$  in proton-proton collisions and its decay to  $J/\psi + \gamma$ . The polar and azimuthal angles,  $\theta'$  and  $\phi'$ , are between the positive muon as measured in the  $J/\psi$  rest frame and the direction of the  $J/\psi$  as seen in the  $\chi_c$  rest frame. Polar angle  $\theta$  is between  $J/\psi$  in the  $\chi_c$  rest frame and  $\chi_c$  direction in the laboratory.

The Pythia Monte Carlo particle gun generates isotropic distributions for both the photon from the  $\chi_c$  and the muons from the  $J/\psi$ . This is equivalent to say that the angular distributions  $\theta$ ,  $\theta'$  and  $\phi'$  are isotropic. Isotropic values of  $\theta$  mean unpolarized  $\chi_c$  mesons, while isotropic values of  $\theta'$  and  $\phi'$  mean that the angular momentum in the  $J/\psi$  rest frame is not conserved. In general, the polar angle distribution,  $W(\theta')$ , of the positive muon in the  $J/\psi$  rest frame, independently of the  $J/\psi$  production mechanism, to first approximation is [52]

$$W(\theta') = 1 - \lambda_{\theta'} \cos^2 \theta'. \quad (4.14)$$

where  $\lambda_{\theta'} = 0$  means absence of polarization,  $\lambda_{\theta'} = -1$  means complete longitudinal polarization and  $\lambda_{\theta'} = 1$  means complete transverse polarization of the  $J/\psi$ . The  $J/\psi$  has total angular momentum  $J = 1$  therefore there are three possible values for the third component of the angular momentum,  $J_z = 0, \pm 1$ . An unpolarized  $J/\psi$  has the same probability,  $1/3$ , to be found in each of the angular momentum eigenstates,  $J_z = -1, 0, 1$ . A transversely polarized  $J/\psi$  has angular momentum component  $J_z = \pm 1$  and a longitudinally polarized  $J/\psi$  has angular momentum component  $J_z = 0$ .

In radiative decays,  $\chi_c \rightarrow J/\psi + \gamma$ , it has been shown in [53, 54, 55] that the polar angle distribution,  $W(\theta')$ , of the positive muon in the  $J/\psi$  rest frame with respect to the  $J/\psi$  direction as seen from the  $\chi_c$  rest frame to first order approximation has always the form

$$\begin{aligned} W(\theta') &= 1 - 1/3 \cos^2 \theta' \quad \text{for } \chi_{c1} \\ W(\theta') &= 1 + 1/3 \cos^2 \theta' \quad \text{for } \chi_{c2} \end{aligned} \quad (4.15)$$

independently of the polarization of  $\chi_{c1}$  and  $\chi_{c2}$ . The angular distributions in Equations 4.15 are the integrated over  $\theta$  and  $\phi'$  full decay angular distributions of  $\chi_{c1}$  and  $\chi_{c2}$  which will be introduced in Section 4.9.4 and Appendix F. We apply a reweighting procedure to the generated with the Monte Carlo particle gun  $\chi_c$  mesons, to obtain the predicted and physically correct decay angular distribution for the  $J/\psi$  shown in Equations 4.15.

Figures 4.16 and 4.17 illustrate  $\cos \theta'$  distribution respectively for  $\chi_{c1}$  and  $\chi_{c2}$  before and after reweighting. We do not reweight the angular distribution  $\theta$  and assume that  $\chi_{c1}$  and  $\chi_{c2}$  are produced unpolarized ( $\theta$  distribution is isotropic) as the correct polarization is not known. In Section 4.9.4 we will apply reweighting procedure and produce  $\chi_{c1}$  and  $\chi_{c2}$  in various polarization states. We will assign a systematic uncertainty on the cross section ratio due to the assumption of producing unpolarized  $\chi_c$  states.

We have the decay products of  $\chi_{c1}$  and  $\chi_{c2}$  generated with Pythia Monte Carlo particle gun with properly reweighted angular distributions and we are now ready to continue with the next steps for the calculation of the efficiency ratio.



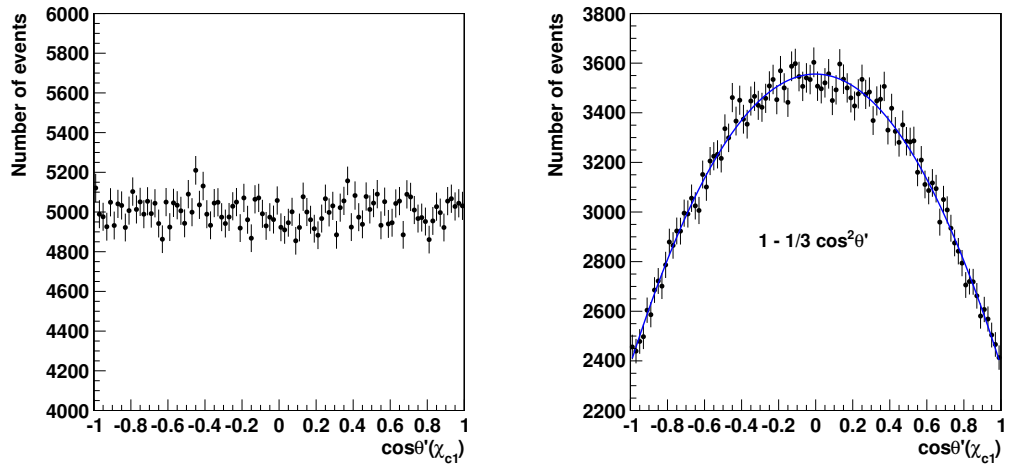


Figure 4.16: Polar angle of the muon in the  $J/\psi$  rest frame with respect to the  $J/\psi$  direction as seen from the  $\chi_{c1}$  rest frame. Left: before reweighting, right: after reweighting.

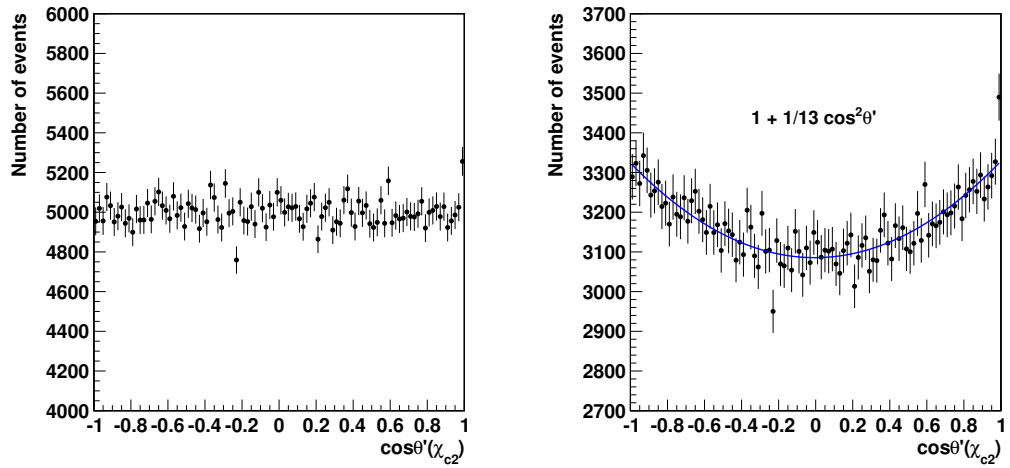


Figure 4.17: Polar angle of the muon in the  $J/\psi$  rest frame with respect to the  $J/\psi$  direction as seen from the  $\chi_{c2}$  rest frame. Left: before reweighting, right: after reweighting.

## Detector simulation, reconstruction and selection-1

At this step the decay products of  $\chi_{c1}$  and  $\chi_{c2}$  are processed through the full CMS detector simulation using CMS software (CMSSW) which is based on the program GEANT4 [50, 51]. The GEANT4 is a software package used to simulate the passage of particles through matter.

The simulation processes included in the GEANT4 toolkit are information of size, shape, material type and position of detector elements, generation of events, tracking through matter, response of detector components etc. The simulation uses output of the Monte Carlo generator which is in the form of particle four vectors and simulates the interaction of these particles within the detector volume. The interactions can be separated in several categories: energy loss by particle ionization and multiple scattering in tracker, particle decays, electromagnetic, hadronic interactions etc. The result of the interactions are physical signals in the sensitive detector element which are transformed into a digital signal with the help of electronics. This step of simulation is also called digitization and the digitized data is called raw data. The raw data from simulation has the same format as real raw data from collisions.

The simulated raw data is then processed through standard CMSSW reconstruction algorithms, trigger selection (Table 4.3),  $\chi_c$  reconstruction and  $\chi_c$  selection (Table 4.4) as real data.

### Low $p_T$ tracks

At this point, we simulated only tracks originating from  $\chi_c$  particles,  $\mu^+$ ,  $\mu^-$  and  $\gamma$  tracks. To be able to correctly determine the ratio  $\epsilon_1/\epsilon_2$ , we add to the simulated digitized signals of the muon and the photon tracks produced with the step above additional digitized signals from low  $p_T$  tracks from the underlying event and pileup.

All particles that emerge from a single parton collision except the process of interest is called underlying event. Pileup is a result of multiple interactions caused by the existence of many parton collisions per bunch crossing. These interactions are with low momentum transfer and they are most common in proton-proton collisions. As a result there can be several primary vertices in one event which can make the reconstruction of a given decay process difficult. On the other hand the probability of that process to occur in collisions becomes higher. Underlying event and pileup interactions give origin to large number low momentum tracks.

By adding tracks from the underlying event and pileup we achieve a more realistic way to determine the ratio of efficiencies. This is because the reconstruction efficiency of converted photons is very much influenced by the presence of low  $p_T$  tracks in the tracker. The pattern recognition algorithm that is at the base of the tracking building process is less efficient when the number of hits in the CMS tracker increases, especially for low  $p_T$  tracks.

We use the standard CMSSW mixing procedure [56] which adds tracks from the underlying events and pileup to our muon, electron and positron tracks as simulated with CMSSW. The mixing scheme which we used is *mix.E7TeV\_AVE.5\_BX156* and it was chosen because it was found to best match the observed distribution of the number of reconstructed primary vertices with the reconstructed primary vertices in Run2011A and Run2011B.

### **Detector simulation, reconstruction and selection-2**

At this step, the simulated digitized decay products of  $\chi_{c1}$  and  $\chi_{c2}$  are mixed with digitized signals of low  $p_T$  tracks from underlying event and pileup. They are both processed again through reconstruction with CMSSW software,  $\chi_c$  reconstruction and selection (Table 4.3 and Table 4.4) procedures. The final event sample is used to measure the acceptance and efficiency correction factor.

### **Efficiency ratio**

The ratio of efficiencies  $\epsilon_1/\epsilon_2$  for different bins of  $p_T(J/\psi)$ , is obtained as

$$\frac{\epsilon_1}{\epsilon_2} = \frac{N_{\chi_{c1}}^{rec} / N_{\chi_{c1}}^{gen}}{N_{\chi_{c2}}^{rec} / N_{\chi_{c2}}^{gen}} \quad (4.16)$$

where  $N_{\chi_{c1}}^{rec}$  and  $N_{\chi_{c2}}^{rec}$  are the number of  $\chi_{c1}$  and  $\chi_{c2}$  candidates generated with Pythia Monte Carlo particle gun and subsequently reconstructed with the CMS detector as explained above with the selection cuts in Table 4.4. The numbers  $N_{\chi_{c1}}^{gen}$  and  $N_{\chi_{c2}}^{gen}$  represent the number of  $\chi_{c1}$  and  $\chi_{c2}$  candidates generated with Pythia Monte Carlo particle gun as explained above in the kinematic range  $|y_{J/\psi}| < 1.0$  and  $p_T(\gamma) > 0.5$  GeV/c. The resulting values are shown in Table 4.7, where the uncertainty is due to the limited size of the simulation sample and it is assumed to be binomial.

The values of  $\epsilon_1/\epsilon_2$  in Table 4.7 are almost constant for different  $p_T(J/\psi)$  but they differ from one. Hence, there is a difference between  $\epsilon_1$  and  $\epsilon_2$  or equivalently to say a difference

Table 4.7: The values of  $\epsilon_1/\epsilon_2$  obtained from Pythia Monte Carlo particle gun. The uncertainties on  $\epsilon_1$  and  $\epsilon_2$  are statistical and they are assumed to be binomial.

$p_T^{J/\psi}$ [GeV/c]	$\epsilon_1/\epsilon_2$
7.0-9.0	0.903 $\pm$ 0.023
9.0-11.0	0.935 $\pm$ 0.019
11.0-13.0	0.945 $\pm$ 0.021
13.0-16.0	0.917 $\pm$ 0.022
16.0-20.0	0.981 $\pm$ 0.031
20.0-25.0	1.028 $\pm$ 0.049

between the geometric acceptance and reconstruction efficiency of  $\chi_{c1}$  and  $\chi_{c2}$ . The difference can be influenced by the different  $p_T$  spectrum for the muon pair originating from the  $J/\psi$  or the different  $p_T$  spectrum of the emitted photon. In Chapter 4.7.2 we present the transverse momentum distributions of  $\chi_c$  decay products and in Chapter 4.7.3 we measure the absolute reconstruction efficiency of the  $\chi_c$  photons. The combination of them leads to the origin of the difference between the efficiencies  $\epsilon_1$  and  $\epsilon_2$ .

## 4.7.2 Kinematic distributions from Monte Carlo

### Kinematics of $\chi_c$ with $p_T(\psi')$ input spectrum

Figures 4.18 and 4.19 show transverse momentum distributions of converted photons and the  $J/\psi$  for  $\chi_{c1}$  and  $\chi_{c2}$  generated with Pythia Monte Carlo particle gun and reconstructed with the CMS detector with selection cuts in Table 4.4. Figure 4.20 shows the same distribution for the  $\chi_{c1}$  and  $\chi_{c2}$  candidates.

The plots lead to the conclusion that the transverse momentum spectrum of  $\chi_{c2}$  photon is harder with respect to the  $\chi_{c1}$  photon and the transverse momentum distributions of  $J/\psi$  from  $\chi_{c1}$  and  $\chi_{c2}$  are very similar both at the generation and reconstruction level. The transverse momentum spectra of generated  $\chi_c$  in Figure 4.20 are almost identical as expected because both of them were generated with identical input  $p_T(\psi')$  spectrum. To quantify the difference between photon and  $J/\psi$  momentum spectra for both states we make another "invalid" assumption for  $\chi_c$  input  $p_T$  spectrum. This is discussed below.

### Kinematics of $\chi_c$ with flat $p_T$ input spectrum

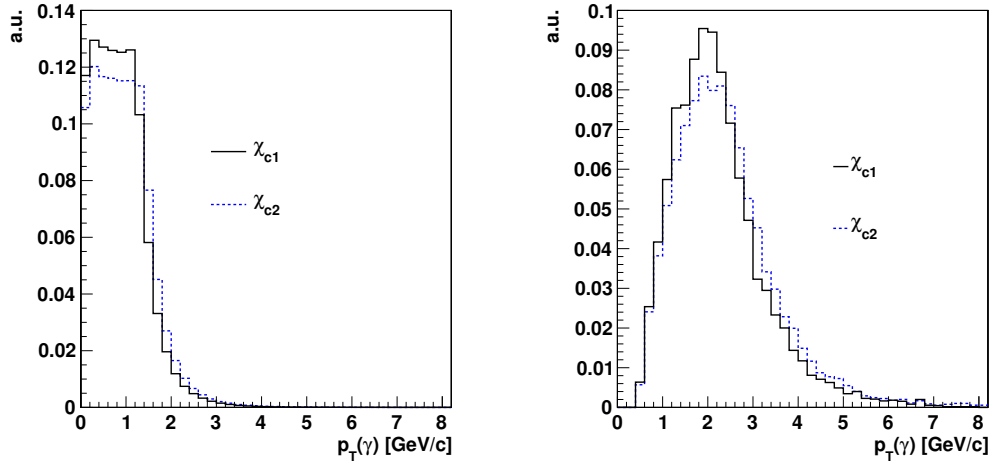


Figure 4.18:  $p_T$  distributions for the converted photons coming from  $\chi_{c1}$  and  $\chi_{c2}$  as generated with Pythia Monte Carlo particle gun with  $p_T(\psi')$  input spectrum for  $\chi_c$  (left) and reconstructed with CMS detector with applied cuts in Table 4.4 (right).

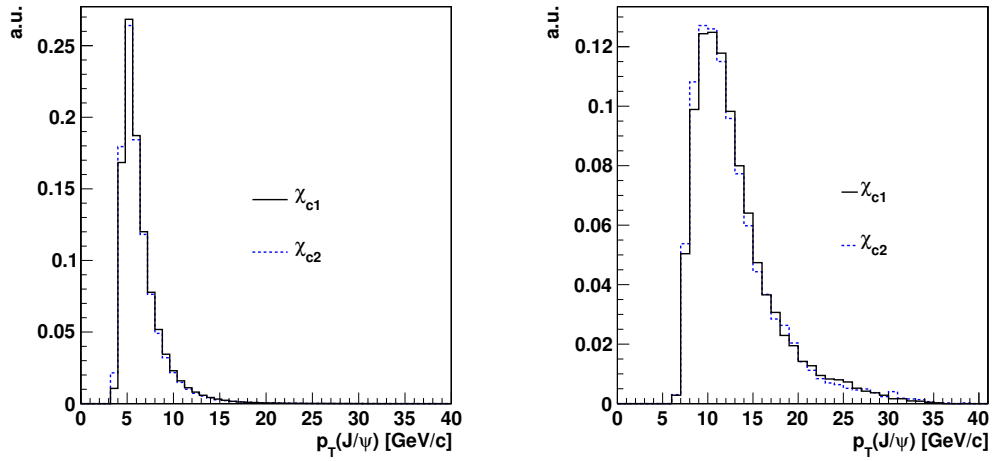


Figure 4.19:  $p_T$  distributions for the  $J/\psi$  coming from  $\chi_{c1}$  and  $\chi_{c2}$  as generated with Pythia Monte Carlo particle gun with  $p_T(\psi')$  input spectrum for  $\chi_c$  (left) and reconstructed with CMS detector with applied cuts in Table 4.4 (right).

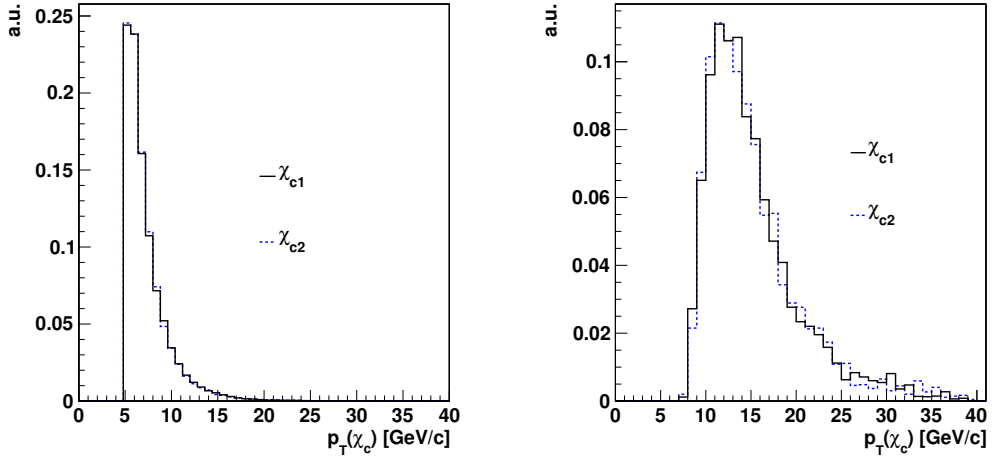


Figure 4.20:  $p_T$  distributions for  $\chi_{c1}$  and  $\chi_{c2}$  as generated with Pythia Monte Carlo particle gun with  $p_T(\psi')$  input spectrum for  $\chi_c$  (left) and reconstructed with CMS detector with applied cuts in Table 4.4 (right).

The  $\chi_{c1}$  and  $\chi_{c2}$  are generated with a  $p_T$  spectrum which populates all bins equally (flat  $p_T$  spectrum). The assumption of a flat  $p_T$  input spectrum for  $\chi_c$  is useful because it gives the possibility to study relations between other kinematic variables of  $\chi_{c1}$  and  $\chi_{c2}$ . This assumption later will be used to calculate systematics from unknown  $\chi_c$  momentum spectrum.

We plot  $p_T(\chi_c)$  vs  $p_T(J/\psi)$  and  $p_T(J/\psi)$  vs  $p_T(\gamma)$  on Figure 4.21 and Figure 4.22 for  $\chi_{c1}$  and  $\chi_{c2}$ . In Figure 4.21, the slope of the mean distribution is  $0.875 \pm 0.001$  for the  $\chi_{c1}$  and  $0.879 \pm 0.001$  for the  $\chi_{c2}$ , showing that the  $J/\psi$  takes most of the transverse momentum of the  $\chi_c$ , with a very small difference between the two states. In Figure 4.22, the slope of the mean distribution is  $0.128 \pm 0.001$  and  $0.142 \pm 0.001$  respectively, showing that photons from the  $\chi_{c2}$  have on average a 10% higher  $p_T$  with respect to photons from  $\chi_{c1}$ .

### 4.7.3 Absolute $\chi_c$ photon reconstruction efficiency

To have a quantitative understanding of the acceptance and reconstruction efficiency of  $\chi_c$  we evaluate

$$\epsilon(\chi_c) = \frac{N_{\chi_c}^{rec}}{N_{\chi_c}^{gen}}(p_T(\gamma)) \quad (4.17)$$

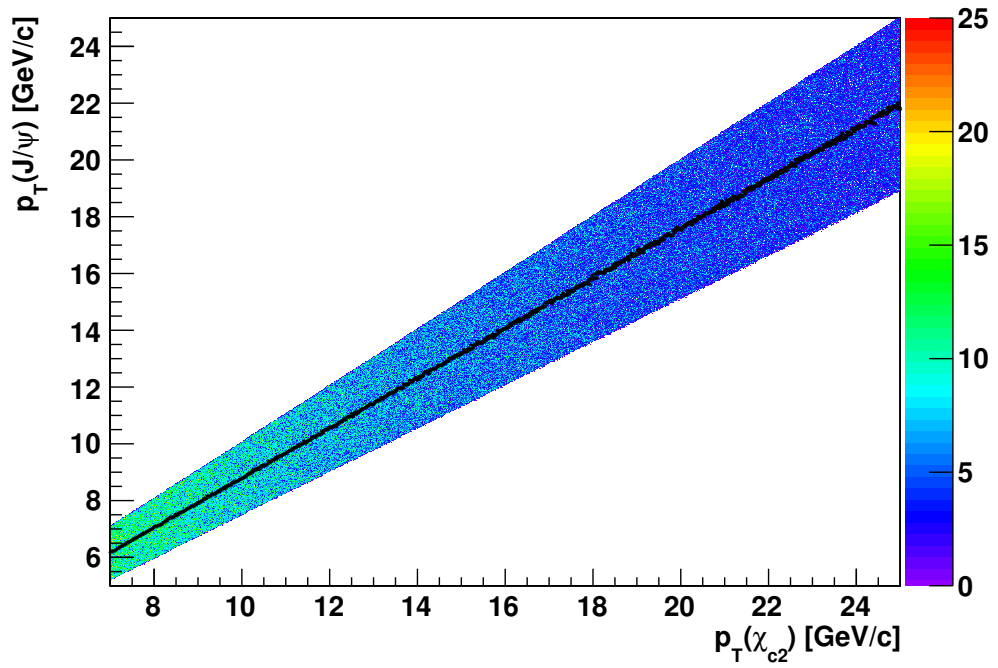
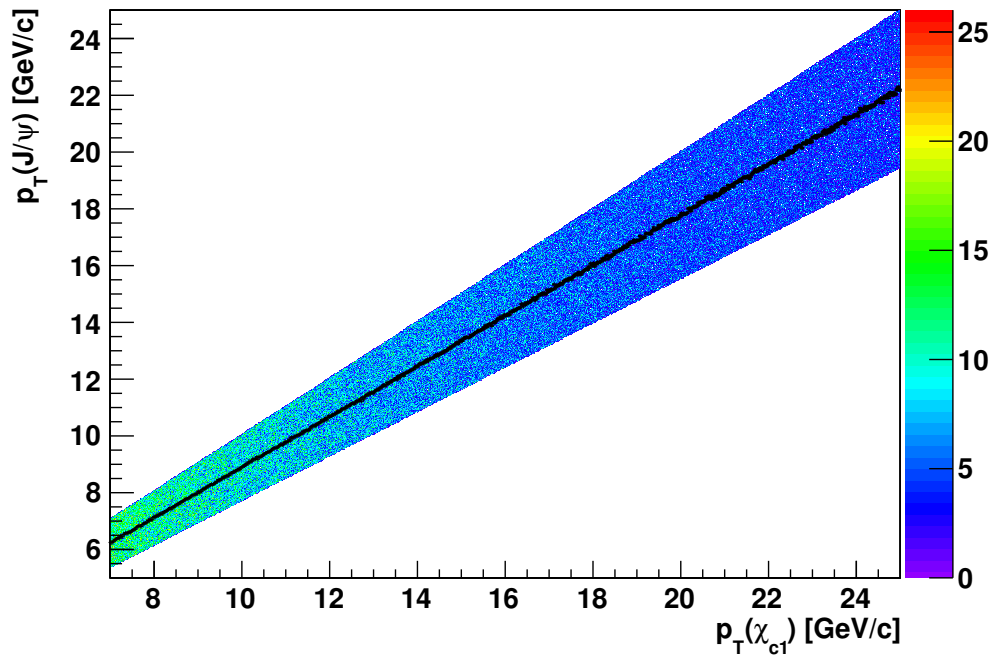


Figure 4.21:  $p_T(J/\psi)$  vs  $p_T(\chi_c)$  with mean distributions superimposed for  $\chi_{c1}$  (top) and  $\chi_{c2}$  (bottom) generated with Pythia Monte Carlo particle gun with flat  $p_T$  input spectrum for  $\chi_c$ . The slopes of the mean distributions are 0.875 and 0.879 respectively.

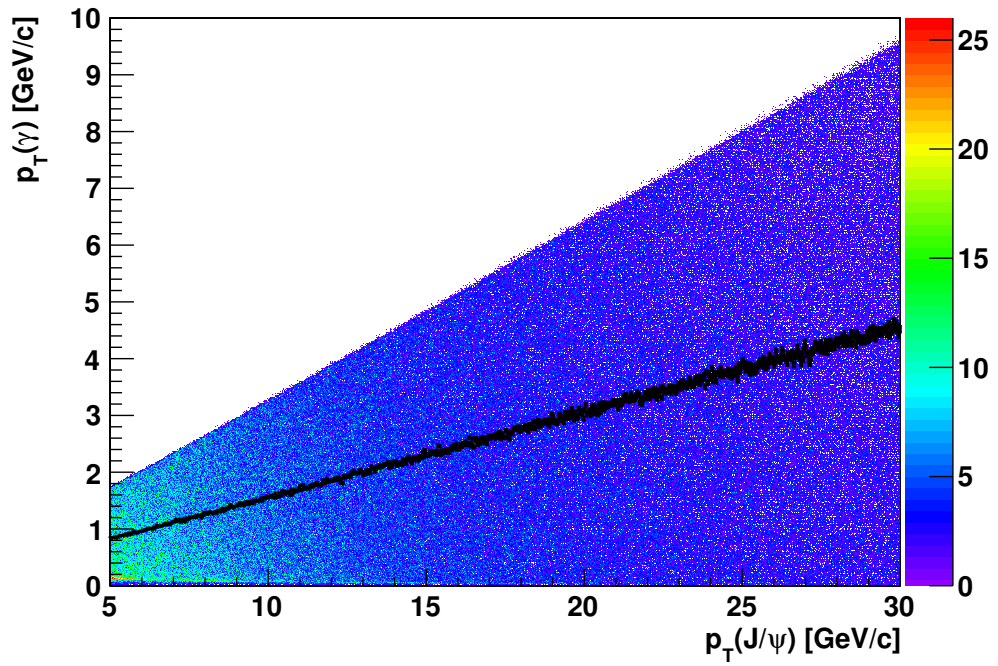
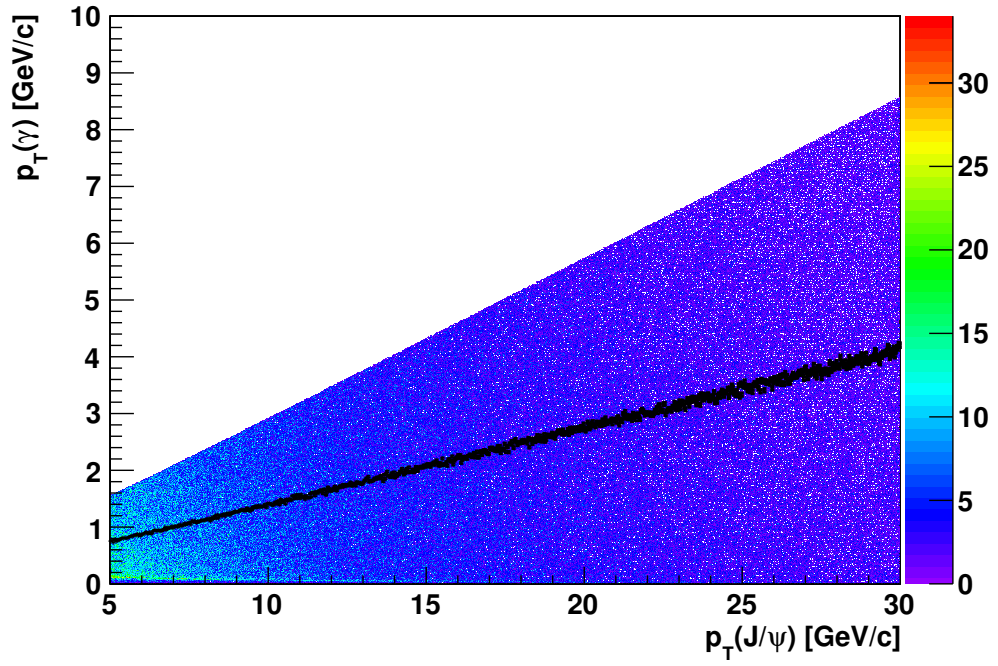


Figure 4.22:  $p_T(\gamma)$  vs  $p_T(J/\psi)$  with mean distributions superimposed for  $\chi_{c1}$  (top) and  $\chi_{c2}$  (bottom) generated with Pythia MC particle gun with flat  $p_T$  input spectrum for  $\chi_c$ . The slopes of the mean distributions are 0.128 and 0.142 respectively.



as a function of  $p_T(\gamma)$ , where  $N_{\chi_c}^{rec}$  is the number of  $\chi_{c1}$  and  $\chi_{c2}$  candidates generated with Pythia Monte Carlo particle gun and subsequently reconstructed with the CMS detector with the selections in Table 4.4 and  $N_{\chi_c}^{gen}$  is the number of generated  $\chi_{c1}$  and  $\chi_{c2}$  with Pythia Monte Carlo particle gun in the kinematic range  $|y_{J/\psi}| < 1.0$  and  $p_\gamma > 0.5$  GeV/c. The efficiency  $\epsilon(\chi_c)$  is proportional to

$$\epsilon(\chi_c) \propto \rho_{conv}^\gamma \times \epsilon_{reco}^\gamma \times \epsilon_{sel}^{\chi_c} \quad (4.18)$$

where  $\rho_{conv}^\gamma$  is the probability for a photon to convert in the tracker,  $\epsilon_{reco}^\gamma$  is the photon conversion reconstruction efficiency and  $\epsilon_{sel}^{\chi_c}$  is the  $\chi_c$  selection efficiency. The conversion probability of a photon is

$$\rho_{conv}^\gamma \propto \frac{1}{\lambda^\gamma} \propto \frac{P}{X_0} \quad (4.19)$$

where  $\lambda^\gamma$  is the mean free path of the photon to convert into an  $e^+e^-$  pair in the tracker. The factor  $\frac{P}{X_0}$  is the average conversion probability where  $P \sim 7/9$  [57] and  $X_0$  is the radiation length (thickness of material where an electron reduces its energy by a factor of  $1/e$  emitting bremsstrahlung radiation). The value of  $X_0$  varies with pseudorapidity,  $\eta$ , and azimuthal angle,  $\phi$ , in the tracker depending on the material distribution as explained in Chapter 3. On average, about 70% of all the photons convert into an  $e^+e^-$  pair in the tracker.

The convolution of the conversion probability, the reconstruction and the selection efficiency,  $\rho_{conv}^\gamma \times \epsilon_{reco}^\gamma \times \epsilon_{sel}^{\chi_c}$ , is shown in Figure 4.23 as a function of  $p_T$  of the photon in the pseudorapidity range  $|\eta(\gamma)| < 1$ .

Figure 4.23 is very important because it shows the very small probability of the  $\chi_c$  photon to convert and its very small reconstruction efficiency. Most of the  $\chi_c$  photons are in the range 0.5 – 5.0 GeV/c (Figures 4.11 and 4.18). The slope of the efficiency curve between 0.5 – 5.0 GeV/c is very steep which leads to a large variation in the reconstruction of  $\chi_c$  photons in that region. This combined with the different momentum spectra for  $\chi_{c1}$  and  $\chi_{c2}$  photons leads to their different acceptance with CMS detector (the value of  $\epsilon_1/\epsilon_2$  is different from one, see Table 4.7).

In Chapter 4.8, we will show that our measurement of  $\epsilon_1/\epsilon_2$  is stable and not affected by a

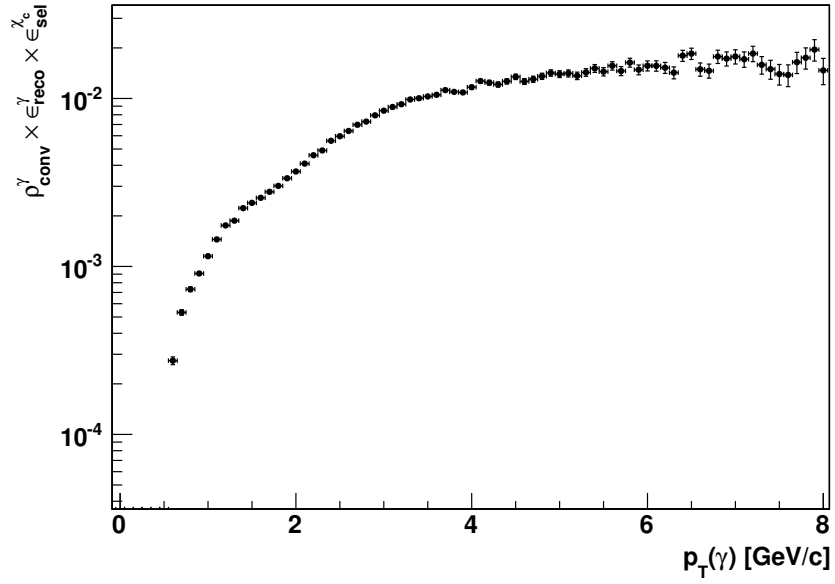


Figure 4.23: Conversion probability and reconstruction efficiency of  $\chi_c$  photons as a function of photon transverse momentum measured with Pythia Monte Carlo particle gun in  $|\eta(\gamma)| < 1$ .

possible error in the estimation of the efficiency curve in Figure 4.23 with our Monte Carlo.

Since the value of the radiation length,  $X_0$ , varies with pseudorapidity which affects the conversion probability, we studied the dependence of  $\rho_{conv}^\gamma \times \epsilon_{reco}^\gamma \times \epsilon_{sel}^{\chi_c}$  as a function of the pseudorapidity of the photon in the ranges  $[-1.0, -0.6]$ ,  $[-0.6, -0.2]$ ,  $[-0.2, 0.2]$ ,  $[0.2, 0.6]$ ,  $[0.6, 1.0]$ . We did not find significant fluctuations in  $\rho_{conv}^\gamma \times \epsilon_{reco}^\gamma \times \epsilon_{sel}^{\chi_c}$  for the different pseudorapidity ranges of the  $\chi_c$  photon.

#### 4.7.4 Reconstruction efficiency for $J/\psi$

In Chapter 4.7.2, we showed that the transverse momentum distributions of the  $J/\psi$  from  $\chi_{c1}$  and  $\chi_{c2}$  are very similar. Below we quantify the similarity in the acceptance of the  $J/\psi$  from  $\chi_{c1}$  and  $\chi_{c2}$ . We estimate the ratio of reconstruction efficiencies for  $J/\psi$  coming from  $\chi_{c1}$  and  $\chi_{c2}$ , by comparing the number of reconstructed  $J/\psi$  with respect to the generated  $J/\psi$  in the following way

$$\frac{\epsilon_1}{\epsilon_2}(J/\psi) = \frac{N_{J/\psi}^{rec}(\chi_{c1})}{N_{J/\psi}^{gen}(\chi_{c1})} / \frac{N_{J/\psi}^{rec}(\chi_{c2})}{N_{J/\psi}^{gen}(\chi_{c2})} \quad (4.20)$$

where  $N_{J/\psi}^{gen}$  are the generated  $J/\psi$  from  $\chi_{c1}$  and  $\chi_{c2}$  with Pythia Monte Carlo particle gun as explained above but without applying the mixing procedure with low  $p_T$  tracks in the kinematic range  $|y_{J/\psi}| < 1.0$ . The generated with Pythia Monte Carlo particle gun without the mixing procedure and subsequently reconstructed with CMS  $J/\psi$  from  $\chi_{c1}$  and  $\chi_{c2}$  in the kinematic range range  $|y_{J/\psi}| < 1.0$  are given by  $N_{J/\psi}^{rec}$ . The ratio  $\frac{\epsilon_1}{\epsilon_2}(J/\psi)$  is calculated for the usual  $p_T(J/\psi)$  ranges and it is shown in Figure 4.24. The values for all ranges are consistent with one within statistical uncertainties and show the similar acceptance of  $J/\psi$  from  $\chi_{c1}$  and  $\chi_{c2}$ .

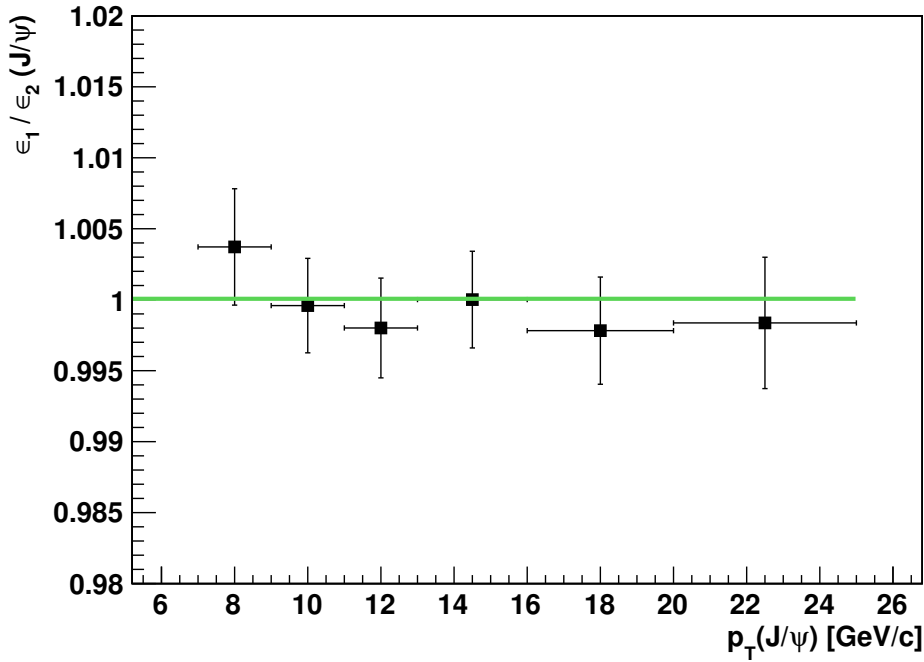


Figure 4.24: Ratio of the  $J/\psi$  detection efficiencies for  $J/\psi$  produced by decay of the simulated  $\chi_{c1}$  and  $\chi_{c2}$ . The values of the ratio of the  $J/\psi$  detection efficiencies for all  $p_T(J/\psi)$  ranges are consistent with one within statistical uncertainties.

## 4.8 Consistency checks

### Reweighting procedure

We want to test the assumption on the production  $p_T$  spectrum of the  $\chi_{c1}$  and  $\chi_{c2}$  states. For that we compare the spectra obtained from the Pythia Monte Carlo particle gun with the spectra obtained experimentally. To separate the  $\chi_{c1}$  and  $\chi_{c2}$  states in data, we start from the spectrum of all  $\chi_c$  candidates and define as  $\chi_{c1}$  candidates the ones with invariant mass in the window  $[3.45, 3.52]$  GeV/c<sup>2</sup> and as  $\chi_{c2}$  candidates the ones with invariant mass in the window  $[3.52, 3.57]$  GeV/c<sup>2</sup>. Their spectra are shown in Figure 4.13.

The ratio histograms of the generated and measured  $p_T$  spectra for  $\chi_{c1}$  and  $\chi_{c2}$  is used as a weight to reweight the events generated with the Pythia particle gun. The goal is to match the generated and observed  $p_T$  spectra for  $\chi_{c1}$  and  $\chi_{c2}$ . We recalculate the ratio  $\epsilon_1/\epsilon_2$  using reweighted events when counting the numbers  $N_{\chi_{c1}}^{rec}$  and  $N_{\chi_{c2}}^{rec}$  in Equation 4.16. The values of  $N_{\chi_{c1}}^{gen}$  and  $N_{\chi_{c2}}^{gen}$  in Equation 4.16 remain the same as in the default case.

The comparison between the default method in Section 4.7 and the method with reweighting gives a maximum difference of 3% in the ratio  $\epsilon_1/\epsilon_2$ . For example, in the range  $7.0 < p_T(J/\psi) < 25.0$  GeV/c we obtain  $\epsilon_1/\epsilon_2 = 0.958 \pm 0.022$  for the default case and  $\epsilon_1/\epsilon_2 = 0.935 \pm 0.022$  for the weighted case.

### Stability of the results with photon $p_T$

We calculate the ratios  $N_{\chi_{c2}}/N_{\chi_{c1}}$  and  $\epsilon_1/\epsilon_2$  for different cuts on  $p_T(\gamma)$ , namely 0.75, 1.00 and 1.25 GeV/c, and compare their values with the default cut value of  $p_T(\gamma) = 0.5$  GeV/c. This is done to ensure that the result for  $\frac{N_{\chi_{c2}}}{N_{\chi_{c1}}} \cdot \frac{\epsilon_1}{\epsilon_2}$  is not dependent on the steep photon reconstruction efficiency, see Figure 4.23. The fluctuations of  $\frac{N_{\chi_{c2}}}{N_{\chi_{c1}}} \cdot \frac{\epsilon_1}{\epsilon_2}$  for different cuts are of the order of 2% with maximum difference in the first  $p_T(J/\psi)$  bin of 6%. The fluctuations are all within the statistical uncertainties.

### Effect of the $\pi^0$ rejection cut

The  $\pi^0$  rejection cut which is used for the selection of  $\chi_c$  mesons in Table 4.4 could bias the measurement of  $N_{\chi_{c2}}/N_{\chi_{c1}}$ . Since  $\chi_{c2}$  emits slightly harder photons, this cut could favor the selection of slightly lower  $p_T$  photons from  $\chi_{c1}$  causing an increase of the efficiency for  $\chi_{c2}$ .

We calculated the values of  $N_{\chi_{c2}}/N_{\chi_{c1}}$  and  $\epsilon_1/\epsilon_2$  without applying the  $\pi^0$  rejection cut, see Tables 4.8 and 4.9, and found them to be compatible with the default values.

Table 4.8: Values of  $N_{\chi_{c2}}/N_{\chi_{c1}}$  without  $\pi^0$  cut.

$p_T^{J/\psi}$ [GeV/c]	$N_{\chi_{c1}}$	$N_{\chi_{c2}}$	$N_{\chi_{c2}}/N_{\chi_{c1}}$
7.0-9.0	$697 \pm 34$	$338 \pm 28$	$0.485 \pm 0.048$
9.0-11.0	$1922 \pm 56$	$912 \pm 43$	$0.475 \pm 0.027$
11.0-13.0	$2166 \pm 58$	$978 \pm 44$	$0.452 \pm 0.024$
13.0-16.0	$2038 \pm 57$	$957 \pm 44$	$0.470 \pm 0.026$
16.0-20.0	$1464 \pm 48$	$566 \pm 35$	$0.387 \pm 0.028$
20.0-25.0	$738 \pm 35$	$260 \pm 25$	$0.353 \pm 0.040$

Table 4.9: Values of  $\epsilon_1/\epsilon_2$  without  $\pi^0$  cut.

$p_T^{J/\psi}$ [GeV/c]	$\epsilon_1/\epsilon_2$
7.0-9.0	$0.902 \pm 0.028$
9.0-11.0	$0.890 \pm 0.017$
11.0-13.0	$0.909 \pm 0.016$
13.0-16.0	$0.939 \pm 0.016$
16.0-20.0	$0.922 \pm 0.017$
20.0-25.0	$0.956 \pm 0.022$

## 4.9 Systematic studies

We study separately systematic uncertainties on the ratios  $N_{\chi_{c2}}/N_{\chi_{c1}}$  and  $\epsilon_1/\epsilon_2$ . The systematic uncertainties on  $N_{\chi_{c2}}/N_{\chi_{c1}}$  come from the fit to  $\chi_{c1}$  and  $\chi_{c2}$  mass distributions while the systematic uncertainties on  $\epsilon_1/\epsilon_2$  come from simulation sample size, the effect of small changes in the efficiency curve (Figure 4.23) and the choice of the  $p_T(\chi_c)$  spectrum. Additionally, we investigate the effect of pileup on the ratio  $N_{\chi_{c2}}/N_{\chi_{c1}}$  and the effect of tracker material and the unknown  $\chi_c$  polarization on  $\epsilon_1/\epsilon_2$ .

### 4.9.1 Uncertainty from mass fit

#### Signal Model

To check that the Double Crystal Ball function provides a good representation of the  $\chi_{c1}$

and  $\chi_{c2}$  signals, we use directly the invariant mass histograms of  $\chi_{c1}$  and  $\chi_{c2}$  obtained with the Pythia Monte Carlo particle gun. The Monte Carlo histograms act as template signal PDF in the extended maximum likelihood minimization in Equation 4.11. We compare the ratio of reconstructed  $\chi_{c1}$  and  $\chi_{c2}$  candidates,  $N_{\chi_{c2}}/N_{\chi_{c1}}$ , obtained with Double Crystal Ball parametrization and template PDFs and found them to be equivalent with a maximum difference of 1% in the first  $p_T(J/\psi)$  bin. Therefore we do not assign a systematic uncertainty.

We estimate systematic uncertainties from the parametrization of our resolution function as defined in Section 4.6.1 by varying the double-sided Crystal Ball parameters  $\sigma$ ,  $\alpha_l$  and  $\alpha_r$  in Table 4.5 which were derived from the Pythia Monte Carlo particle gun within their uncertainties. Then, we build the ratio  $N_{\chi_{c2}}/N_{\chi_{c1}}$  for all possible variations of those parameters. Their values can be found in Appendix D. We observe that the largest deviations from the default value of  $N_{\chi_{c2}}/N_{\chi_{c1}}$  come from variations of the parameter  $\alpha_l$  for  $\chi_{c2}$  (cases [9] and [10]). The maximum deviation with respect to the default case in the last  $p_T(J/\psi)$  bin [20 – 25] is about four times larger than the deviations in the other bins. This is related to the fact that in the last  $p_T(J/\psi)$  bin the number of reconstructed  $\chi_c$  candidates is very low which affects the precision of the measurement.

We quote as a systematic uncertainty the maximum relative difference in  $N_{\chi_{c2}}/N_{\chi_{c1}}$  obtained with parameter variations and our default value. For the  $p_T(J/\psi)$  bin [20 – 25] we assume a systematic uncertainty of the order of the uncertainties in the other  $p_T$  bins. The values of these systematic uncertainties are reported in Table 4.13.

### Background Model

Systematic uncertainty from the background model parametrization is assigned by using an alternative background PDF defined as [4]

$$S_B = \left(1 - \exp\left(-\frac{Q - q_0}{c}\right)\right) \cdot \left(\frac{Q}{q_0}\right)^a + b \cdot \left(\frac{Q}{q_0} - 1\right) \quad (4.21)$$

where  $Q = m_{\gamma\mu\mu} - m_{\mu\mu} + m_{J/\psi}^{PDG}$ ,  $q_0 = 3.2$  and  $a$ ,  $b$  and  $c$  are free parameters in the fit. The  $S_B$  is empirical function which has been used to model the background in the  $D^{*\pm} - D^0$  invariant mass difference distribution. We take the relative difference in  $N_{\chi_{c2}}/N_{\chi_{c1}}$  obtained with this parametrization and our default parametrization as systematic uncertainty, see Table 4.13.

## 4.9.2 Uncertainty on the ratio of efficiencies $\epsilon_1/\epsilon_2$

### Simulation sample size

We have generated 240 million events with  $\chi_{c1}$  and  $\chi_{c2}$  using Pythia Monte Carlo particle gun. The sample is of such a big size due to the fact that the reconstruction efficiency of converted photons with the CMS tracker is very low. As it was discussed in Chapter 4.7.3 and Figure 4.23 for  $p_T(\gamma) = 0.5$  GeV/c, the reconstruction efficiency of the converted photons is 0.01% while for  $p_T(\gamma) = 4$  GeV/c it is about 1%. Therefore a Monte Carlo sample of a considerable size is needed for a proper calculation of the ratio  $\epsilon_1/\epsilon_2$ .

The statistical uncertainty on  $\epsilon_1/\epsilon_2$ , see Table 4.7, from the limited simulation sample size is accounted as a systematic uncertainty and their values are reported in Table 4.13.

### Efficiency curve shift

We further check the stability of the ratio of efficiencies  $\epsilon_1/\epsilon_2$  by estimating the effect of small changes in the efficiency curve with our Monte Carlo in Section 4.7.3. The uncertainty on the efficiency curve is simulated by artificially applying a shift upward by 5% and leftward by 5%. We, then, recalculate the values of  $N_{\chi_{c1}}^{rec}$  and  $N_{\chi_{c2}}^{rec}$  in Equation 4.16 by applying a weight to the generated events  $N_{\chi_{c1}}^{gen}$  and  $N_{\chi_{c2}}^{gen}$ . The weight depends on the  $p_T$  of the converted photon and it is calculated by fitting the efficiency curve in Figure 4.23. Then, the ratio  $\epsilon_1/\epsilon_2$  is recalculated using the new values of  $N_{\chi_{c1}}^{rec}$  and  $N_{\chi_{c2}}^{rec}$ .

The upward shift of 5% of the efficiency curve has no effect because it cancels in the ratio. The leftward shift of 5% has an impact which depends on  $p_T(J/\psi)$ . The maximum deviation between the default and shifted values of  $\epsilon_1/\epsilon_2$  is in the  $p_T(J/\psi)$  bin [20 – 25] and it is about 1% therefore we chose to not assign a systematic uncertainty.

### Choice of $p_T(\chi_c)$ spectrum

As discussed in Section 4.7, we modeled the  $p_T(\chi_c)$  spectrum with the  $p_T(\psi')$  distribution measured with the CMS experiment. Two variations for the  $p_T(\chi_c)$  spectrum are investigated and a systematic uncertainty is assigned with respect to the default case. The first variation uses the  $p_T(J/\psi)$  spectrum measured with CMS experiment and the second generates  $\chi_c$  with a flat  $p_T$  spectrum. Similarly to the  $p_T(\psi')$  spectrum, we use the data available in [45] for the  $J/\psi$  momentum spectrum in the range  $|y(J/\psi)| < 0.9$  and parametrize the data using the

expression in Equation 4.13. The fitted  $p_T(J/\psi)$  spectrum used to model the  $p_T(\chi_c)$  spectrum is shown in Appendix E.

The ratio  $\epsilon_1/\epsilon_2$  is evaluated for both hypotheses and the corresponding results compared with the default values are shown in Table 4.10.

Table 4.10: Values of  $\epsilon_1/\epsilon_2$  for different choices of input  $p_T(\chi_c)$  spectrum.

$p_T(J/\psi)$	$\psi'$	$J/\psi$	flat
7.0-9.0	$0.903 \pm 0.023$	$0.910 \pm 0.022$	$0.963 \pm 0.027$
9.0-11.0	$0.935 \pm 0.019$	$0.924 \pm 0.018$	$0.956 \pm 0.018$
11.0-13.0	$0.945 \pm 0.021$	$0.973 \pm 0.021$	$0.964 \pm 0.018$
13.0-16.0	$0.917 \pm 0.022$	$0.926 \pm 0.023$	$0.987 \pm 0.018$
16.0-20.0	$0.981 \pm 0.031$	$0.899 \pm 0.028$	$0.961 \pm 0.020$
20.0-25.0	$1.028 \pm 0.049$	$1.022 \pm 0.046$	$1.004 \pm 0.026$

The values of  $\epsilon_1/\epsilon_2$  evaluated using the  $p_T(J/\psi)$  spectrum are statistically compatible with the corresponding values of  $\epsilon_1/\epsilon_2$  using the  $p_T(\psi')$  spectrum. The flat  $p_T$  spectrum is the extreme scenario with respect to the observed rapidly falling  $\chi_c$  momentum distribution. The relative differences between the  $\psi'$  spectrum and the flat  $p_T$  spectrum vary between 2% and 7% in various  $p_T(J/\psi)$  ranges.

We use the difference in the ratio  $\epsilon_1/\epsilon_2$  between the flat  $p_T$  spectrum and the  $p_T(\psi')$  spectrum to evaluate the systematic uncertainty associated to the choice of the input  $p_T$  spectrum. To do so, we fit the values of  $\epsilon_1/\epsilon_2$  obtained with the flat case and  $\psi'$  case with a straight line, and we quote as relative systematic uncertainty the relative difference between the fit function at any given value of  $p_T(J/\psi)$ . This procedure is illustrated in Figure 4.25 and the corresponding results are in Table 4.13.

### Tracker material

Reliable determination of  $\epsilon_1/\epsilon_2$  relies on the correct simulation of the tracker detector material. The tracker geometry, as implemented in CMSSW, consists of 350000 volumes, 95% of which filled with an average mixture of components from the real tracker like support structure, cooling and power elements etc. The other 5% of the volumes are silicon sensors which are the most accurately known components of the tracker. A detailed table in [58] shows the basic components of the tracker volume. Therefore by definition the material in the tracker is described only approximately. The quantity used to determine the impact of the tracker



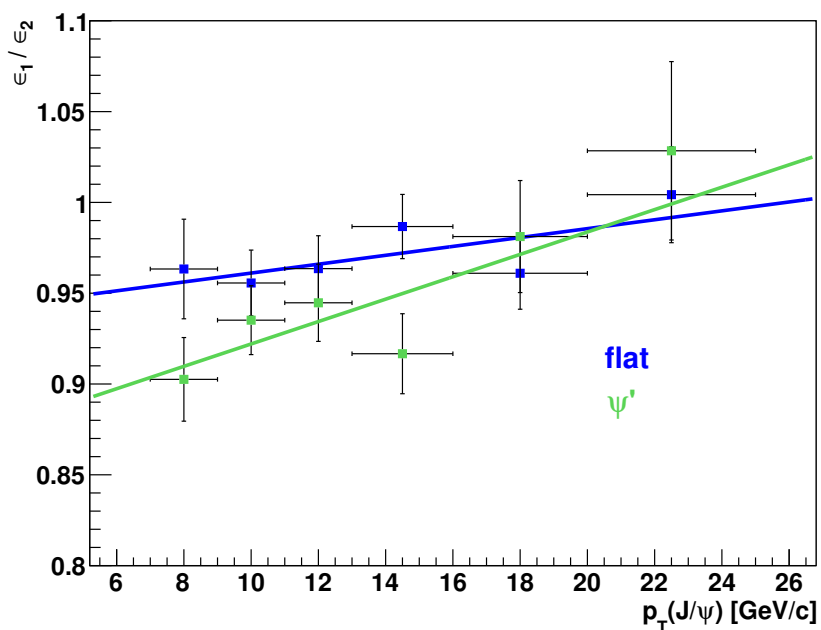


Figure 4.25: Values of  $\epsilon_1/\epsilon_2$  for the  $\psi'$  and flat input spectrum and their fit to a straight line. Uncertainties are statistical and are due to limited size of the simulation sample.

material on the reconstruction performance of charged particle tracks is the radiation length,  $X_0$ .

Two modified material scenarios are prepared as in [58] and they correspond to a minimal and maximal increase of the average radiation length,  $X_0^{\min} = -3\%$  and  $X_0^{\max} = 8\%$ , by assuming that 5% of the tracker mass is not represented in the simulation.

The resulting values of  $\epsilon_1/\epsilon_2$  in the range  $7.0 < p_T(J/\psi) < 25.0$  GeV/c are  $0.955 \pm 0.007$ ,  $0.951 \pm 0.009$ , and  $0.948 \pm 0.009$  respectively for nominal geometry,  $X_0^{\min}$  and  $X_0^{\max}$ . This shows that increase or decrease in the conversion probability for both states cancels in the ratio. No significant difference in  $\epsilon_1/\epsilon_2$  is observed and the corresponding systematic uncertainty is assumed to be negligible.

### 4.9.3 Pileup

The LHC instantaneous luminosity in 2011 was high enough that there are many parton collisions per bunch crossing. Apart from the hard process of interest there are many interactions

which are characterized with small momentum transfer. These multiple interactions are called pileup interactions. As a result of the pileup interactions, the number of primary vertices in the events increases.

The 2011 data is divided into two periods, 2011A and 2011B, see Table 4.2, which are characterized with different instantaneous luminosities. Different instantaneous luminosity leads to a different average number of primary vertices per bunch crossing. Multiple vertices and increased track density influence the reconstruction efficiency of the  $\chi_c$  candidates. The stability of our analysis as a function of the number of primary vertices in the event has been investigated.

The number of primary vertices for each periods, 2011A and 2011B, is shown in Figure 4.26. For 2011A period most of the events have on average six primary vertices, for 2011B period the average number of vertices is nine and they are distributed in the  $z$  direction with spread of 6 cm. We perform two studies to check the stability of our measurement: calculate the ratio  $N_{\chi_{c2}}/N_{\chi_{c1}}$  in bins up to a given number of vertices as well as in individual bins of number of vertices, see Table 4.11.

Table 4.11: Number of vertices in bins up to a given number (Case 1) and in individual bins (Case 2) for Run 2011A and Run 2011B.

<b>Run 2011A</b>	
Case 1	[1 – 2], [1 – 3], [1 – 4], [1 – 5] [1 – 6], [1 – 7], [1 – 8], [1 – 9] [1 – 10], [1 – 11], [1 – 12], [1 – 13] [1 – 14], [1 – 15], [1 – 16]
Case 2	[1 – 4], [5 – 6], [7 – 8], [9 – 16]
<b>Run 2011B</b>	
Case 1	[1 – 2], [1 – 3], [1 – 4], [1 – 5] [1 – 6], [1 – 7], [1 – 8], [1 – 9] [1 – 10], [1 – 11], [1 – 12], [1 – 13] [1 – 14], [1 – 15], [1 – 16], [1 – 17], [1 – 18]
Case 2	[1 – 4], [5 – 6], [7 – 9], [10 – 18]

For example, bin [1 – 2] means events with number of primary vertices 1 and 2, bin [1 – 4] means events with number of primary vertices between 1 and 4. The ratio  $N_{\chi_{c2}}/N_{\chi_{c1}}$  is calculated and plotted for each bin of primary vertices. The results are illustrated in Figure 4.26.

Both studies show independence of  $N_{\chi_{c2}}/N_{\chi_{c1}}$  from the number of primary vertices in the

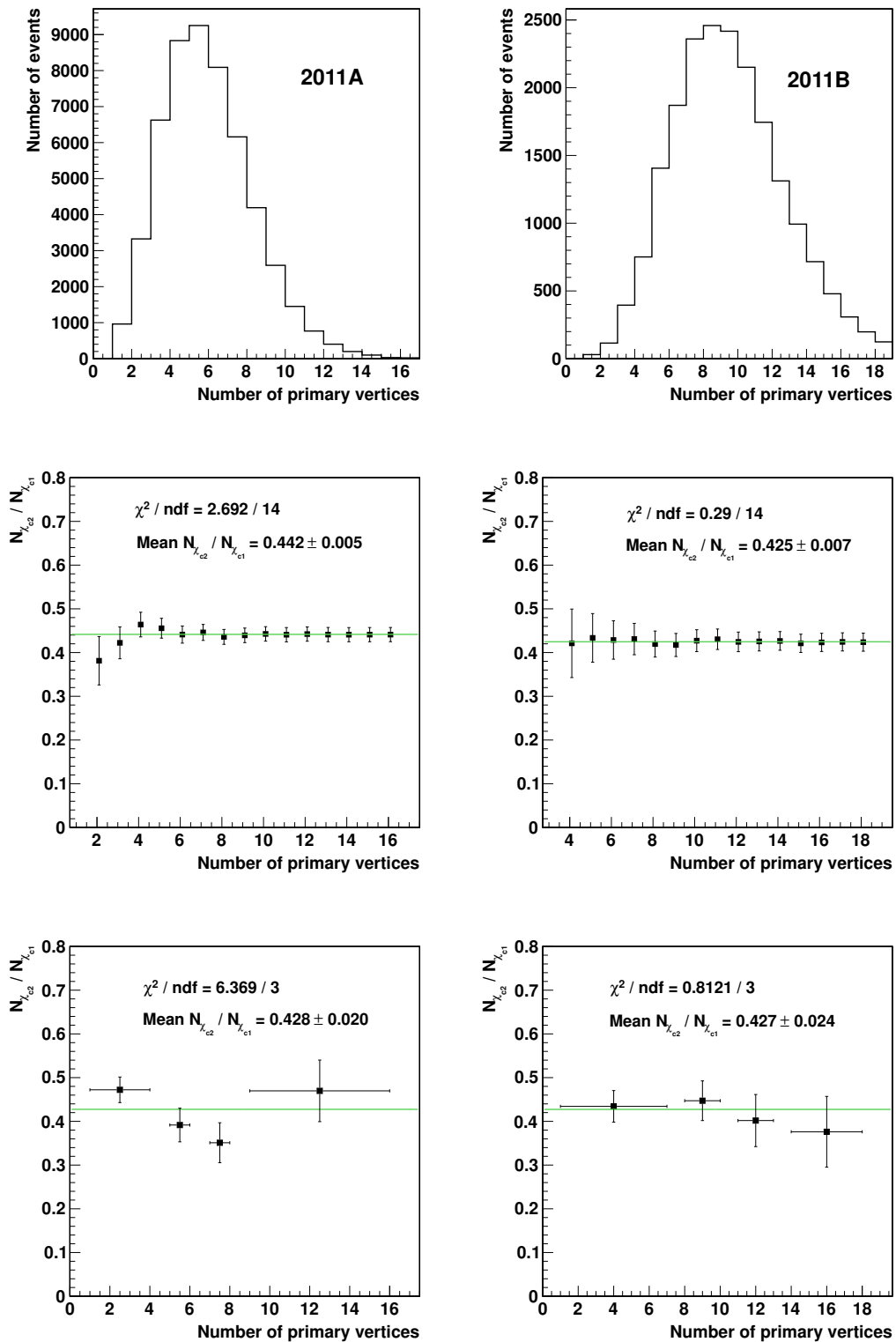


Figure 4.26: Top: Distribution of the number of primary vertices in Run2011A (left) and Run2011B (right). Middle: stability of the ratio  $N_{\chi_{c2}}/N_{\chi_{c1}}$  in bins up to a given number of vertices (Case 1) for Run2011A (left) and Run2011B (right). Bottom: stability of the ratio  $N_{\chi_{c2}}/N_{\chi_{c1}}$  for individual bins of the number of vertices (Case 2) for Run2011A (left) and Run2011B (right).

event. For Case 1, the ratio of  $N_{\chi_{c2}}/N_{\chi_{c1}}$  for all bins up to a given number converges to the value of  $N_{\chi_{c2}}/N_{\chi_{c1}}$  obtained with the maximum number of primary vertices observed in data (the last data point in the middle plots in Figure 4.26). The fluctuations in the first bin for Run2011A are due to low statistics. The ratio of  $N_{\chi_{c2}}/N_{\chi_{c1}}$  for Case 1 and Case 2 has been fitted with a straight line. The maximum deviation from the straight line is statistically not significant and it is quantitatively measured by the corresponding  $p$  value of the  $\chi^2$  distribution. For 2011A period it is  $p = 0.99$ (Case 1)/ $0.09$ (Case 2) and for 2011B period it is  $p = 1$ (Case 1)/ $0.84$ (Case 2). Therefore we do not assign a systematic uncertainty due to pileup.

#### 4.9.4 $\chi_c$ polarization

The  $\chi_c$  polarization influences the angular correlation between the  $\chi_c$  decay products and hence the  $\gamma$  and the  $J/\psi$  transverse momentum distribution. This consequently affects the efficiency of their detection with the CMS experiment. For the calculation of the ratio of efficiencies  $\epsilon_1/\epsilon_2$  we used the Monte Carlo particle gun which generates unpolarized  $\chi_c$  particles. Since the polarization of  $\chi_{c1}$  and  $\chi_{c2}$  is unknown we evaluate the ratio of efficiencies with a coefficient that takes different  $\chi_c$  polarization states into account.

The  $\chi_c$  decay depends on three angles which define the angular correlations among  $\chi_c$ ,  $J/\psi$  and  $\gamma$ , see Figure 4.15. It was discussed in Section 4.7 that the angular distributions for  $\theta$ ,  $\theta'$  and  $\phi'$  as generated with the Monte Carlo particle gun are isotropic. The isotropic  $\theta'$  distribution was corrected by a reweighting procedure to reproduce the physically correct decay angular distribution for the  $J/\psi$ .

To account for  $\chi_c$  polarization, we reweight all angular distributions with a function  $W(\theta, \theta', \phi')$  [53, 63] which predicts the angular distribution of decay products for different polarization scenarios of  $\chi_c$ . These decay angular distributions are calculated as a function of the angular momentum composition of the decaying  $\chi_c$  meson and of the multipole structure of the photon radiation.

#### Decay angular distributions $W(\theta, \theta', \phi')$

The decay angular distribution  $W(\theta, \theta', \phi')$  for  $\chi_{c1}$  and  $\chi_{c2}$  are parametrized as

- $\chi_{c1}$

$$\begin{aligned}
W(\theta, \theta', \phi') &= k_1 + k_2 \cos^2 \theta + (k_3 + k_4 \cos^2 \theta) \cos^2 \theta' \\
&\quad + k_5 \sin^2 \theta \sin^2 \theta' \cos \phi'
\end{aligned} \tag{4.22}$$

- $\chi_{c2}$

$$\begin{aligned}
W(\theta, \theta', \phi') &= k_1 + k_2 \cos^2 \theta + k_3 \cos^4 \theta + (k_4 + k_5 \cos^2 \theta + k_6 \cos^4 \theta) \cos^2 \theta' \\
&\quad + (k_7 + k_8 \cos^2 \theta + k_9 \cos^4 \theta) \sin^2 \theta' \cos 2\phi' \\
&\quad + (k_{10} + k_{11} \cos^2 \theta) \sin 2\theta \sin 2\theta' \cos \phi'
\end{aligned} \tag{4.23}$$

where  $\theta$  is the polar angle of the  $J/\psi$  with respect to the proton direction in the  $\chi_c$  rest frame,  $\theta'$  and  $\phi'$  are the polar and azimuthal angles of the muon in the  $J/\psi$  rest frame with respect to the  $J/\psi$  direction seen from the  $\chi_c$  rest frame. More information about the decay angular distributions  $W(\theta, \theta', \phi')$  with explanation of the meaning of the various coefficients can be found in Appendix F.

The angular distributions,  $W(\theta, \theta', \phi')$ , depend on the choice of the coordinate system. There are two standard coordinate systems [52] to study quarkonium polarization, the helicity and Collins-Soper [59] frames, with respect to which the momenta of decay products are expressed in spherical coordinates. The two frames use different convention for the orientation of the  $z$  axis: the flight direction of the  $\chi_c$  in center-of-mass of the colliding beams (helicity frame) and the bisector of the angle between one beam and the opposite of the other beam in the  $\chi_c$  rest frame (Collins-Soper frame). The two frames are mutually orthogonal by a rotation of  $90^\circ$  around the  $y$  axis, defined as a perpendicular to the plane of the colliding beams momenta. Since we do not know the  $\chi_c$  polarization, for the evaluation of  $W(\theta, \theta', \phi')$  we use both coordinate systems.

We define several polarization cases for the  $\chi_{c1}$  and  $\chi_{c2}$  mesons in the following way. The  $\chi_{c1}$  and  $\chi_{c2}$  mesons have total angular momentum,  $J$ , equal to 1 and 2 respectively. The helicity,  $h = \vec{J} \cdot \vec{p} / |\vec{p}|$ , is defined as a projection of the particle's total angular momentum,  $\vec{J}$ , along its momentum direction  $\vec{p}$ . Therefore the  $\chi_{c1}$  states can have helicities  $h_{\chi_{c1}} = 0, \pm 1$  while the  $\chi_{c2}$  states can have helicities  $h_{\chi_{c2}} = 0, \pm 1, \pm 2$ . An unpolarized  $\chi_{c1}$  has the same probability to be

found in each of the helicity states,  $-1, 0, 1$  and an unpolarized  $\chi_{c2}$  has the same probability to be found in each of the helicity states,  $-2, -1, 0, 1, 2$ .

Figure 4.27 shows the  $\cos\theta$  angular distributions for unpolarized  $\chi_{c1}$  and  $\chi_{c2}$  and different helicity states of  $\chi_{c1}$  and  $\chi_{c2}$  after reweighting with angular distributions  $W(\theta, \theta', \phi')$  in helicity frame. Figure 4.28 shows how the  $p_T(\gamma)$  distribution changes with different polarization scenarios. This effect is related to the different photon direction,  $\cos\theta$ , for various  $\chi_c$  helicity states in combination with the boost direction in proton-proton center-of-mass frame. The corresponding  $\cos\theta$  and  $p_T(\gamma)$  distributions in Collins-Soper frame are shown in Appendix G.

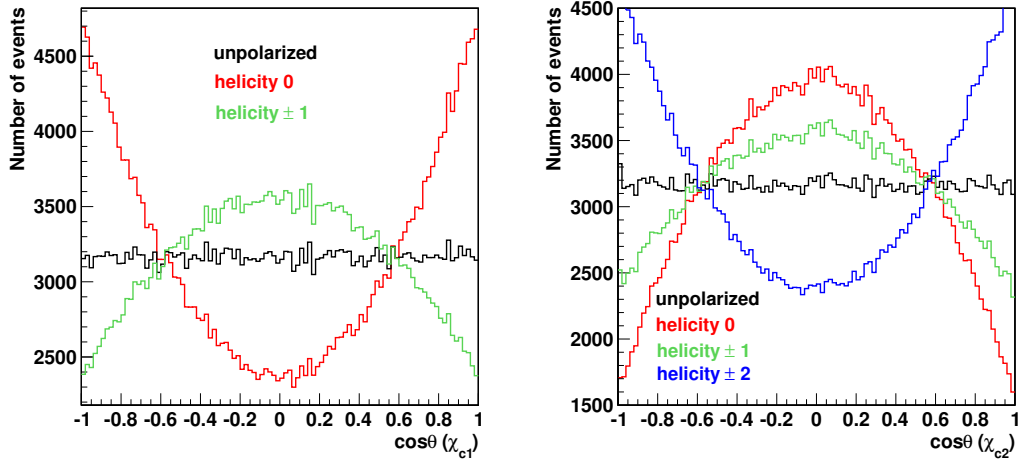


Figure 4.27: Angle between the direction of the  $J/\psi$  and  $\chi_c$  as seen in  $\chi_c$  rest frame for unpolarized, helicities  $0, \pm 1$  and  $\pm 2$   $\chi_c$  states in the helicity frame. Left:  $\chi_{c1}$ , right:  $\chi_{c2}$ .

The  $p_T(\gamma)$  distributions change for different polarization scenarios which affects the efficiency of the photon detection with the CMS detector. As a result, the ratio  $\epsilon_1/\epsilon_2$  changes for different  $\chi_c$  polarization scenarios. Therefore we evaluate the ratio  $\epsilon_1/\epsilon_2$  using Equation 4.16 for unpolarized  $\chi_{c1}$  or with helicity  $h_{\chi_{c1}} = 0, \pm 1$  in combination with unpolarized  $\chi_{c2}$  or with helicity  $h_{\chi_{c2}} = 0, \pm 1, \pm 2$ . Both of the values  $N^{rec}$  and  $N^{gen}$  in Equation 4.16 are evaluated by assuming that the  $\chi_{c1}$  and  $\chi_{c2}$  states are produced in a specific helicity state. Table 4.12 reports correction factors to default measurement of  $\epsilon_1/\epsilon_2$  for different polarization scenarios and for each  $p_T(J/\psi)$  range in helicity frame where the correction factor  $\mathcal{P}$  is calculated as

$$\mathcal{P}(h_{\chi_{c1}}, h_{\chi_{c2}}) = \frac{R(h_{\chi_{c1}}, h_{\chi_{c2}})}{R(Unpolarized_{\chi_{c1}}, Unpolarized_{\chi_{c2}})}. \quad (4.24)$$

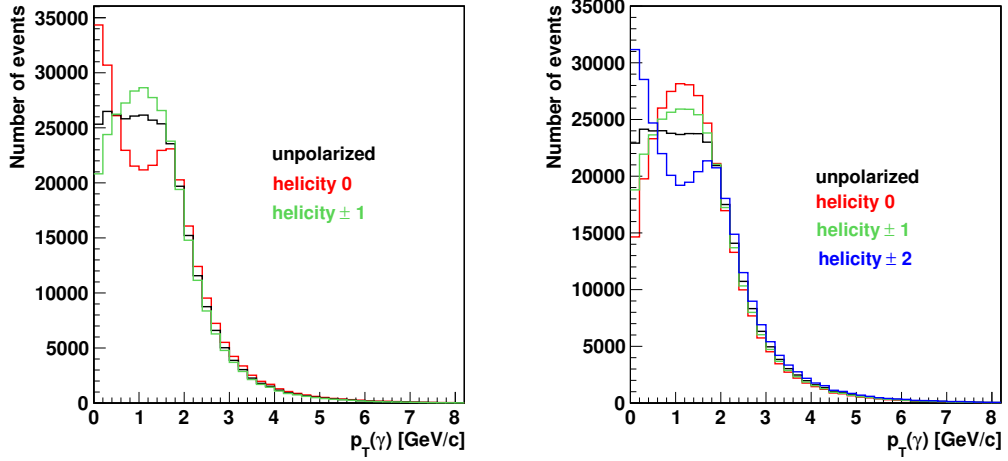


Figure 4.28:  $p_T$  distributions of the photon from  $\chi_{c1}$  (left) and  $\chi_{c2}$  (right) for unpolarized, helicities 0,  $\pm 1$  and  $\pm 2$   $\chi_c$  states in the helicity frame.

The values of  $R(\text{Unpolarized}_{\chi_{c1}}, \text{Unpolarized}_{\chi_{c2}})$  are reported in Table 4.7 and the values of  $R(h_{\chi_{c1}}, h_{\chi_{c2}})$  is the ratio  $\epsilon_1/\epsilon_2$  calculated for different helicity combinations. The maximum deviation with respect to the unpolarized case is for helicity combinations  $(h_{\chi_{c1}}, h_{\chi_{c2}}) = (0, 0)$  and  $(h_{\chi_{c1}}, h_{\chi_{c2}}) = (\pm 1, \pm 2)$  found to be about  $\mathcal{P} \sim 0.73$  and  $\mathcal{P} \sim 1.29$  respectively. The same table corresponding to Collins-Soper frame can be found in Appendix G. Again, we observe that the maximum deviation with respect to the unpolarized case is for helicity combinations  $(h_{\chi_{c1}}, h_{\chi_{c2}}) = (0, 0)$  and  $(h_{\chi_{c1}}, h_{\chi_{c2}}) = (\pm 1, \pm 2)$  but this effect is smaller with respect to the one observed in the helicity frame.

#### 4.9.5 Systematics summary

Table 4.13 gives a summary of the various sources of systematic uncertainties. The total uncertainty is calculated as the sum of individual uncertainties in quadrature. At low  $p_T(J/\psi)$ , systematics are dominated by the choice of  $p_T(\chi_c)$  spectrum, at high  $p_T(J/\psi)$  they are dominated by signal and background model parametrization. The major source of uncertainty comes from simulation sample size and it equally populates all  $p_T(J/\psi)$  bins.

We chose to report the systematic uncertainties from  $\chi_c$  polarization separately and they will be discussed in Section 4.10.

Table 4.12: The values of  $\epsilon_1/\epsilon_2$  for different polarization scenarios in the helicity frame relative to the unpolarized case.

$\mathcal{P}(h_{\chi_{c1}}, h_{\chi_{c2}})$	$p_T(J/\psi)[\text{GeV}/c]$					
	7–9	9–11	11–13	13–16	16–20	20–25
$\mathcal{P}(\text{Unpolarized}, 0)$	0.886	0.871	0.855	0.857	0.847	0.862
$\mathcal{P}(\text{Unpolarized}, \pm 1)$	0.920	0.935	0.938	0.930	0.945	0.935
$\mathcal{P}(\text{Unpolarized}, \pm 2)$	1.203	1.204	1.212	1.201	1.201	1.172
$\mathcal{P}(0, \text{Unpolarized})$	0.832	0.839	0.848	0.848	0.854	0.861
$\mathcal{P}(\pm 1, \text{Unpolarized})$	1.077	1.072	1.068	1.068	1.067	1.064
$\mathcal{P}(0, 0)$	0.737	0.730	0.725	0.727	0.723	0.743
$\mathcal{P}(0, \pm 1)$	0.765	0.783	0.795	0.788	0.806	0.805
$\mathcal{P}(0, \pm 2)$	1.001	1.010	1.028	1.019	1.025	1.010
$\mathcal{P}(\pm 1, 0)$	0.954	0.933	0.913	0.916	0.904	0.917
$\mathcal{P}(\pm 1, \pm 1)$	0.991	1.003	1.001	0.993	1.008	0.995
$\mathcal{P}(\pm 1, \pm 2)$	1.295	1.291	1.294	1.283	1.281	1.247

Table 4.13: Relative systematic uncertainties on  $\frac{\sigma(\chi_{c2})\mathcal{B}(\chi_{c2})}{\sigma(\chi_{c1})\mathcal{B}(\chi_{c1})}$  for various  $p_T(J/\psi)$  from different sources and the sum of individual uncertainties in quadrature.

$p_T(J/\psi)$ range [GeV/c]	7–9	9–11	11–13	13–16	16–20	20–25
Source of uncertainty	Relative uncertainty (%)					
Simulation Sample Size	2.6	2.0	2.2	2.4	3.1	4.8
Choice of $p_T(\chi_c)$ spectrum	4.5	3.7	2.9	1.9	0.6	1.1
Signal Model	1.4	3.0	1.1	1.5	1.6	2.2
Background Model	1.4	1.5	0.9	1.2	1.8	2.4
Total uncertainty	5.5	5.4	3.9	3.6	4.0	5.9

## 4.10 Results

The results of the measurements of

$$\frac{\sigma(pp \rightarrow \chi_{c2} + X)}{\sigma(pp \rightarrow \chi_{c1} + X)} \quad \text{and} \quad \frac{\sigma(pp \rightarrow \chi_{c2} + X)\mathcal{B}(\chi_{c2} \rightarrow J/\psi + \gamma)}{\sigma(pp \rightarrow \chi_{c1} + X)\mathcal{B}(\chi_{c1} \rightarrow J/\psi + \gamma)} \quad (4.25)$$

are reported in Tables 4.14 and 4.15 for different ranges of  $p_T(J/\psi)$ . The ratio of decay branching fractions is

$$\frac{\mathcal{B}(\chi_{c1} \rightarrow J/\psi + \gamma)}{\mathcal{B}(\chi_{c2} \rightarrow J/\psi + \gamma)} = \frac{34.4 \pm 1.5}{19.5 \pm 0.8} = 1.76 \pm 0.10 \quad (4.26)$$

assuming the two values are uncorrelated. Therefore the systematic uncertainty on the ratio



of cross sections due to branching ratio uncertainties is about 6%. In Tables 4.14 and 4.15 the first uncertainty is statistical, the second uncertainty is systematic and the third uncertainty in Table 4.15 comes from the branching fractions. Separate columns are dedicated to the uncertainty deriving from the extreme polarization scenarios  $(h_{\chi_{c1}}, h_{\chi_{c2}}) = (0, 0)$  and  $(h_{\chi_{c1}}, h_{\chi_{c2}}) = (\pm 1, \pm 2)$  in the helicity and Collins-Soper frames. They show that the uncertainty from unknown  $\chi_c$  polarization can change the ratio  $\sigma(\chi_{c2})/\sigma(\chi_{c1})$  by 25%. In Figure 4.29 a visual representation of the results is given.

Table 4.14: Measurements of  $\frac{\sigma(\chi_{c2})\mathcal{B}(\chi_{c2})}{\sigma(\chi_{c1})\mathcal{B}(\chi_{c1})}$  for various values of  $p_T(J/\psi)$ . The first uncertainty is statistical, the second is systematic. The last two columns report the uncertainty deriving from the extreme polarization scenarios in the helicity and Collins-Soper frames.

$p_T(J/\psi)[GeV/c]$	$\frac{\sigma(\chi_{c2})\mathcal{B}(\chi_{c2})}{\sigma(\chi_{c1})\mathcal{B}(\chi_{c1})}$	Pol. HX	Pol. CS
7.0-9.0	$0.460 \pm 0.044(\text{stat}) \pm 0.025(\text{syst})$	+0.136 -0.121	+0.037 -0.023
9.0-11.0	$0.439 \pm 0.025(\text{stat}) \pm 0.024(\text{syst})$	+0.128 -0.119	+0.052 -0.035
11.0-13.0	$0.426 \pm 0.024(\text{stat}) \pm 0.017(\text{syst})$	+0.125 -0.117	+0.059 -0.042
13.0-16.0	$0.442 \pm 0.025(\text{stat}) \pm 0.016(\text{syst})$	+0.125 -0.121	+0.065 -0.044
16.0-20.0	$0.377 \pm 0.028(\text{stat}) \pm 0.015(\text{syst})$	+0.106 -0.104	+0.059 -0.042
20.0-25.0	$0.379 \pm 0.041(\text{stat}) \pm 0.022(\text{syst})$	+0.094 -0.097	+0.055 -0.040

Table 4.15: Measurements of  $\sigma(\chi_{c2})/\sigma(\chi_{c1})$  for various values of  $p_T(J/\psi)$ . The first uncertainty is statistical, the second is systematic, the third is the branching fractions uncertainty. Two separate columns report the uncertainty deriving from the extreme polarization scenarios in the helicity and Collins-Soper frames.

$p_T(J/\psi)[GeV/c]$	$\sigma(\chi_{c2})/\sigma(\chi_{c1})$	Pol. HX	Pol. CS
7.0-9.0	$0.811 \pm 0.078(\text{stat}) \pm 0.045(\text{syst}) \pm 0.046(\mathcal{B})$	+0.239 -0.213	+0.066 -0.041
9.0-11.0	$0.774 \pm 0.044(\text{stat}) \pm 0.042(\text{syst}) \pm 0.044(\mathcal{B})$	+0.225 -0.209	+0.092 -0.061
11.0-13.0	$0.752 \pm 0.042(\text{stat}) \pm 0.029(\text{syst}) \pm 0.043(\mathcal{B})$	+0.221 -0.207	+0.105 -0.074
13.0-16.0	$0.780 \pm 0.044(\text{stat}) \pm 0.028(\text{syst}) \pm 0.044(\mathcal{B})$	+0.221 -0.213	+0.115 -0.078
16.0-20.0	$0.665 \pm 0.049(\text{stat}) \pm 0.027(\text{syst}) \pm 0.038(\mathcal{B})$	+0.187 -0.184	+0.104 -0.074
20.0-25.0	$0.669 \pm 0.072(\text{stat}) \pm 0.039(\text{syst}) \pm 0.038(\mathcal{B})$	+0.165 -0.172	+0.096 -0.070

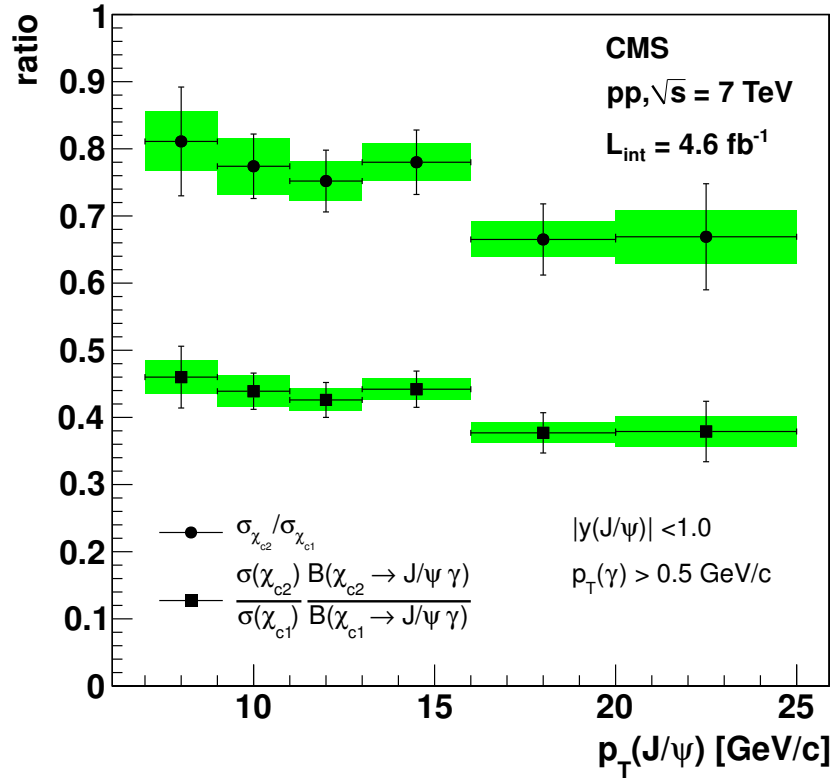


Figure 4.29: Ratio of the  $\chi_{c2}$  to  $\chi_{c1}$  production cross sections (circles) and the ratio of the cross sections times the branching fractions to  $J/\psi + \gamma$  (squares) as a function of the  $J/\psi$  transverse momentum. The green band corresponds to the systematic uncertainties and the error bars to the statistical uncertainties. For the cross section ratios the 6% uncertainty from the branching fractions is not included [64].

## 4.11 Comparison with theory

We compare our results with two theory predictions:  $k_T$  factorization [60, 61] and next-to-leading order (NLO) Non-Relativistic QCD [28].

The first calculation predicts that both  $\chi_{c1}$  and  $\chi_{c2}$  are produced in an almost pure zero helicity state in the helicity frame. Therefore in our comparison, we apply the corresponding correction factor on the ratio of efficiencies  $\epsilon_1/\epsilon_2$  from Table 4.12 which amounts to about 0.73 and is almost independent of  $p_T(J/\psi)$ . The theoretical calculation is given in the same kinematic range  $p_T(\gamma) > 0.5$  GeV/c and  $|y(J/\psi)| < 1.0$  as our measurement.

For the NLO NRQCD calculation, we do not have information about  $\chi_c$  polarization and we used the ratio of efficiencies estimated in the unpolarized case for the comparison. The theory prediction is given in the kinematic range  $p_T(\gamma) > 0$  GeV/c and  $|y(J/\psi)| < 1.0$ . We used the same Monte Carlo simulation described in Section 4.7 to derive a correction factor that takes into account the extrapolation from our fiducial phase space to the one used in the theoretical calculation. The correction factor,  $R_{extr}$ , is calculated as

$$R_{extr} = \frac{\frac{N_{\chi_{c2}}^{gen}(|y(J/\psi)| < 1.0, p_T(\gamma) > 0.5 \text{ GeV}/c)}{N_{\chi_{c2}}^{gen}(|y(J/\psi)| < 1.0)}}{\frac{N_{\chi_{c1}}^{gen}(|y(J/\psi)| < 1.0, p_T(\gamma) > 0.5 \text{ GeV}/c)}{N_{\chi_{c1}}^{gen}(|y(J/\psi)| < 1.0)}} \quad (4.27)$$

where  $N^{gen}$  are the generated  $\chi_{c1}$  and  $\chi_{c2}$  with the Pythia Monte Carlo particle gun in the corresponding phase space of  $y(J/\psi)$  and  $p_T(\gamma)$ . The values of  $R_{extr}$  have been calculated for unpolarized scenario and the two extreme polarization scenarios,  $(h_{\chi_{c1}}, h_{\chi_{c2}}) = (0, 0)$  and  $(h_{\chi_{c1}}, h_{\chi_{c2}}) = (\pm 1, \pm 2)$ , in helicity frame.

The results in Table 4.14 are multiplied with the values of  $R_{extr}$  which amounts to about 0.98 for the default unpolarized case and to about 0.83 and 1.13 for the extreme polarization scenarios, to get the new extrapolated values of  $\frac{\sigma(\chi_{c2})\mathcal{B}(\chi_{c2})}{\sigma(\chi_{c1})\mathcal{B}(\chi_{c1})}$  in the kinematic range  $p_T(\gamma) > 0$  GeV/c and  $|y(J/\psi)| < 1.0$ . The 2% systematic uncertainty on the estimation of the correction factor, coming from the difference on the factor calculated with the  $p_T(\psi')$  spectrum and with the flat  $p_T$  spectrum, is added in quadrature to the other systematic uncertainties.

The result of the two comparisons is shown in Figure 4.30. The  $k_T$  factorization prediction is represented by a line because uncertainties due to choice of  $\alpha_s$ , gluon densities etc. cancel

out in the ratio. The  $k_T$  factorization prediction reproduces well the trend of  $\frac{\sigma(\chi_{c2})\mathcal{B}(\chi_{c2})}{\sigma(\chi_{c1})\mathcal{B}(\chi_{c1})}$  versus transverse momentum of the  $J/\psi$ , but with a global normalization off by a factor two with respect to our measurement. On the other hand, the NLO NRQCD prediction is compatible with our data within experimental and theoretical uncertainties. The theoretical uncertainties in NLO NRQCD prediction are dominated by the unknown color octet matrix elements, which are extracted from Tevatron data.

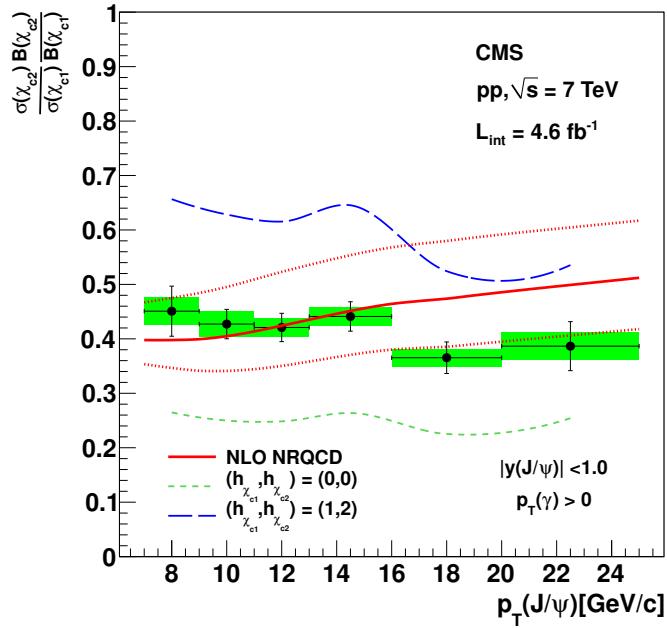
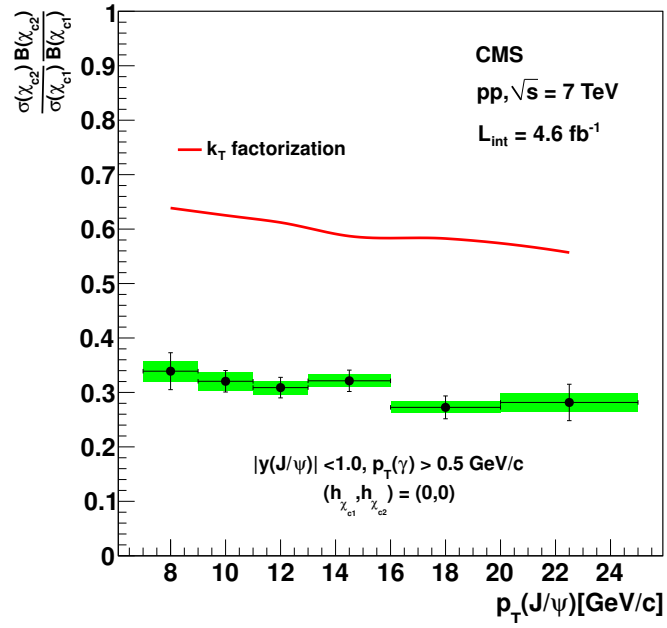


Figure 4.30: Top: Comparison of the production ratio  $\frac{\sigma(\chi_{c2})\mathcal{B}(\chi_{c2})}{\sigma(\chi_{c1})\mathcal{B}(\chi_{c1})}$  with  $k_T$  factorization approach [61]. The measurement is corrected with an acceptance factor assuming zero helicity for the  $\chi_c$  states. The  $k_T$  factorization prediction is represented by a line because theoretical uncertainties cancel out in the ratio. Bottom: Comparison of the production ratio  $\frac{\sigma(\chi_{c2})\mathcal{B}(\chi_{c2})}{\sigma(\chi_{c1})\mathcal{B}(\chi_{c1})}$  with NLO NRQCD [28] calculations. The measurement is corrected to match the kinematic range used in NLO NRQCD calculations which assume the  $\chi_c$  are produced unpolarized. The two extreme polarization scenarios in helicity frame are shown by blue and green dashed lines. The NLO NRQCD prediction is a band (red color), reflecting the uncertainties in the fitted values of the color octet matrix elements [64].

## CHAPTER 5

### Conclusions

We measured the cross section ratio of excited charmonia states  $\chi_{c1}$  and  $\chi_{c2}$  for different  $J/\psi$   $p_T$  ranges using the CMS detector at LHC. The  $\chi_c$  mesons were reconstructed through their decays into a  $J/\psi$  and a photon. The  $J/\psi$  was reconstructed with two oppositely charged muons detected in the CMS tracker and muon chambers. The photons were reconstructed through conversions in the tracker. An unbinned extended maximum likelihood fit to the data was used to extract the number of  $\chi_{c1}$  and  $\chi_{c2}$  candidates. The signal shape of  $\chi_{c1}$  and  $\chi_{c2}$  was modeled with a Double Crystal Ball PDF while the  $\chi_{c0}$  shape was modeled with a Single Crystal Ball PDF. For the combinatorial background a generic PDF which consists of a product of exponential and power law functions was used.

Using a Monte Carlo generator, a correction factor to the observed numbers of  $\chi_{c1}$  and  $\chi_{c2}$  candidates was calculated to account for detector acceptance and reconstruction efficiency. Several sources of systematic uncertainties were evaluated and their effect on the cross section ratio was estimated. The unknown  $\chi_c$  polarization represents the biggest source of uncertainty on the measured ratio. Correction coefficients to the ratio were evaluated to account for different  $\chi_{c1}$  and  $\chi_{c2}$  polarization states and to allow an easier comparison with theory predictions.

The result was compared with two theory predictions:  $k_T$  factorization and NLO Non-Relativistic QCD. None of these models gives a fully satisfactory description of the data. The trend of  $\sigma(\chi_{c2})/\sigma(\chi_{c1})$  in data is well described by the  $k_T$  factorization approach but the normalization is off by a factor of two. In the  $k_T$  factorization calculations, the  $\chi_{c1}$  and  $\chi_{c2}$  wave functions are assumed to be identical, following the results of potential model calculations which neglect spin-orbit interactions [60]. A large deviation from the assumption of identical  $\chi_{c1}$  and

$\chi_{c2}$  wave functions may explain why the  $p_T(J/\psi)$  dependence of the ratio is the same and the difference is a global scale factor [65].

Similarly to CDF [5], we observe a discrepancy of the same order with NLO NRQCD calculations. Moreover, both CDF and CMS experiments observe a decrease of the  $\chi_{c2}/\chi_{c1}$  production ratio while NLO NRQCD predicts an increase of the  $\chi_{c2}/\chi_{c1}$  production ratio with  $J/\psi$   $p_T$ . Higher order corrections in the perturbative calculations of the formation of the  $c\bar{c}$  pair are not expected to reduce this discrepancy with experimental results at high  $p_T(J/\psi)$  [65]. This difference can only be explained [65] with non-perturbative contributions related to the binding of the  $c\bar{c}$  pair into charmonium.

A proper comparison between the NLO NRQCD prediction and the measurement depends on the predicted polarization of  $\chi_c$ , which is not known. For example, if the predicted polarization were to increase the measured production ratio, the agreement between theory and measurement would be better at high  $p_T(J/\psi)$  [65]. Hence, a measurement of the  $\chi_c$  polarization is crucial to interpret the existing results within the framework of NRQCD.

This measurement is among the most precise measurements of the  $\chi_c$  production cross section ratio made in hadron collisions which extends the explored range to high  $p_T$  values of the  $J/\psi$ .

## REFERENCES

- [1] The CMS Collaboration, S. Chatrchyan et al., JINST **3** (2008) S08004.
- [2] O. Bruning et. al, LHC Design Report, CERN-2004-03, (2004) CERN.
- [3] N. Brambilla et. al, CERN Yellow Report, CERN-2005-005, arXiv:hep-ph / 0412158 (2005).
- [4] LHCb Collaboration, Phys. Lett. **B714** (2012) 215.
- [5] CDF Collaboration, Phys. Rev. Lett. **98** (2007) 232001.
- [6] J. Pantaleone et. al, Phys. Rev. **D33** (1986) 777.
- [7] D. Ebert et. al, Phys. Rev. **D67** (2003) 014027.
- [8] I. Hinchliffe et. al, Ann. Rev. Nucl. Part. Sci. **50** (2000) 643.
- [9] J. Conway et. al, Eur. J. Phys. **22** (2001) 533.
- [10] M.A. Shifman et. al, Nucl. Phys. **B147** (1979) 385.
- [11] M.B. Voloshin et. al, Nucl. Phys. **B154** (1979) 365.
- [12] W.E. Caswell et. al, Phys. Lett. **B167** (1986) 437.
- [13] A. Pineda, Nucl. Phys. B Proc. Suppl. **64** (1998) 428.
- [14] M. Beneke, CERN-TH/97-55, arXiv:hep-ph / 9703429 (1997).
- [15] W.E. Caswell et. al, Phys. Rev. **D51** (1995) 1125.
- [16] M. Luke et. al, Phys. Lett. **D55** (1997) 4129.
- [17] C.H. Chang et. al, Nucl. Phys. **B172** (1980) 425.
- [18] R. Baier et. al, Phys. Lett. **B102** (1981) 364.
- [19] W.Y. Keung, Phys. Rev. **D23** (1981) 2072.
- [20] E.L. Berger, Phys. Rev. **D23** (1981) 1521.
- [21] H. Fritzch, Phys. Lett. **B67** (1977) 217.
- [22] F. Halzen, Phys. Lett. **B69** (1977) 105.
- [23] G.T. Bodwin et. al, Phys. Rev. **D65** (2002) 054504.
- [24] X. Garcia i Tormo et. al, Phys. Rev. **D69** (2004) 114006.
- [25] N. Brambilla et. al, Phys. Rev. Lett. **88** (2002) 012003.



- [26] F. Maltoni, Proceedings of the 5th Workshop on QCD, Villefranche-sur-Mer, France (2000), arXiv:hep-ph / 0007003 (2000).
- [27] J. Campbell et. al, Phys. Rev. Lett. **98** (2007) 252002.
- [28] Y.Q. Ma et. al, Phys. Rev. **D83** (2011) 111503.
- [29] E. Braaten, Annual Review of Nuclear and Particle Science, Vol. **46** (1996) 197-235.
- [30] E. Braaten et. al, Phys. Rev. Lett. **71** (1993) 1673.
- [31] E. Braaten et. al, Phys. Rev. **D50** (1994) 3176.
- [32] Ringaile Placakyte for H1 and ZEUS Collaborations, Proceedings of the PIC2011, Vancouver (2011), arXiv:hep-ph / 1111.5452 (2011)
- [33] J.C. Collins et. al, Nucl. Phys. **B194** (1982) 445.
- [34] S. Catani et. al, Phys. Lett. **B242** (1990) 97.
- [35] J.C. Collins et. al, Nucl. Phys. **B360** (1991) 3.
- [36] M.G. Ryskin et. al, Phys. Atom. Nucl. **64** (2001) 1995.
- [37] B.W. Xiao and F. Yuan, Phys. Rev. Lett. **105** (2010) 062001.
- [38] The CMS Collaboration, <https://espace.cern.ch/cms-quarkonia/trigger-bph/Menu2011/Home.aspx>, last access date 12.09.2012
- [39] G.L. Bayatyan et al, CERN-LHCC-2005-023, CMS-TDR-007 (2005).
- [40] E. Widl et al., CMS-NOTE-2006-022, <http://cdsweb.cern.ch/record/927376>.
- [41] W. Adam et al., J. Phys. **G31 N9** (2005).
- [42] The CMS Collaboration, CMS-PAS-TRK-10-003.
- [43] CDF Collaboration, Phys. Rev. **D71** (2005) 032001.
- [44] K. Nakamura et al., J. Phys. **G37** (2010) 075021.
- [45] The CMS Collaboration, Eur. Phys. J. **C71** (2011) 1575.
- [46] W. Verkerke et al., Proceedings of the Conference for Computing in High-Energy and Nuclear Physics (CHEP 03), La Jolla, California (2003), arXiv:physics / 0306116 (2003).
- [47] M.J. Oreglia, SLAC -R -236 (1980) Appendix D.
- [48] J.E Gaiser, SLAC -R -255 (1982) Appendix F.
- [49] T. Sjostrand, S. Mrenna and P. Skands, Pythia 6.4 Physics and Manual.
- [50] GEANT4 Collaboration, Nucl. Inst. and Meth. **A506** (2003) 250.
- [51] GEANT4 Collaboration, IEEE. Trans. Nucl. Sci. **53** (2006) 270.
- [52] P. Faccioli et. al, Eur. Phys. J **C69** (2010) 657.

- [53] P. Faccioli et. al, Phys. Rev. **D83** (2011) 096001.
- [54] Fermilab E835 Collaboration, Phys. Rev. **D65** (2002) 052002.
- [55] M.G. Olsson et. al, Phys. Rev. **D34** (1986) 2043.
- [56] The CMS Collaboration, <https://twiki.cern.ch/twiki/bin/view/CMSPublic/SWGuideFastSimPileUp>, last access date 25.07.2012
- [57] G. Cerati, G.Sguazzoni, CMS Note 2010/040 (2010).
- [58] E. Migliore, G.Sguazzoni, CMS Note 2010/010 (2010).
- [59] J.C Collins, D.E. Soper, Phys. Rev. **D16** (1977) 2219.
- [60] S.P. Baranov, Phys. Rev. **D83** (2011) 034035.
- [61] S.P. Baranov, Private communication, results to be published.
- [62] F.L. Ridener et. al, Phys. Rev. **D45** (1992) 3173.
- [63] P. Faccioli, Private Monte Carlo code generating  $\chi_c$  mesons in different polarization states.
- [64] The CMS Collaboration, CMS Paper BPH 2011/010 (2012), Submitted for publication to EPJC.
- [65] S.P. Baranov and P. Faccioli, Private communication.

## APPENDIX A

### Kinematic variables

#### Particle coordinates

Particle with four momentum  $p^\mu = (E, \vec{p})$  in the laboratory frame has

- rapidity:  $y = \frac{1}{2} \ln \frac{E+p_z}{E-p_z}$
- pseudorapidity:  $\eta = -\ln \left[ \tan \frac{\theta}{2} \right]$
- transverse momentum:  $p_T = \sqrt{p_x^2 + p_y^2} = p \sin \theta$

#### Track coordinates

Track coordinates are defined with respect to the point of closest approach (impact point) of the track to the beam axis.

- $d_0$ : coordinate of the impact point in the transverse plain of the detector  
 $d_0 = y_0 \cos \phi - x_0 \sin \phi$ , where  $x_0$  and  $y_0$  are the transverse coordinates of the impact point with respect to the beam spot (mean pp collision)
- $z_0$ : coordinate of the impact point in the longitudinal plain of the detector with respect to the primary vertex
- $\phi$ : azimuthal angle of the momentum vector of the track
- $\cot \theta$ : cotangent of the polar angle of the track momentum vector

- $p_T$ : transverse momentum

The resolutions of  $d_0$  and  $z_0$  at high momentum (100 GeV/c) are dominated by the hit resolution in pixel detector. At low momenta (1 GeV/c) the resolutions are affected significantly by multiple scattering. For a 1 GeV/c track at  $|\eta| < 1$  the resolution of  $d_0$  and  $z_0$  is about 100  $\mu\text{m}$ .

## APPENDIX B

### Fitting methods

In high energy physics the mass, the width and the yield of a particle can be inferred by fitting the invariant mass distribution of its daughter particles. This distribution consists of signal and background events and both distributions are fitted simultaneously. Fitting is done by using parametrized theoretical curves known as Probability Distribution Functions (PDF). For example the mass peak of a particle can be fitted with a Gaussian PDF and for the background a polynomial PDF can be used. There are several fitting techniques:

- $\chi^2$  method
- Binned maximum likelihood
- Unbinned maximum likelihood

#### $\chi^2$ method

The method of least  $\chi^2$  is the most popular one. It minimizes the sum of squared residuals, where the residual is the difference between the observed and the fitted value provided by a model. It is only applied to binned data.

#### Binned and unbinned maximum likelihood

Lets suppose the data is composed of  $N$  measurements  $x = x_1, x_2, \dots, x_N$  and the PDF of data points  $x$  is  $f(x|\theta)$ . The vector  $\theta = \theta_1, \dots, \theta_m$  has  $m$  parameters. The shape of the PDF is known but the parameter values  $\theta$  are unknown. Then the joint PDF for data points  $x$  is given by the likelihood function:

$$L(x|\theta) = \prod_{i=1}^N f(x_i|\theta) \quad (\text{B.1})$$

The likelihood is a function of the parameters  $\theta$ . The values of  $x$  are fixed and are given by the experiment. The maximum likelihood estimate of the parameters  $\theta$  or their most probable values are those for which the likelihood function has its global maximum. In general, for wrong parameter values of  $\theta$  the likelihood function will have smaller values. Instead of finding global maximum, for computational reasons, it is better to find the minimum of the log-likelihood function:

$$\log L(x|\theta) = \sum_{i=1}^N \log f(x_i|\theta) \quad (\text{B.2})$$

For unbinned maximum likelihood fit, the data is not grouped in bins, as it is the case for binned maximum likelihood fit. This avoids losing information caused by the binning. It is common to bin the data only if we want to be faster in the calculations of the likelihood function.

Now, if we consider that the number of events  $N$  is allowed to fluctuate as a Poisson random variable with mean value  $\nu$ , then the likelihood is a product of the PDF for each data  $x_i$  multiplied by the probability of observing  $N$  events

$$L(x|\nu, \theta) = \frac{\nu^N}{N!} e^{-\nu} \prod_{i=1}^N f(x_i|\theta). \quad (\text{B.3})$$

Then the log-likelihood is

$$\log L(x|\theta) = \sum_{i=1}^N \log f(x_i|\theta) + N \log \nu - \nu \quad (\text{B.4})$$

by dropping terms which do not depend on  $\theta$  and  $\nu$ .

In reality, the number of events,  $N$ , consists of signal and background events. Therefore we can write the above equation separating the number of signal  $n_s$  and background events  $n_b$  in the following way

$$\log L(x|n_s, n_b, \theta) = \sum_{i=1}^N \log(f_s(x_i|\theta) + f_b(x_i|\theta)) + N \log(n_s + n_b) - n_s - n_b \quad (\text{B.5})$$

where  $n_s + n_b$  can fluctuate around the number of observed events,  $N$ . Therefore the parameters for which the maximum likelihood function should be maximized are  $n_s$ ,  $n_b$  and  $\theta$ . This is called extended maximum likelihood formalism.

## APPENDIX C

### Fits to Pythia Monte Carlo particle gun

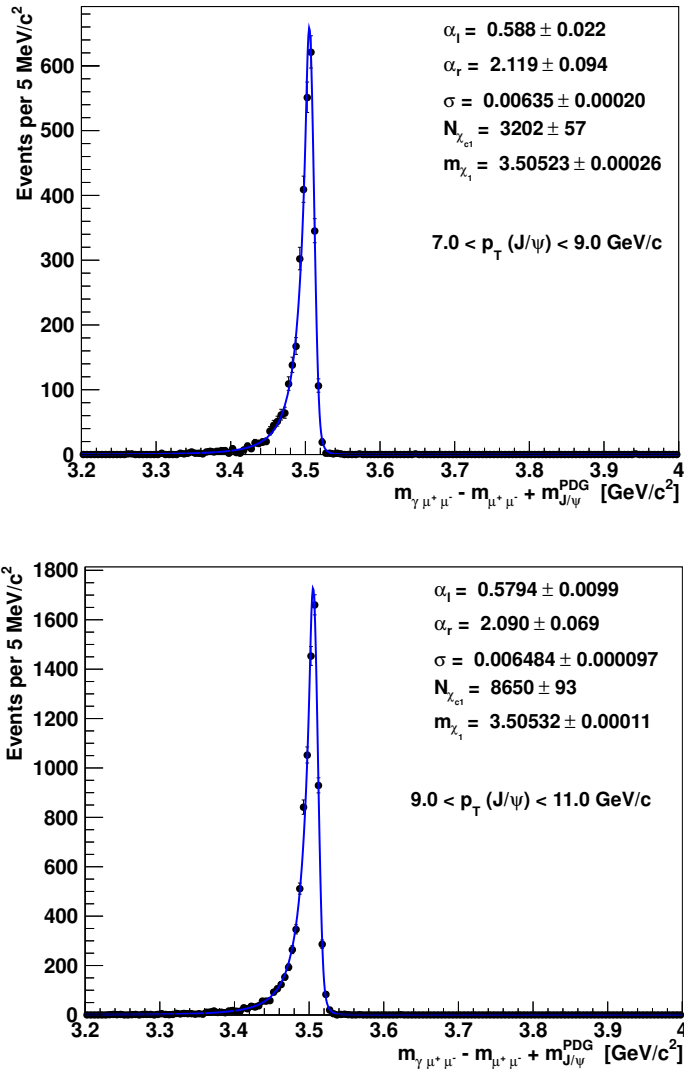


Figure C.1: Double-sided Crystal Ball fits to particle gun Monte Carlo for  $\chi_{c1}$  candidates for  $p_T(J/\psi)$  in [7.0–9.0] GeV/c (top) and [9.0–11.0] GeV/c (bottom).



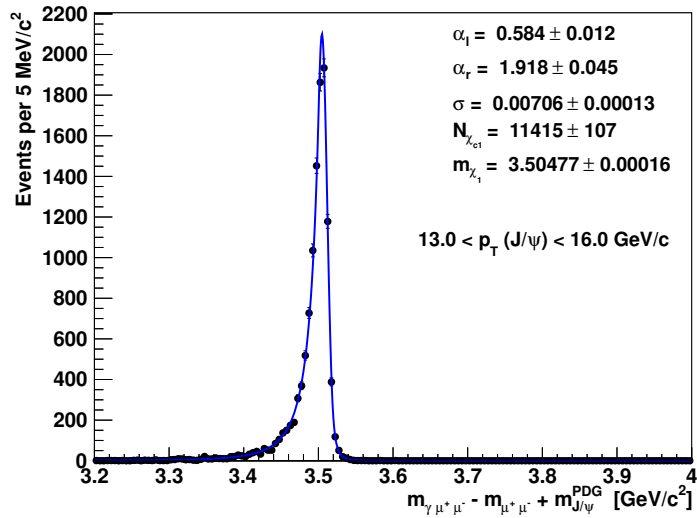
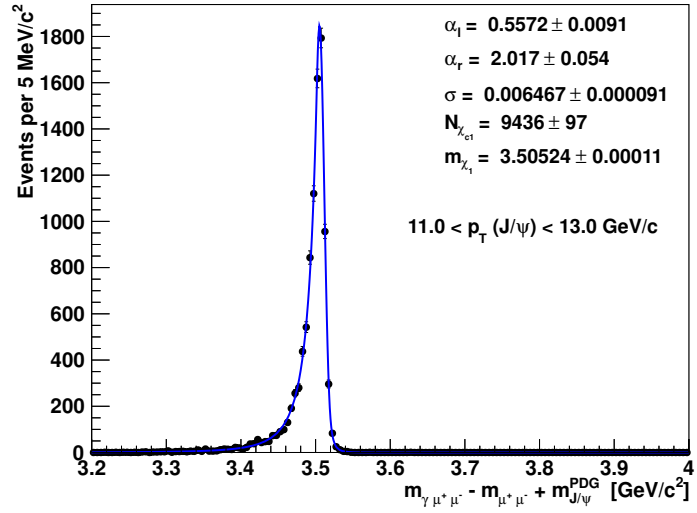


Figure C.2: Double-sided Crystal Ball fits to particle gun Monte Carlo for  $\chi_{c1}$  candidates for  $p_T(J/\psi)$  in [11.0 – 13.0] GeV/c (top) and [13.0 – 16.0] GeV/c (bottom).

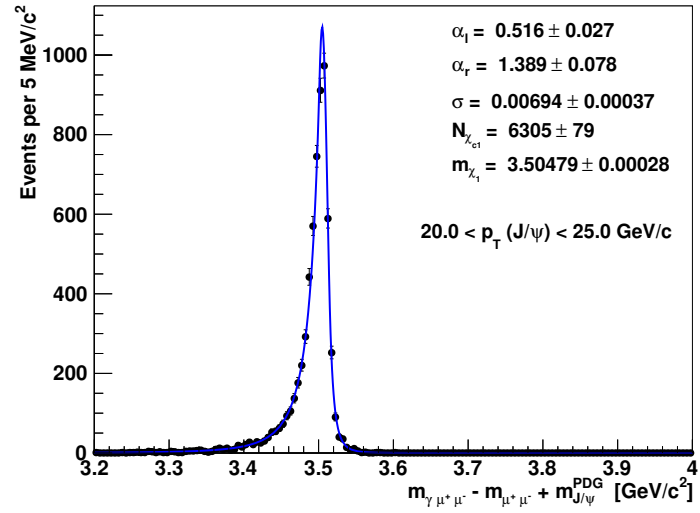
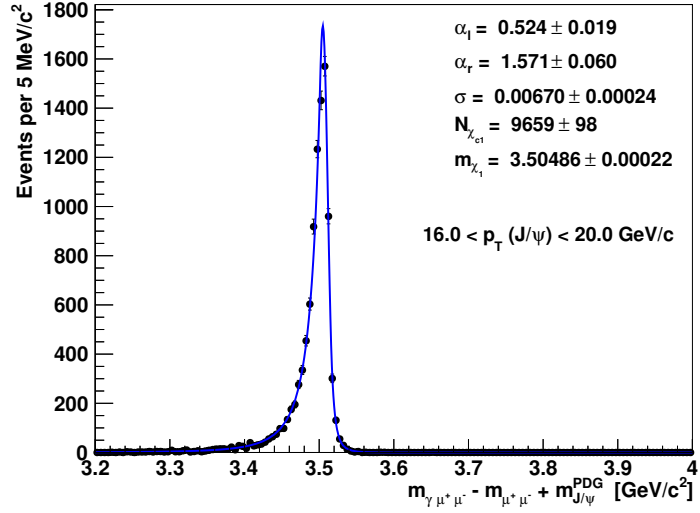


Figure C.3: Double-sided Crystal Ball fits to particle gun Monte Carlo for  $\chi_{c1}$  candidates for  $p_T(J/\psi)$  in  $[16.0 - 20.0]$  GeV/c (top) and  $[20.0 - 25.0]$  GeV/c (bottom).

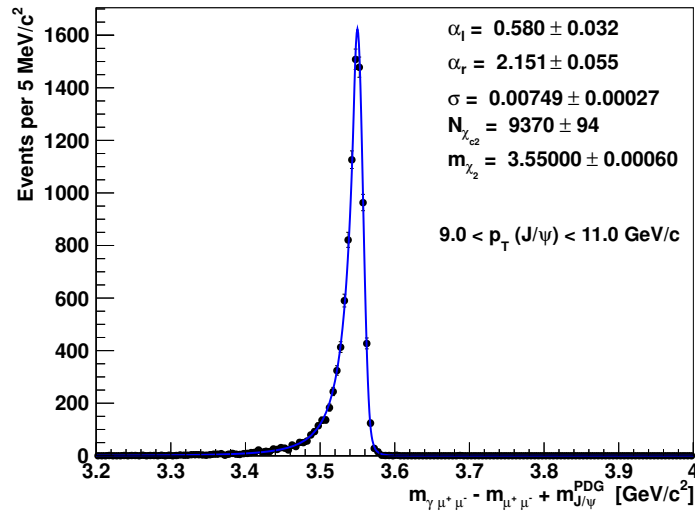
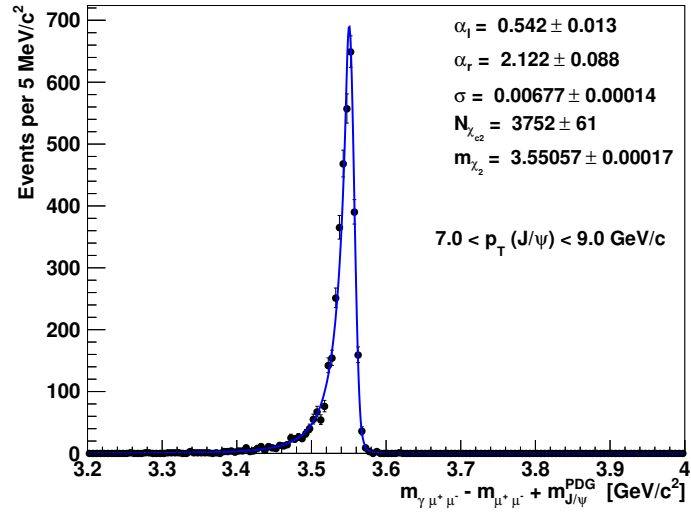


Figure C.4: Double-sided Crystal Ball fits to particle gun MC for  $\chi_{c2}$  candidates for  $p_T(J/\psi)$  in [7.0–9.0] GeV/c (top) and [9.0–11.0] GeV/c (bottom).

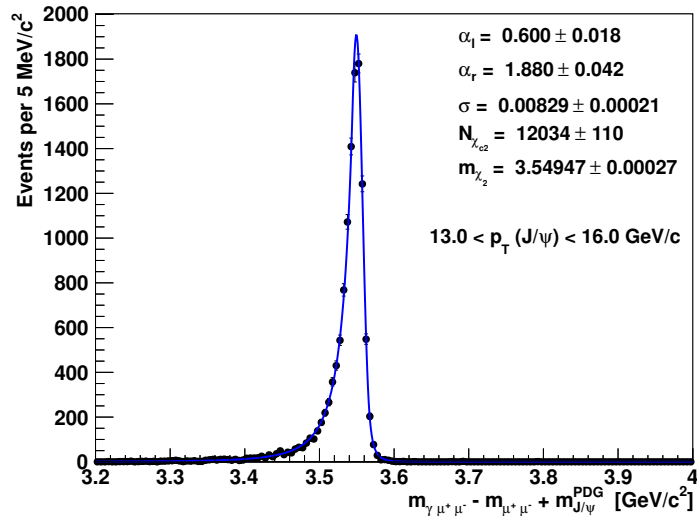
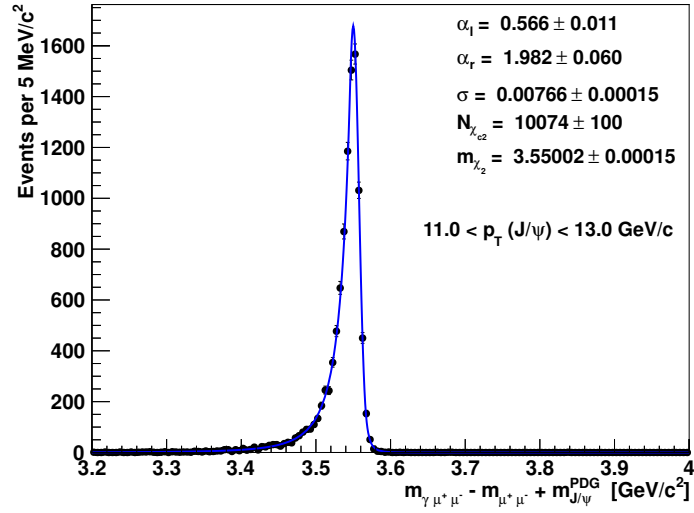


Figure C.5: Double-sided Crystal Ball fits to particle gun MC for  $\chi_{c2}$  candidates for  $p_T(J/\psi)$  in [11.0–13.0] GeV/c (top) and [13.0–16.0] GeV/c (bottom).

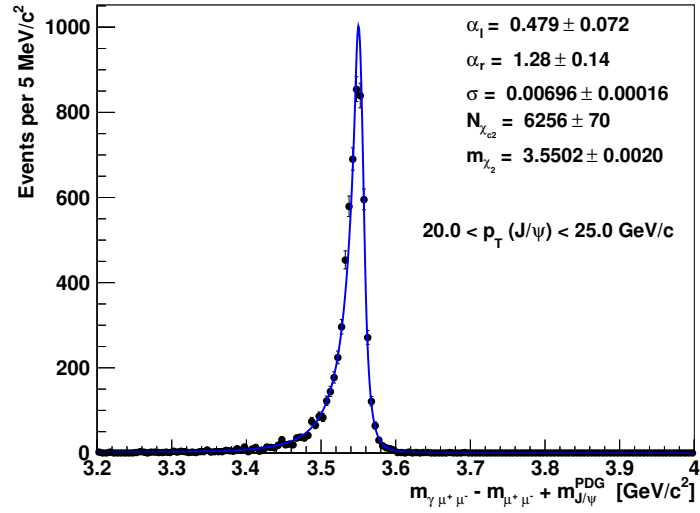
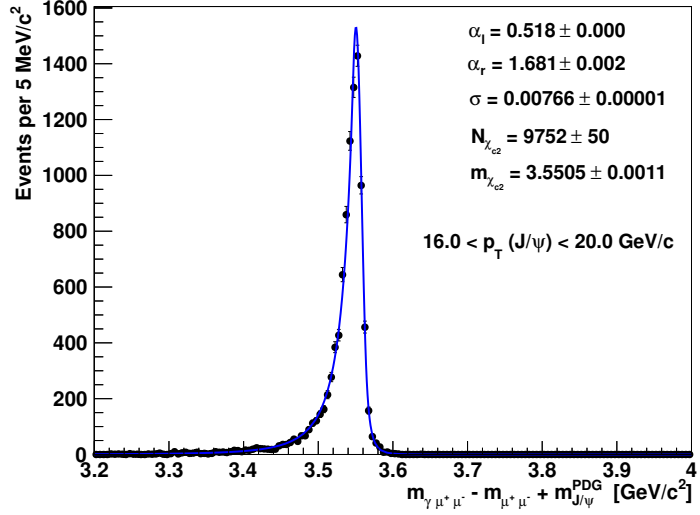


Figure C.6: Double-sided Crystal Ball fits to particle gun MC for  $\chi_{c2}$  candidates for  $p_T(J/\psi)$  in [16.0 – 20.0] GeV/c (top) and [20.0 – 25.0] GeV/c (bottom).

## APPENDIX D

### Uncertainties from the signal model

Different cases in Table D.1 are formulated by varying signal parameters  $\sigma$ ,  $\alpha_l$  and  $\alpha_r$  for  $\chi_{c1}$  and  $\chi_{c2}$  within their uncertainties,  $e$ :

- [1] – [2]: variation of  $\sigma_{\chi_{c1}}$
- [3] – [4]: variation of  $\sigma_{\chi_{c2}}$
- [5] – [6]: variation of  $\alpha_l(\chi_{c1})$
- [7] – [8]: variation of  $\alpha_r(\chi_{c1})$
- [9] – [10]: variation of  $\alpha_l(\chi_{c2})$
- [11] – [12]: variation of  $\alpha_r(\chi_{c2})$
- [13] – [14]: variation of  $\sigma_{\chi_{c1}}$  and  $\sigma_{\chi_{c2}}$
- [15] – [16]: variation of  $\alpha_l(\chi_{c1})$  and  $\alpha_r(\chi_{c1})$

Table D.1: Ratio of  $N_{\chi_{c2}}/N_{\chi_{c1}}$  for different signal parameters varied within their uncertainties.

case	7 – 9	9 – 11	11 – 13	13 – 16	16 – 20	20 – 25
default	$0.510 \pm 0.049$	$0.469 \pm 0.027$	$0.451 \pm 0.025$	$0.482 \pm 0.027$	$0.384 \pm 0.028$	$0.368 \pm 0.040$
[1] $\sigma_{\chi_{c1}} + e$	$0.503 \pm 0.048$	$0.466 \pm 0.027$	$0.448 \pm 0.025$	$0.478 \pm 0.027$	$0.378 \pm 0.028$	$0.359 \pm 0.039$
[2] $\sigma_{\chi_{c1}} - e$	$0.517 \pm 0.049$	$0.472 \pm 0.027$	$0.453 \pm 0.025$	$0.486 \pm 0.027$	$0.390 \pm 0.029$	$0.379 \pm 0.041$
[3] $\sigma_{\chi_{c2}} + e$	$0.515 \pm 0.049$	$0.477 \pm 0.028$	$0.454 \pm 0.025$	$0.488 \pm 0.027$	$0.384 \pm 0.028$	$0.372 \pm 0.041$
[4] $\sigma_{\chi_{c2}} - e$	$0.504 \pm 0.048$	$0.461 \pm 0.027$	$0.446 \pm 0.025$	$0.476 \pm 0.027$	$0.384 \pm 0.028$	$0.364 \pm 0.042$
[5] $\alpha_r(\chi_{c1}) + e$	$0.514 \pm 0.049$	$0.471 \pm 0.027$	$0.452 \pm 0.025$	$0.484 \pm 0.027$	$0.386 \pm 0.029$	$0.371 \pm 0.041$
[6] $\alpha_r(\chi_{c1}) - e$	$0.506 \pm 0.048$	$0.468 \pm 0.027$	$0.449 \pm 0.025$	$0.480 \pm 0.027$	$0.382 \pm 0.028$	$0.366 \pm 0.040$
[7] $\alpha_r(\chi_{c1}) + e$	$0.512 \pm 0.049$	$0.471 \pm 0.027$	$0.452 \pm 0.025$	$0.483 \pm 0.027$	$0.387 \pm 0.028$	$0.375 \pm 0.041$
[8] $\alpha_r(\chi_{c1}) - e$	$0.508 \pm 0.049$	$0.468 \pm 0.027$	$0.449 \pm 0.025$	$0.480 \pm 0.027$	$0.380 \pm 0.028$	$0.361 \pm 0.040$
[9] $\alpha_r(\chi_{c2}) + e$	$0.504 \pm 0.048$	$0.457 \pm 0.026$	$0.446 \pm 0.025$	$0.475 \pm 0.027$	$0.384 \pm 0.028$	$0.342 \pm 0.037$
[10] $\alpha_r(\chi_{c2}) - e$	$0.516 \pm 0.049$	$0.483 \pm 0.028$	$0.455 \pm 0.025$	$0.489 \pm 0.028$	$0.384 \pm 0.028$	$0.403 \pm 0.044$
[11] $\alpha_r(\chi_{c2}) + e$	$0.509 \pm 0.049$	$0.469 \pm 0.027$	$0.450 \pm 0.025$	$0.481 \pm 0.027$	$0.384 \pm 0.028$	$0.366 \pm 0.040$
[12] $\alpha_r(\chi_{c2}) - e$	$0.511 \pm 0.049$	$0.470 \pm 0.027$	$0.451 \pm 0.025$	$0.482 \pm 0.027$	$0.384 \pm 0.028$	$0.371 \pm 0.040$
[13] $\sigma_{\chi_{c1}} + e$ and $\sigma_{\chi_{c2}} + e$	$0.509 \pm 0.049$	$0.474 \pm 0.027$	$0.452 \pm 0.025$	$0.484 \pm 0.027$	$0.378 \pm 0.028$	$0.363 \pm 0.040$
[14] $\sigma_{\chi_{c1}} - e$ and $\sigma_{\chi_{c2}} - e$	$0.511 \pm 0.049$	$0.464 \pm 0.027$	$0.449 \pm 0.025$	$0.480 \pm 0.027$	$0.390 \pm 0.029$	$0.374 \pm 0.041$
[15] $\alpha_r(\chi_{c1}) + e$ and $\alpha_r(\chi_{c1}) + e$	$0.516 \pm 0.049$	$0.472 \pm 0.027$	$0.453 \pm 0.025$	$0.485 \pm 0.027$	$0.389 \pm 0.029$	$0.377 \pm 0.041$
[16] $\alpha_r(\chi_{c1}) - e$ and $\alpha_r(\chi_{c1}) - e$	$0.504 \pm 0.048$	$0.466 \pm 0.027$	$0.448 \pm 0.011$	$0.478 \pm 0.027$	$0.378 \pm 0.028$	$0.359 \pm 0.039$
diff	$-0.006/+0.007$	$-0.014/+0.012$	$-0.004/+0.005$	$-0.007/+0.007$	$-0.006/+0.006$	$-0.011/+0.026$

## APPENDIX E

### $p_T(J/\psi)$ spectrum measured with the CMS experiment

We use the data available in [45] for the  $J/\psi$  momentum spectrum in the range  $|y(J/\psi)| < 0.9$  and parametrize the data using the expression

$$\frac{dN}{dp_T} \propto p_T \left[ 1 + \frac{1}{(\beta-2)} \frac{p_T^2}{\langle p_T^2 \rangle} \right]^{-\beta}. \quad (\text{E.1})$$

The fitted  $p_T(J/\psi)$  spectrum used to model  $p_T(\chi_c)$  spectrum is shown in Figure E.1.

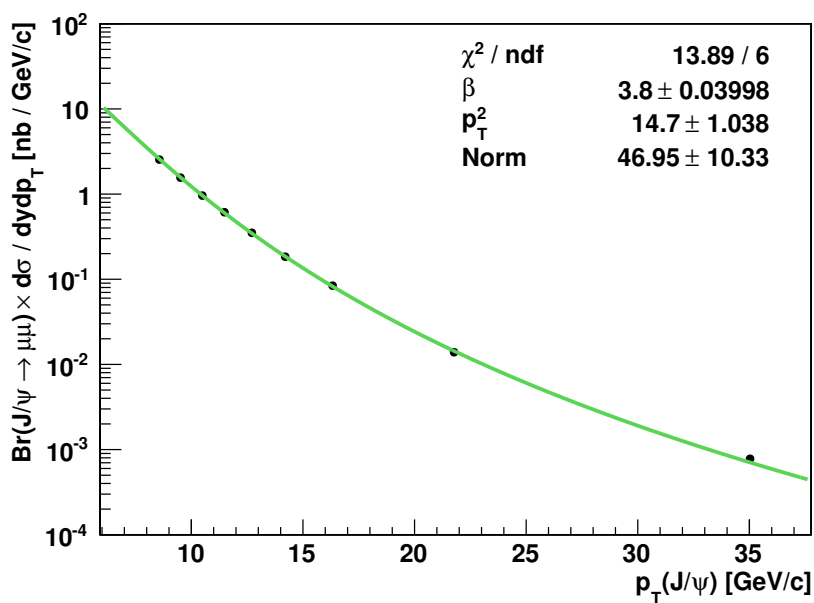


Figure E.1: The  $p_T$  spectrum measured in [45] is shown with data points. The green line is the fit to data using Equation 4.13. The fitted spectrum is used as input distribution for the Pythia Monte Carlo particle gun.



## APPENDIX F

### Expressions for the $\chi_{c1}$ and $\chi_{c2}$ decay angular distributions

The  $\chi_c$  polarization depends on the properties of the  $c\bar{c}$  bound state and the nature of the radiative decay  $\chi_c \rightarrow J/\psi + \gamma$ . The radiative transitions between  $\chi_c$  and  $J/\psi$  can be analyzed in terms of electric and magnetic  $2^l$  pole radiation like dipole, quadropole etc. The  $2^l$  pole transitions are usually indicated as  $El$  and  $Ml$ , where  $l$  is the total angular momentum of the emitted photon,  $E$  stands for electric and  $M$  for magnetic radiation. For  $\chi_{c1}$  and  $\chi_{c2}$  states, only  $E1$  and  $M2$  transitions are allowed. Additionally, for the  $\chi_{c2}$  state also  $E3$  transition is allowed.

The angular distributions of the decay products in  $\chi_c \rightarrow J/\psi + \gamma$  and  $J/\psi \rightarrow \mu^+ + \mu^-$  are parametrized as a function of the angular momentum composition of the decaying  $\chi_c$  meson and of the multiple structure of the photon radiation [53, 55, 62]. These angular distributions, denoted with  $W(\theta, \theta', \phi')$ , are expressed in terms of observables,  $k_i$ , and trigonometric functions,  $T_i$ ,

$$W(\theta, \theta', \phi') = \sum k_i(A_i)T_i(\theta, \theta', \phi'). \quad (\text{F.1})$$

The coefficients  $k_i$  are written in terms helicity amplitudes  $A_i$  which parametrize the dynamics of the decay process. The helicity amplitudes  $A_i$  are linear combinations of the multipole transition amplitudes  $a_i$  which are related to the total angular momentum carried by the photon. The values of  $a_1$ ,  $a_2$  and  $a_3$  correspond to  $E1$ ,  $M2$  and  $E3$  transitions. The amplitudes  $A_i$  and  $a_i$  are normalized to one. The coefficients  $T_i$  are functions of the observed angles  $\theta$ ,  $\theta'$  and  $\phi'$ . Below are the full angular distribution functions,  $W(\theta, \theta', \phi')$ , for the  $\chi_{c1}$  and  $\chi_{c2}$  states [63] that are used in the reweighting procedure.

$\chi_{c1}$  angular distributions

$$W(\theta, \theta', \phi') = k_1 + k_2 \cos^2 \theta + (k_3 + k_4 \cos^2 \theta) \cos^2 \theta' + k_5 \sin^2 \theta \sin^2 \theta' \cos \phi'. \quad (\text{F.2})$$

Coefficients  $k_i$  are defined as

$$\begin{aligned} k_1 &= A_1^2 + 1/2R(A_0^2 - A_1^2) & k_2 &= (1 - 3/2R)(A_0^2 - A_1^2) \\ k_3 &= -A_1^2 + 1/2R & k_4 &= 1 - 3/2R \\ k_5 &= 1/4A_1^2(3R - 2) \end{aligned}$$

where  $A_0 = \sqrt{1/2}(a_1 + a_2)$  and  $A_1 = \sqrt{1/2}(a_1 - a_2)$ . The values of  $a_1$  and  $a_2$  correspond to  $E1$  and  $M2$  transitions. The  $M2$  contributions can be neglected with sufficiently high accuracy, therefore  $a_2 = 0$  and  $a_1 = \sqrt{1 - a_2^2}$ . Coefficient  $R$  measures fractional contribution of helicity  $\pm 1$  particles to the production processes of  $\chi_{c1}$ . The  $\chi_{c1}$  can have helicities 0 and  $\pm 1$  hence for helicity 0:  $R = 0$ , for helicity  $\pm 1$ :  $R = 1$ . For the unpolarized  $\chi_c$  meson,  $R = 2/3$ .

$\chi_{c2}$  angular distributions

$$\begin{aligned} W(\theta, \theta', \phi') &= k_1 + k_2 \cos^2 \theta + k_3 \cos^4 \theta + (k_4 + k_5 \cos^2 \theta + k_6 \cos^4 \theta) \cos^2 \theta' \\ &\quad + (k_7 + k_8 \cos^2 \theta + k_9 \cos^4 \theta) \sin^2 \theta' \cos 2\phi' \\ &\quad + (k_{10} + k_{11} \cos^2 \theta) \sin 2\theta \sin 2\theta' \cos \phi' \end{aligned} \quad (\text{F.3})$$

Coefficients  $k_i$  are defined as

$$\begin{aligned} k_1 &= R_0 k_1^0 + R_1 k_1^1 + R_2 k_1^2 & k_2 &= R_0 k_2^0 + R_1 k_2^1 + R_2 k_2^2 \\ k_3 &= R_0 k_3^0 + R_1 k_3^1 + R_2 k_3^2 & k_4 &= R_0 k_4^0 + R_1 k_4^1 + R_2 k_4^2 \\ k_5 &= R_0 k_5^0 + R_1 k_5^1 + R_2 k_5^2 & k_6 &= R_0 k_6^0 + R_1 k_6^1 + R_2 k_6^2 \\ k_7 &= R_0 k_7^0 + R_1 k_7^1 + R_2 k_7^2 & k_8 &= R_0 k_8^0 + R_1 k_8^1 + R_2 k_8^2 \\ k_9 &= R_0 k_9^0 + R_1 k_9^1 + R_2 k_9^2 & k_{10} &= R_0 k_{10}^0 + R_1 k_{10}^1 + R_2 k_{10}^2 \\ k_{11} &= R_0 k_{11}^0 + R_1 k_{11}^1 + R_2 k_{11}^2 \end{aligned}$$

where  $R_1 = R$  and  $R_0 = 1 - R_1 - R_2$ . Coefficients  $R$  and  $R_2$  measure fractional contribution of helicity  $\pm 1$  and helicity  $\pm 2$  particles to the production processes of  $\chi_{c2}$ . The  $\chi_{c2}$  can have helicities 0,  $\pm 1$  and  $\pm 2$  hence for helicity 0:  $R = 0$  and  $R_2 = 0$ , for helicity  $\pm 1$ :  $R = 1$  and  $R_2 = 0$  and for helicity  $\pm 2$ :  $R = 0$  and  $R_2 = 1$ . For the unpolarized  $\chi_{c2}$  meson,  $R = 2/5$  and  $R_2 = 2/5$ . Coefficients  $k_i^0$ ,  $k_i^1$  and  $k_i^2$  are defined as

$$\begin{aligned}
k_1^0 &= 1/4A_0^2 + 3/8A_2^2 & k_1^1 &= 1/2A_1^2 + 1/4A_2^2 \\
k_1^2 &= 3/8A_0^2 + 1/2A_1^2 + 1/16A_2^2 & k_2^0 &= -3/2A_0^2 + 3A_1^2 - 3/4A_2^2 \\
k_2^1 &= 3/2A_0^2 + 3/2A_1^2 & k_2^2 &= -3/4A_0^2 + 3/8A_2^2 \\
k_3^0 &= 9/4A_0^2 - 3A_1^2 + 3/8A_2^2 & k_3^1 &= -3/2A_0^2 + 2A_1^2 - 1/4A_2^2 \\
k_3^2 &= 3/8A_0^2 - 1/2A_1^2 + 1/16A_2^2 & k_4^0 &= 1/4A_0^2 + 3/8A_2^2 \\
k_4^1 &= -1/2A_1^2 + 1/4A_2^2 & k_4^2 &= 3/8A_0^2 - 1/2A_1^2 + 1/16A_2^2 \\
k_5^0 &= -3/2A_0^2 - 3A_1^2 - 3/4A_2^2 & k_5^1 &= 3/2A_0^2 + 3/2A_1^2 \\
k_5^2 &= -3/4A_0^2 + 3/8A_2^2 & k_6^0 &= 9/4A_0^2 + 3A_1^2 + 3/8A_2^2 \\
k_6^1 &= -3/2A_0^2 - 2A_1^2 - 1/4A_2^2 & k_6^2 &= 3/8A_0^2 + 1/2A_1^2 + 1/16A_2^2 \\
k_7^0 &= -\sqrt{6}/4A_0A_2 & k_7^1 &= 0 \\
k_7^2 &= \sqrt{6}/8A_0A_2 & k_8^0 &= \sqrt{6}A_0A_2 \\
k_8^1 &= -\sqrt{6}/2A_0A_2 & k_8^2 &= 0 \\
k_9^0 &= -3\sqrt{6}/4A_0A_2 & k_9^1 &= \sqrt{6}/2A_0A_2 \\
k_9^2 &= -\sqrt{6}/8A_0A_2 & k_{10}^0 &= \sqrt{3}/4A_0A_1 + 3\sqrt{2}/8A_1A_2 \\
k_{10}^1 &= -\sqrt{3}/4A_0A_1 & k_{10}^2 &= \sqrt{3}/8A_0A_1 - 3\sqrt{2}/16A_1A_2 \\
k_{11}^0 &= -3\sqrt{3}/4A_0A_1 - 3\sqrt{2}/8A_1A_2 & k_{11}^1 &= \sqrt{3}/2A_0A_1 + \sqrt{2}/4A_1A_2 \\
k_{11}^2 &= -\sqrt{3}/8A_0A_1 - \sqrt{2}/16A_1A_2
\end{aligned}$$

where  $A_0 = \sqrt{1/10}a_1 + \sqrt{1/2}a_2 + \sqrt{2/5}a_3$ ,  $A_1 = \sqrt{3/10}a_1 + \sqrt{1/6}a_2 - \sqrt{8/15}a_3$  and  $A_2 = \sqrt{3/5}a_1 - \sqrt{1/3}a_2 + \sqrt{1/15}a_3$ . The values of  $a_1$ ,  $a_2$  and  $a_3$  correspond to  $E1$ ,  $M2$  and  $E3$  transitions. In this case,  $M2$  and  $E3$  contributions can be neglected, therefore  $a_2 = 0$  and  $a_3 = 0$  and  $a_1 = \sqrt{1 - a_2^2 - a_3^2}$ .

## APPENDIX G

### Polarization of $\chi_c$ in Collins-Soper frame

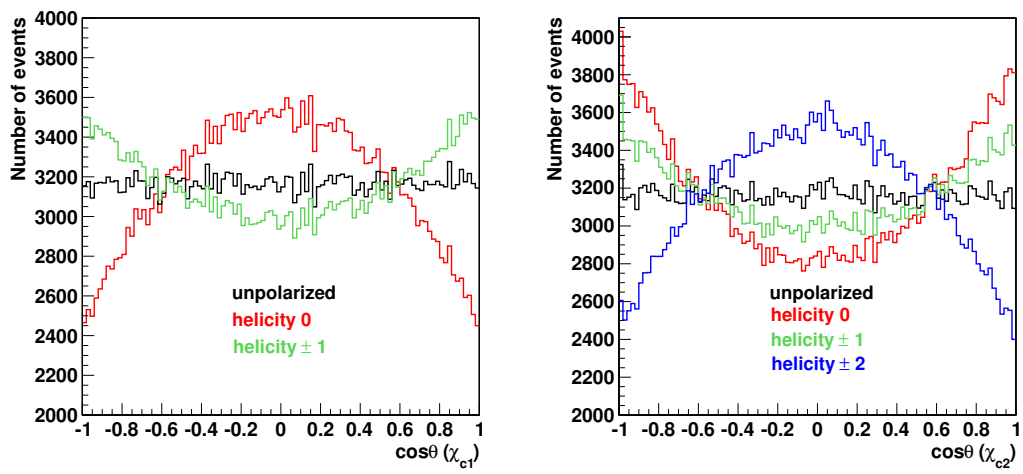


Figure G.1: Angle between the direction of  $J/\psi$  and  $\chi_c$  as seen in  $\chi_c$  rest frame for unpolarized, helicities 0,  $\pm 1$  and  $\pm 2$   $\chi_c$  states in the Collins-Soper frame. Left:  $\chi_{c1}$ , right:  $\chi_{c2}$ .

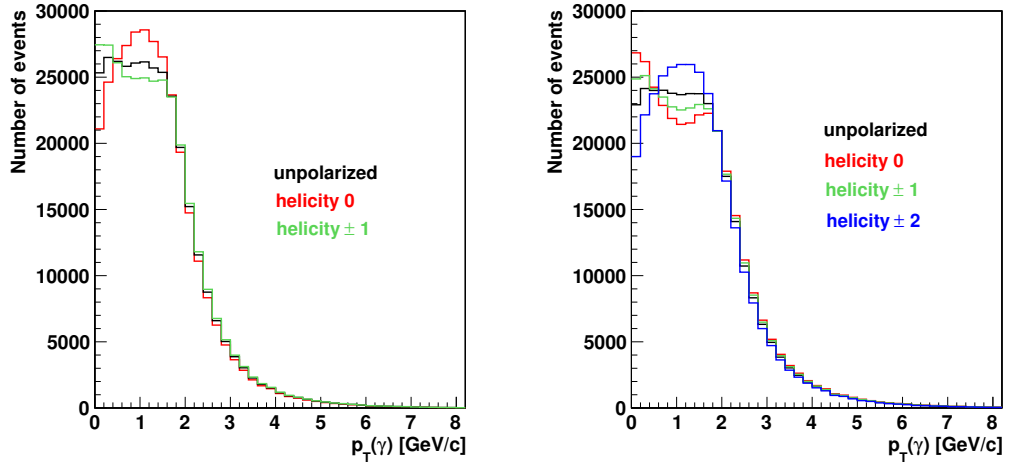


Figure G.2:  $p_T$  distributions of the photon from  $\chi_{c1}$  (left) and  $\chi_{c2}$  (right) for unpolarized, helicities 0,  $\pm 1$  and  $\pm 2$   $\chi_c$  states in the Collins-Soper frame.

Table G.1: The values of  $\epsilon_1/\epsilon_2$  for different polarization scenarios in the Collins-Soper frame relative to the unpolarized case.

$\mathcal{P}(h_{\chi_{c1}}, h_{\chi_{c2}})$	$p_T(J/\psi)[GeV/c]$					
	7–9	9–11	11–13	13–16	16–20	20–25
$\mathcal{P}(Unpolarized, 0)$	1.040	1.063	1.076	1.075	1.084	1.077
$\mathcal{P}(Unpolarized, \pm 1)$	1.016	1.035	1.048	1.033	1.056	1.037
$\mathcal{P}(Unpolarized, \pm 2)$	0.968	0.948	0.930	0.933	0.921	0.925
$\mathcal{P}(0, Unpolarized)$	1.039	1.053	1.059	1.067	1.069	1.062
$\mathcal{P}(\pm 1, Unpolarized)$	0.980	0.972	0.969	0.965	0.964	0.968
$\mathcal{P}(0, 0)$	1.081	1.119	1.139	1.147	1.157	1.144
$\mathcal{P}(0, \pm 1)$	1.056	1.092	1.108	1.101	1.127	1.102
$\mathcal{P}(0, \pm 2)$	1.006	0.998	0.985	0.995	0.984	0.982
$\mathcal{P}(\pm 1, 0)$	1.019	1.033	1.042	1.037	1.045	1.042
$\mathcal{P}(\pm 1, \pm 1)$	0.995	1.005	1.016	0.997	1.019	1.003
$\mathcal{P}(\pm 1, \pm 2)$	0.949	0.921	0.902	0.900	0.888	0.895

# Curriculum vitae - Iлина Vasileva Akin

## PERSONAL INFORMATION

Date and Place of Birth: 16 October 1977, Varna

Nationality: Bulgarian

e-mail: ilina.vasileva.akin@cern.ch

## EDUCATION

### Ph.D in Physics

2009 – 2012

Middle East Technical University, Ankara, Turkey

Thesis topic: *”Measurement of the cross-section ratio  $\sigma(\chi_{c2})/\sigma(\chi_{c1})$  for prompt  $\chi_c$  production with CMS experiment”*

Area of study: High Energy Physics

### M.S. in Physics

2006 – 2009

Middle East Technical University, Ankara, Turkey

Thesis topic: *”Search for scalar and tensor unparticles in the diphoton final state in CMS experiment”*

Master’s degree includes extended minor program in undergraduate Physics

Area of study: High Energy Physics

### Structural engineer

2001 – 2008

Structural design of various structures.

### B.S. and M.S. in Civil Engineering

1996 – 2001

University of Architecture, Civil Engineering and Geodesy, Sofia, Bulgaria

Area of study: Structural design

## **WORK EXPERIENCE**

### **Graduate Student**

**February 2011 – September 2012**

**January 2009 – September 2009**

*Exotica and B-Physics groups at CERN, Geneva, Switzerland*

I have spent about three years at CERN, the world's largest particle physics laboratory, doing research in fundamental physics with the CMS experiment. I worked in a small group focused on specific research projects within the CMS Exotica and B-Physics groups at CERN for my Master's and Ph.D. degrees.

Responsibilities:

- Developed analysis based on Monte Carlo simulation to search for exotic type of matter called "unparticles".
- Developed analysis to measure the cross-section ratio of two excited charmonium states to test one of the fundamental theories in the Standard Model physics, the theory of strong interactions among quarks and gluons, Quantum Chromodynamics. I used collision data detected with CMS experiment from 2011 for this measurement.
- Service work at CMS detector includes Data Acquisition System (DAQ) and Computing shifts.

### **Structural Steel Design Engineer**

**December 2005 – December 2008**

*Yapimer and BMAK, Ankara, Turkey*

Yapimer and BMAK are two structural and mechanical engineering firms with extensive experience in the structural design of oil refineries, cement factories, iron and steel factories, grinding plants, office and residential buildings and airport buildings in Turkey, Iraq, Russia, Nigeria etc.

Responsibilities:

- Performed structural analysis and design of industrial steel buildings subject to heavy dynamic equipment and machine loads. Designed beams, columns, braces and connections by using finite element analysis software and hand calculations.
- Created structural 3D models and performed structural steel detailing using software

programs AutoCad and XSteel. Prepared CAD drawings.

- Prepared calculation reports and technical specifications in liaison with clients and project team.
- Supervised other engineers and CAD technicians.
- Worked closely with representatives from the two biggest steel manufacturing companies in Turkey "Temsan" and "Prokon" to ensure overall project coordination and completion.
- Translated technical documentation from Russian to English language.

**Structural Design Engineer**

**November 2004 – November 2005**

*BirYapi, Ankara, Turkey*

BirYapi is a structural engineering firm with experience in the design of reinforced concrete and steel structures, wastewater treatment, water supply and water distribution projects. The firm has completed projects in Turkey, Russia, Ukraine, Azerbaijan, Afghanistan and Iraq.

Responsibilities:

- Performed structural analysis and design of residential reinforced concrete buildings in Turkey by using finite element analysis software. Designed beams, columns and foundations.
- Designed retaining walls.
- Prepared layouts, detail drawings and calculation reports.
- Translated technical documentation from Russian to English language.

**Civil Engineer**

**May 2004 – October 2004**

*Ozka Prefabrik, Ankara, Turkey*

Ozka Prefabrik is a civil engineering firm specialized in design and manufacture of accommodation containers, modular prefabricated buildings and steel structures. The firm has completed projects in Russia, Afghanistan, Iraq, Kazakhstan, Libya, Romania etc.

Responsibilities:

- Designed modular prefabricated buildings in Afghanistan and Iraq which can serve as dormitories, dining halls, offices and social buildings.



- Prepared layouts, detail drawings and specifications for the prefabricated elements.
- Supervised and monitored the production process of the prefabricated elements in the factory.

**Cartographer and group supervisor**

**September 2001 – March 2004**

*AGS Italia, Sofia, Bulgaria and Pesaro, Italy*

AGS Italia is an engineering firm operating in the field of information technology. It provides services such as cartography and cadastre of the territory of Italy and geographic information systems development.

Responsibilities:

- Led a group of thirty people and was responsible for the organization, development, coordination and completion of contract drawings.
- Photogrammetric and thematic mapping of geological and morphological areas, socio-economic and urban fields of Italy using CAD techniques.
- Produced technological maps of average and low voltage electrical networks covering the territory of Italy using CAD techniques.
- Traveled regularly to the main office of the firm based in Pesaro for trainings and new projects development.

**TALKS AT PHYSICS CONFERENCES**

I.V.Akin, " $\chi_c$  production in pp collisions at 7 TeV with CMS experiment",

International Conference in Quantum Chromodynamics, July 2012, Montpellier

**TRAINING**

*CMS B-Physics and Quarkonia workshop*, April 2012, CERN, Geneva

*Quarkonium Production Probing QCD at LHC*, May 2011, Vienna

*ISOTDAQ2010 International school of Trigger and Data acquisition*, February 2010, Ankara

*International Summer School and Conference of High Energy Physics: Standard Model and Beyond*, September 2009, Mugla

CERN Summer School, June – August 2008, Geneva

## PUBLICATIONS

- I.V.Akin, S.Argiro, D.Giordano et. al., "Measurement of the relative prompt production rate of  $\chi_{c1}$  and  $\chi_{c2}$  in pp collisions at center-of-mass energy of 7 TeV", BPH-11-010 (2012) and AN-2011-332 (2012)
- I.V.Akin, S.Ask et.al., "Real emission and virtual exchange of gravitons and unparticles in PYTHIA8", CPC 181:9 p.1593 (2010)
- I.V.Akin, G.Landsberg, A.de Roeck , "Search for scalar and tensor unparticles in diphoton final state", EXO-09-011 (2009)

## SCHOLARSHIPS AND GRANTS

Turkish Atomic Energy Authority (TAEK) Grants	<b>April 2008 – November 2012</b>
Italian Institute for Nuclear Physics (INFN) Grant	<b>February 2012 – March 2012</b>
CERN Grant for Non-Member States	<b>December 2011</b>
TUBITAK Grant	<b>December 2010 – February 2011</b>
UACEG Academic Scholarship for high grade performance	<b>1996 – 1998</b>

## AWARDS

- METU Graduate Courses 2009/2010 Performance Award, *The most successful in the Ph.D. Program of the Department of Physics*
- METU Graduate Courses 2007/2008 Performance Award, *The most successful in the M.Sc. Program of the Department of Physics*

## CODES AND STANDARDS IN ENGINEERING WORK

Turkish Standards, AISC-LRFD, AISC-ASD, SNIP

## COMPUTER SKILLS

### *For engineering*

- Structural Analysis and Design: SAP2000
- CAD: Tekla XSteel, AutoCad

### *For physics*

- Programming languages: C++ and python
- Calculation tools: Mathematica
- Data analysis: ROOT (C++) and PyROOT(python)
- Word and image processing tools: Lathex and Microsoft Office
- CMS software: CMSSW

## LANGUAGES

Bulgarian native, English fluent, Italian, Russian and Turkish good

## MISCELLANEA

- Advanced education in mathematics in a class of ten people at High School of Mathematics, Varna, Bulgaria in the period 1991-1996

## CHOSEN CIVIL ENGINEERING PROJECTS

### **Lagos Sparkwest Flour factory, Nigeria**

Built a 3D structural model, structural steel detailing and prepared manufacturing drawings.

### **Airport building Sabiha Gokcen, Istanbul, Turkey**

Structural design of passage ways, structural steel detailing and prepared manufacturing drawings for the whole building.

**Temsan OSB Factory, Ankara, Turkey**

Structural design of the factory, built 3D structural model.

**Mother Teresa International Airport, Tirana, Albania**

Steel connection design of the main building.

**Cimko Cement factory, Kahramanmaras, Turkey**

Structural design, 3D structural models and steel detailing of Preheater Tower, Additive Storage, Limestone, Coal Storage buildings, various conveyors and transfer stations.

**Bazifa Cement factory, North Iraq**

Structural design, 3D structural model and detailing of Circular Mixing Bed, Clinker Silo Structure, Mill and Crusher Structures and various conveyors.

**Iskenderun Iron Factory, Iskenderun, Turkey**

Structural design, 3D structural model and steel detailing of conveyors and transfer stations.

**Theatre building, Balkanabat, Turkmenistan**

Structural design of steel roof structure.

**Beykoz villas, Istanbul, Turkey**

Structural design of a complex of luxury villas.

**Modular Prefabricated Buildings for Afghanistan and Iraq**

Plan and design of the prefabricated buildings.